

## RESEARCH ARTICLE

# DCEM-PINNs: A deep complementary energy method for solid mechanics

Yizheng Wang<sup>1,2</sup> | Jia Sun<sup>1</sup> | Timon Rabczuk<sup>2</sup> | Yinghua Liu<sup>1</sup>

<sup>1</sup>Department of Engineering Mechanics, Tsinghua University, Beijing, China

<sup>2</sup>Institute of Structural Mechanics, Bauhaus-Universität Weimar, Marienstr. 15, Weimar, Germany

**Correspondence**

Yinghua Liu, Department of Engineering Mechanics, Tsinghua University, Beijing 100084, China.  
Email: [yhliu@mail.tsinghua.edu.cn](mailto:yhliu@mail.tsinghua.edu.cn)

**Funding Information**

This research was supported by the Key Project of the National Natural Science Foundation of China (12332005)

**Abstract**

In recent years, the rapid advancement of deep learning has significantly impacted various fields, particularly in solving partial differential equations (PDEs) in the realm of solid mechanics, benefiting greatly from the remarkable approximation capabilities of neural networks. In solving PDEs, Physics-Informed Neural Networks (PINNs) and the Deep Energy Method (DEM) have garnered substantial attention. The principle of minimum potential energy and complementary energy are two important variational principles in solid mechanics. However, the well-known Deep Energy Method (DEM) is based on the principle of minimum potential energy, but there lacks the important form of minimum complementary energy. To bridge this gap, we propose the deep complementary energy method (DCEM) based on the principle of minimum complementary energy. The output function of DCEM is the stress function, which inherently satisfies the equilibrium equation. We present numerical results of classical linear elasticity using the Prandtl and Airy stress functions, and compare DCEM with existing PINNs and DEM algorithms when modeling representative mechanical problems. The results demonstrate that DCEM outperforms DEM in terms of stress accuracy and efficiency and has an advantage in dealing with complex displacement boundary conditions, which is supported by theoretical analyses and numerical simulations. We extend DCEM to DCEM-Plus (DCEM-P), adding terms that satisfy partial differential equations. Furthermore, we propose a deep complementary energy operator method (DCEM-O) by combining operator learning with physical equations. Initially, we train DCEM-O using high-fidelity numerical results and then incorporate complementary energy. DCEM-P and DCEM-O further enhance the accuracy and efficiency of DCEM. In summary, our proposed DCEM marks the first time that complementary energy is extended to the energy-based physics-informed neural network and provides an essential supplementary energy form to the DEM in solid mechanics, offering promising research prospects in computational mechanics.

**KEYWORDS**

complementary energy, Physics-informed neural network, operator learning, DeepONet, deep learning, deep energy method

## 1 | INTRODUCTION

The laws of nature can be described and approximated through various means, including partial differential equations (PDEs), which reflect the relationship of physical quantities with space and time. PDEs stand as a foundational tool for describing the laws of nature, playing a crucial role in fields like numerical weather prediction and computational solid mechanics<sup>1</sup>. Take the discoveries of Kepler and Newton as a specific example for illustrating the importance of PDEs, it can be observed that Newton's discovery of PDEs explained the underlying mechanisms responsible for elliptic orbits based on Kepler's data driven models. As a result, PDEs model is an abstract and symbolic representation of big data. PDEs have exhibited remarkable durability in engineering design, enabling successful landing of spacecraft on the moon<sup>2</sup>. Obtaining an analytical solution to PDEs is important in the process of engineering application. However, obtaining its analytical solution in real-world applications is often unlikely, necessitating the use of numerical methods to approximate solutions. There are

several traditional numerical methods to obtain the approximate solutions to PDEs, including the well-established finite element method (FEM)<sup>3,4,5,6</sup>, the finite difference method<sup>7</sup>, the finite volume method<sup>8</sup>, and mesh-free method<sup>9,10,11,12,13,14</sup>. These methods have been developed and used for a long time, and are considered reliable numerical methods, especially FEM in solid mechanics simulation. Different trial and test functions produce various finite element numerical methods. The essence of FEM is to find the optimal solution in the approximate function space. However, constructing different elements requires a significant amount of cognitive cost<sup>15</sup>. FEM is doing quite well for many nonlinear problems, but solving the nonlinear problem by FEM involves assembling a complex tangent matrix and residual vector in the implicit FEM scheme. Furthermore, the explicit FEM scheme often faces conditional stability constraints, which demand small time increments<sup>16</sup>.

The past decade has witnessed a significant impact from artificial intelligence across a range of fields, especially deep learning. Various fields<sup>17,18,19,20,21,22</sup> are benefiting from deep learning, and computational solid mechanics is no exception<sup>23</sup>. One crucial aspect of integrating deep learning and mechanics is leveraging the powerful approximation capabilities of neural networks and the abundance of reliable big data to model complex relationships between inputs and outputs, such as constitutive models<sup>24,25,26,27</sup>, the prediction of the equivalent modulus of non-uniform materials<sup>28</sup>, inverse construction and topology optimization of metamaterials<sup>29,30,31</sup>. A model that is already trained can often achieve high efficiency and accuracy, without accounting for the training time, but its drawback is usually the low interpretability and the large amount of data required. Fitting the data with a neural network often results in poor model scalability, i.e., the neural network often needs to be retrained for different problems, and even the network structure may change drastically<sup>32</sup>. Moreover, the physical mechanism behind it is often not well understood<sup>33</sup>. This aspect of combination faces challenges in solving high-dimensional problems because it relies on existing methods to obtain data, which leads to the curse of dimensionality<sup>34</sup>. The universal approximation theorem states that multilayer feedforward neural networks with any nonconstant and bounded activation function and at least one hidden layer can act as universal approximators with arbitrary accuracy<sup>35,36</sup>. This theorem opens up a new way to solve PDEs, which is another aspect of combining deep learning and mechanics. Raissi et al.<sup>37</sup> proposed the most popular method in this direction, i.e., physics-informed neural networks (PINNs), although the idea of using the neural network to solve PDEs can be traced back to the last century<sup>38,39</sup>. PINNs are neural networks that incorporate partial differential equations (PDEs) into their loss function. The original PINNs considered the strong form of PDEs in solid mechanics called the deep collocation method (DCM)<sup>1,40</sup>. PINNs have been applied to various fields, such as solid mechanics<sup>41,26,42</sup>, fluid mechanics<sup>43,44</sup>, and biomechanics<sup>45,46</sup>. Moreover, Samaniego and Nguyen-Thanh et al.<sup>1</sup> presented a deep energy method (DEM)<sup>†</sup> where the loss function can be reformulated as an energy functional in solid mechanics with applications to linear elasticity<sup>1</sup>, fracture mechanics<sup>47,48,42</sup>, hyperelasticity<sup>49</sup>, viscoelasticity<sup>23</sup>, strain gradient elasticity<sup>50</sup>, elastoplasticity<sup>40</sup>. The core idea of DEM is that the principle of minimum potential energy can be used for optimization. PINNs have the advantage of generality, i.e., almost any PDEs can be solved by PINNs. However, they face the challenge in determining the optimal hyperparameters, especially in solid mechanics where the equations involve high-order tensors and derivatives. Although some recent studies have proposed methods for selecting hyperparameters<sup>51,52,32</sup>, DEM has the advantage of having fewer hyperparameters and achieving higher efficiency and accuracy due to lower order derivative than PINNs, but it is not applicable to all PDEs, as it is hard for some of them to derive an energy formulation. Moreover, DEM requires the prior construction of the field of interest due to the requirement of the variational principle<sup>53</sup>. Fuhg et al.<sup>54</sup> have shown that DEM can not solve the concentration feature like stress very well for finite strain hyperelasticity, so they propose a mixed deep energy method (mDEM). The core idea of mDEM is to add some extra loss terms, including the stress obtained by neural network output and the constitutive law describing the relationship between displacement and stress. Abueidda et al.<sup>55</sup> improve mDEM by introducing the Fourier transform to the input of neural network for promoting the perception of high-frequency function and incorporating both the strong form and energy form. To apply DEM, one needs to perform a successful integration over the domain defined by the collocation points<sup>23</sup>. The deep learning approach relies mainly on matrix-vector multiplications, which are highly optimized and greatly benefit from GPUs. However, the implicit FEM fail to fully exploit GPUs. As a result, high-performance GPUs provides research on the confluence of artificial intelligence and classical numerical method with great potential. In addition, developing nonlinear PINNs to solve PDEs is much simpler and faster than FEM<sup>56</sup>, attributing to the machine learning packages such as PyTorch<sup>57</sup> and TensorFlow<sup>58</sup>. Finally, a combination of data-driven and physics-informed deep learning approaches has been utilized to tackle incomplete and ill-posed problems in computational mechanics and other physics-based modelling

---

<sup>†</sup> In this work, DCM means the strong form of PINNs, DEM means the energy form of PINNs

disciplines. It is challenge for classical numerical methods to combine the data and physical laws<sup>59</sup>. In summary, PINNs and DEM have opened up a new avenue for solving partial differential equations and have significant research value.

In the linear theory of elasticity, the most critical variational principle is the dual extreme principle, i.e., the principle of minimum potential and complementary energy<sup>60</sup>. However, DEM currently lacks a complementary energy principle. It is well-known that the stress finite element (equilibrium element) plays a vital role in computational mechanics. Thus, proposing a deep energy method based on the principle of complementary energy is of utmost importance. To date, purely data-driven methods require large amounts of data, and it is not easy to surpass traditional finite element methods in terms of efficiency and accuracy if they solely rely on physical equations, even if the theory of generalized approximate functions shows great theoretical prospects. There is still much to be done to achieve this goal<sup>61</sup>. Recently, the practical application potential<sup>42,62,63</sup> of DeepONet<sup>64</sup> and FNO<sup>65</sup> has been receiving attention due to their basis in the universal approximation operator theory<sup>66</sup>. Goswami et al.<sup>42</sup> have indicated that the combination of DeepONet and DEM significantly improves computational efficiency and accuracy when solving fracture mechanics problems. Therefore, Semi-supervised learning, combined with operator and physical laws, has great potential in the future of data-driven approaches.

In this work, we propose a novel deep energy form based on the principle of minimum complementary energy (DCEM), instead of the traditional minimum potential energy principle. Our output function is the stress function, which naturally satisfies the equilibrium equation. This is the first attempt to leverage the power of the physics-informed neural networks (PINNs) energy form based on complementary energy. We further extend the capabilities of DCEM and propose a DCEM-Plus (DCEM-P) algorithm, where we add terms that naturally satisfy the biharmonic equation in the Airy stress function for better accuracy and efficiency compared to DCEM. We develop DCEM based on the DeepONet operator (DCEM-O), including branch net, trunk net, basis net, and particular net. The motivation behind DCEM-O is to harness and revive existing calculation results (data) and not waste previous calculation results to improve the computational efficiency of DCEM. The data is from our current or future high-fidelity numerical results and experiment data. The advantages of the DCEM are multi-fold :

- **Accuracy in Stress:** DCEM introduces a new energy form based on the minimum complementary energy principle, distinct from traditional DEM based on the minimum potential energy. This makes it a valuable supplement to existing DEM methods, offering improved accuracy, especially in stress predictions.
- **Enhanced Accuracy:** DCEM-Plus (DCEM-P) extends DCEM by incorporating terms that satisfy the biharmonic equation in the Airy stress function. This idea of DCEM-P can be applied to other methods of PINNs as well.
- **Computational Efficiency:** DCEM can be combined with physical equations and existing data through operator learning (DCEM-O). Leveraging additional data improves computational efficiency, making it a powerful and efficient approach, particularly with big data.
- **Convenient for Complex Displacement Boundaries:** DCEM's theoretical superiority over DEM in constructing admissible functions is particularly advantageous when dealing with complex displacement boundary conditions. It eliminates the need for constructing an admissible function field on the displacement boundary, simplifying the implementation process.

As a result, DCEM is an important supplement to the existing DEM. Additionally, DCEM can be combined with physical equations and existing data through operator learning (DCEM-O). The more data we have, the faster the DCEM-O calculation.

The outline of the paper is as follows. In Section 2, we introduce the prerequisite knowledge, including the feed-forward network, DeepONet algorithm, deep energy method, and the important stress functions in solid mechanics. In Section 3, we describe the methodology of the proposed method DCEM, DCEM-P and DCEM-O. In Section 4, we present the numerical result of the most common stress function, Prandtl and Airy stress function with the different boundary conditions under DCM, DEM, and DCEM:

1. The circular tube shows that DCEM can solve the problem dominated by displacement boundary well compared to existing methods such as DEM and PINNs strong form.
2. The wedge problem verifies DCEM has the feasibility of infinite problems, a challenging task for DEM, and DCEM is more accurate and efficient than PINNs strong form.

3. The non-uniform stretching force applied to the plate and the central hole showcases DCEM's competence in dealing with irregular geometries, outperforming DEM in both accuracy and efficiency, particularly in terms of stress prediction and stress concentration.
4. The Prandtl stress problem demonstrates DCEM's proficiency in solving full natural boundary conditions and torsion problems, making it a valuable tool in engineering applications.

The results demonstrate that DCEM exhibits better accuracy and efficiency in term of stress compared to DEM. DCEM has advantages in solving problems primarily influenced by the displacement boundary. Finally, Section 5 and Section 6 present some discussions of DCEM, concluding remarks, some limitations of DCEM such as we only deal with the linear elasticity problem without body force, and possible future work. In the Appendices, we show some important proofs of DCEM.

## 2 | PREREQUISITE KNOWLEDGE

### 2.1 | Introduction to feed-forward neural network

There are four primary types of neural networks: fully connected (also known as feed-forward neural networks), convolutional neural networks<sup>67</sup>, recurrent neural networks (with LSTM being the most commonly used), and the more recent Transformer<sup>68</sup>. The combination of machine learning and computational mechanics relies heavily on the powerful fitting capabilities of neural networks<sup>61,69</sup>. As a result, feed-forward neural networks remain the mainstream choice for scientific applications involving machine learning. Therefore, this article will focus mainly on the feed-forward neural network, which is essentially a nonlinear multiple linear regression model with added nonlinear capabilities through the activation function. The mathematical formula for the feed-forward neural network can be expressed as follows:

$$\begin{aligned}
 \mathbf{z}^{(1)} &= \mathbf{w}^{(1)} \cdot \mathbf{x} + \mathbf{b}^{(1)} \\
 \mathbf{a}^{(1)} &= \sigma(\mathbf{z}^{(1)}) \\
 &\vdots \\
 \mathbf{z}^{(L)} &= \mathbf{w}^{(L)} \cdot \mathbf{a}^{(L-1)} + \mathbf{b}^{(L)} \\
 \mathbf{a}^{(L)} &= \sigma(\mathbf{z}^{(L)}) \\
 \mathbf{y} &= \mathbf{w}^{(L+1)} \cdot \mathbf{a}^{(L)} + \mathbf{b}^{(L+1)},
 \end{aligned} \tag{1}$$

where  $\mathbf{x}$  is input,  $\mathbf{y}$  is output,  $\mathbf{z}$  is linear output. Activation function  $\sigma$  is applied to  $\mathbf{z}$ , and trainable parameters are  $\mathbf{w}$  and  $\mathbf{b}$ . Layers' neurons  $\mathbf{a}^{(l-1)}$  are linearly transformed to  $\mathbf{z}^{(l)}$ . Activation function  $\mathbf{a}^{(l)}$  is typically nonlinear (e.g., tanh). In this work, tanh function is used as activation function:

$$\tanh = \frac{e^x - e^{-x}}{e^x + e^{-x}}. \tag{2}$$

Notably, ReLU is not used due to physics-informed method involving high-order derivatives. Emperically, adding hidden layers doesn't necessarily improve accuracy.

### 2.2 | Introduction to DeepONet

DeepONet is an algorithm based on neural network operator learning. The mathematical structure is similar to polynomial and periodic function fitting

$$f(\mathbf{y}) = \sum_{i=1}^n \alpha_i \phi(\mathbf{y}_i). \tag{3}$$

The Trunk net is fitted with a neural network using the basis function  $\phi(\mathbf{y})$ . This approach shares a fundamental concept with PINNs, where the neural network fits from the coordinate space to the objective function. However, in DeepONet, the basis function is fitted instead of the objective function, and the constant weight  $\alpha$  in front of the basis function is fitted by

the branch net. Notably, the same input function of the branch net yields a fixed weight  $\alpha$ , which aligns with the function approximation concept in numerical analysis. In contrast to traditional function approximation algorithms that pre-select basis functions, DeepONet leverages neural networks to adaptively select the suitable basis functions based on the data.

Since Trunk net resembles PINNs, we can apply the automatic differential algorithm<sup>70</sup> in PINNs to construct a partial differential operator and obtain new loss function (strong form or energy principle) based on PDEs. In this work, we propose a semi-supervised combination of data operators and partial differential equations, which will be discussed in detail in DCEM-O Section 3.4. Next, we will introduce the network structure of DeepONet.

The network structure of DeepONet is similar to the theoretical results of the article on universal operator approximation in 1995<sup>64,66</sup>

$$|G(\mathbf{u})(\mathbf{y}) - \sum_{k=1}^p \sum_{i=1}^n c_i^k \sigma(\sum_{j=1}^m w_{ij}^k \mathbf{u}(\mathbf{x}_j) + b_i^k) \sigma(W^k \cdot \mathbf{y} + B^k)| < \epsilon, \quad (4)$$

where we can use the neural network to replace the item in Eq. (4)

$$\begin{cases} NN_B^k(\mathbf{u}(\mathbf{x}); \boldsymbol{\theta}_{NN}^B) &= \sum_{i=1}^n c_i^k \sigma(\sum_{j=1}^m w_{ij}^k \mathbf{u}(\mathbf{x}_j) + b_i^k) \\ NN_T^k(\mathbf{y}; \boldsymbol{\theta}_{NN}^T) &= \sigma(W^k \cdot \mathbf{y} + B^k) \\ NN_O(\mathbf{y}; \mathbf{u}) &= \sum_{k=1}^p NN_B^k(\mathbf{u}(\mathbf{x}); \boldsymbol{\theta}_{NN}^B) \cdot NN_T^k(\mathbf{y}; \boldsymbol{\theta}_{NN}^T), \end{cases} \quad (5)$$

where  $NN_B^k$ ,  $NN_T^k$ , and  $NN_O$  are the output of the branch net, trunk net and DeepONet respectively.  $\mathbf{u}(\mathbf{x})$  can be approximated from the sensor  $\mathbf{x}$ , i.e., discrete points approximate continuous function. For example, if the input  $\mathbf{u}(\mathbf{x})$  of  $NN_B$  is the gravitational potential energy of a three-dimensional cube material ( $[0, 1]^3$ ), the gravitational potential energy field in  $[0, 1]^3$  can take  $101^3$  at equal intervals of 0.01. The data structure of  $\mathbf{u}(\mathbf{x})$  is a variety of different structures, such as the data structure close to the image. Therefore, we can use corresponding network structures as the network architecture of the branch net, e.g., CNN with local features to deal with data similar to image and time-related RNN to deal with data strongly related to time. Noting that the network structure of branch net must consider the essence of the problem to select the appropriate network structure closest to the essence of the problem. Hence, we can find that  $\mathbf{u}(\mathbf{x})$  determines the output of the branch net in DeepONet, which is related to the weight  $\alpha$  in Eq. (3), and has no correlation with the coordinates we are interested in. Similarly, the coordinate completely determines the output of trunk net, which has the same characteristics as the basis function  $\phi(\mathbf{y})$  in Eq. (3). Therefore, DeepONet has many similar ideas to traditional function approximation.

For many details and extensions about DeepONet, please refer to this paper<sup>61</sup>.

## 2.3 | Introduction to deep energy method

The deep energy method (DEM)<sup>1</sup> is based on the principle of minimum potential energy in order to obtain the true displacement solution. The principle of minimum potential energy means that the true displacement field minimizes the potential energy functional  $J(\mathbf{u})$  among all the admissible displacement fields satisfying the displacement boundary conditions in advance. Note that the theory here is not only for the case of linear elasticity, but also for some nonlinear hyperelastic problems<sup>49</sup>. The formulation of DEM can be written as:

$$\begin{aligned} \boldsymbol{\theta}^* &= \arg \min_{\boldsymbol{\theta}} J(\mathbf{u}(\mathbf{x}; \boldsymbol{\theta})) \\ s.t. \quad \mathbf{u}(\mathbf{x}) &= \bar{\mathbf{u}}(\mathbf{x}), \mathbf{x} \subseteq \Gamma^u, \end{aligned} \quad (6)$$

where  $\mathbf{u}(\mathbf{x}; \boldsymbol{\theta})$  is approximated by neural network,  $\bar{\mathbf{u}}(\mathbf{x})$  is the given Dirichlet boundary  $\Gamma^u$  condition and

$$J(\mathbf{u}) = \int_{\Omega} \psi(\mathbf{u}) dV - \int_{\Omega} \mathbf{f} \cdot \mathbf{u} dV - \int_{\Gamma^t} \bar{\mathbf{t}} \cdot \mathbf{u} dA, \quad (7)$$

where  $\psi$ ,  $\Omega$ ,  $\mathbf{f}$ ,  $\bar{\mathbf{t}}$  and  $\Gamma^t$  is the strain energy density function, the domain, the body force, the surface force and Neumann boundary respectively. To be specific, the strain energy density in linear elasticity is

$$\begin{aligned} \psi &= \frac{1}{2} \boldsymbol{\varepsilon} : \mathbf{C} : \boldsymbol{\varepsilon} \\ \boldsymbol{\varepsilon} &= \frac{1}{2} (\nabla \mathbf{u} + \mathbf{u} \nabla). \end{aligned} \quad (8)$$

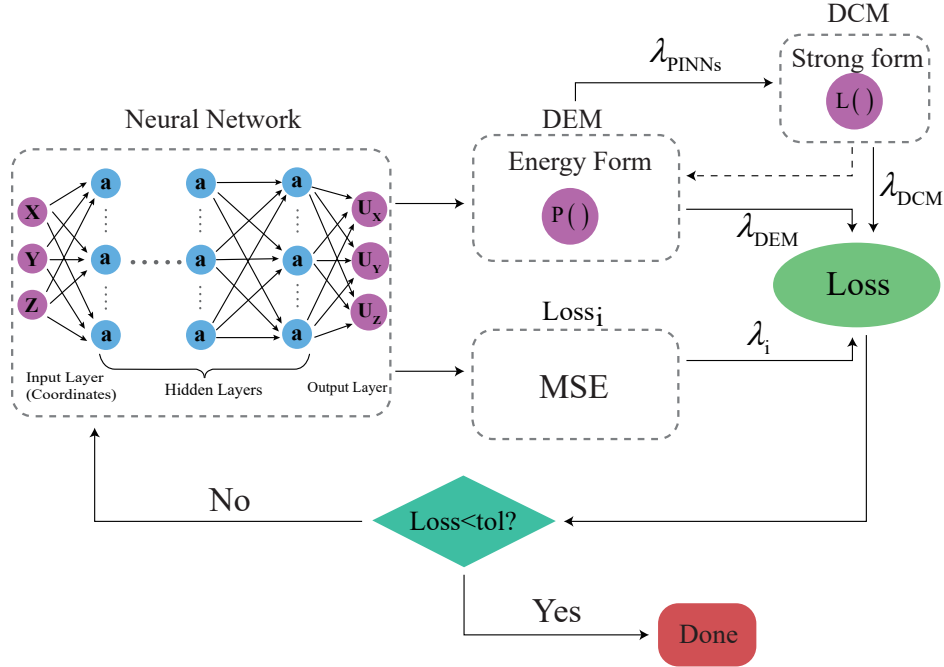


**FIGURE 1** Schematic of the difference and connection between DCM and DEM, purple circles in the Neural network are the inputs and outputs. Blue circles in the Neural network are the hidden neurons.  $P()$  is the energy density of the functional.  $Loss_i$  is the essential boundary loss. MSE is the mean square error to let the field of interest to satisfy the essential boundary. If the boundary condition is satisfied in advance,  $Loss_i$  can be dismissed.  $L()$  is the differential operator related to the strong form of PDEs.  $\lambda_{DCM}$  and  $\lambda_{DEM}$  are the weight of the loss of DCM and DEM.  $\lambda_i$  is the weight of  $Loss_i$  (including initial condition if temporal problem). Note that the number of  $\lambda_{DCM}$  is determined by the number of PDEs. The dotted arrow means not all PDEs can be converted to the energy form.

In the context of nonlinear elasticity, particularly in hyperelasticity, the strain energy density function, denoted as  $\psi$ , can be formulated based on the deformation gradient  $\mathbf{F}$  or Green-Lagrange strain tensor  $\mathbf{G}$  ( $\mathbf{G} = (\mathbf{F}^T \mathbf{F} - \mathbf{I})/2$ ). For detailed conceptualization of the strain energy density form in hyperelasticity, readers may refer to these papers<sup>15,71,72,73</sup>.

From a physical perspective, DEM can be applied not only to reversible systems like hyperelasticity but also to dissipative systems such as viscoelasticity<sup>23</sup> and elastoplasticity<sup>40</sup>. Mathematically, many partial differential equations (PDEs) have corresponding weak forms that are obtained through integration by parts.

The idea in DEM is simple but effective. DEM uses a neural network to replace the approximation function like the trial function in FEM. A neural network is used to approximate the displacement function over the physical domain of interest. Due to the rich function space of the neural network, DEM can have a better performance compared to the traditional methods theoretically, regardless of the optimization error. DEM is the energy form of physics-informed neural networks (PINNs). In the traditional PINNs, DCM construct the physical loss by the strong form of the PDEs directly<sup>41</sup>. However, the differential equations in solid mechanics are high-order tensors and high-order derivatives. If we use the energy form of the PINNs, the accuracy and efficiency are commonly higher than the strong form. Fig. 1 shows the difference and connection between DCM and DEM.

In DEM, we must construct the admissible displacement in advance before using the principle of minimum potential energy. The distance function  $\mathbf{d}(\mathbf{x})$  can be applied to satisfy the requirement of the admissible displacement:

$$\mathbf{u}(\mathbf{x}) = \bar{\mathbf{u}}(\mathbf{x}) + \mathbf{d}(\mathbf{x}) \odot \mathbf{u}_g(\mathbf{x}), \quad (9)$$

where  $\odot$  is element-wise, i.e., multiplication of corresponding elements does not change the shape, and  $\mathbf{u}_g(\mathbf{x})$  is a general function, which is neural networks in DEM. The distance function is a special and currently common way to satisfy boundary condition in advance<sup>15,49,74,75,76,38</sup>. And the distance function  $d(\mathbf{x})$  is to give the nearest distance from the point  $\mathbf{x}$  (domain without boundary or boundary) to Dirichlet boundary. The label of the distance  $y^{(i)}$  can be obtained from the traditional method (dataset:  $\{\mathbf{x}^{(i)}, y^{(i)}\}_{i=1}^n$ ), such as kd-tree. Then we use the NN to fit the label, i.e.,

$$d(\mathbf{x}) \approx NN(\mathbf{x}; \boldsymbol{\theta})$$

$$\boldsymbol{\theta} = \arg \min_{\boldsymbol{\theta}} \mathcal{L} = \sum_{i=1}^n [NN(\mathbf{x}^{(i)}) - y^{(i)}].$$

The NN to fit the distance can be used to solve the complex boundary problem<sup>77</sup>. Besides, there is another easier way to satisfy boundary conditions than using the distance constraint, i.e., the soft constraint way<sup>78</sup>. The soft constraint method is usually implemented by a penalty loss, i.e.  $\beta \int_{\Gamma} (\mathbf{u} - \bar{\mathbf{u}})^2 d\Gamma$ , where  $\beta$  is the hyperparameter of the boundary loss, and  $\bar{\mathbf{u}}$  is the given condition on the boundary. However, it is a way that the boundary condition can not be satisfied exactly, and different penalty factor  $\beta$  results in the different numerical results.

## 2.4 | Introduction to stress function

The stress function method is an extension of the well-known stress solution in solid mechanics, which aims to automatically satisfy the equilibrium equations. When solving elasticity problems, there are two main methods: the displacement method and the stress method. While there is also a strain solution method, it is less commonly used because strain and stress are linearly related in elastic mechanics problems, making the difficulty of the strain solution equivalent to that of the stress solution.

In the stress method, the stress must satisfy the equilibrium equations, but by using a stress function, the equilibrium equations are automatically satisfied. This not only reduces the number of equations in the stress solution but also maintains the advantages of the stress method. The advantages of the stress method yield more precise stress results, like in equilibrium elements. However, the stress method necessitates higher-order trial functions and complex integration processes to determine the displacement field, which is more complicated than taking derivatives. Therefore, the stress function solution plays a significant role in solving problems in elastic mechanics, especially stress. To better understand the stress function, we briefly introduce displacement and stress solutions of elastic mechanics. For detailed conceptualization of methods to solve the elastic mechanic's problems, readers may refer to this book<sup>79</sup>. The stress function method is primarily used to solve linear elastic problems in traditional solid mechanics and has limited effectiveness in solving nonlinear problems. There are two reasons resulting in the difficulty to apply stress function method to nonlinear problem including geometric and material nonlinearity. In nonlinear mechanics, the material nonlinearity makes it challenging to directly apply the stress function method. To apply stress function method, the strain should be expressed by stress. Besides, the geometric equations, i.e.,

$$\mathbf{G} = \frac{1}{2} [\nabla \mathbf{u} + \mathbf{u} \nabla + (\mathbf{u} \nabla)^T (\mathbf{u} \nabla)], \quad (10)$$

contain a nonlinear term for displacement in geometrically nonlinear problems, and the nonlinear term is  $(\mathbf{u} \nabla)^T (\mathbf{u} \nabla)$ . In the case of small strain linear elasticity, the nonlinear term in Eq. (10) becomes negligible, leading us to disregard this nonlinear term. Consequently, the geometric equations simplify to the form presented in Eq. (11). The governing equations of stress function are expressed by geometric equations. As a result, if the problem is a nonlinear problem, the governing equations of stress function not only become complex but also different materials referred to different forms of constitutive law should have different corresponding governing equations of stress function in nonlinear problems. Thus, this makes the stress function approach difficult to apply to nonlinear problems. Hence, we only solve the linear problems by stress function in this work.

In the displacement method, the primary unknown quantity to be solved is the displacement field, denoted as  $\mathbf{u}$ . In contrast, stress is the basic unknown quantity in stress solution. We substitute the strain tensor obtained by geometrical equations

$$\boldsymbol{\varepsilon} = \frac{1}{2} (\nabla \mathbf{u} + \mathbf{u} \nabla) \quad (11)$$

into the linear constitutive equations, i.e., Hooke's law

$$\boldsymbol{\sigma} = \mathbf{C} : \boldsymbol{\varepsilon}, \quad (12)$$

where  $\mathbf{u}$ ,  $\nabla$ ,  $\boldsymbol{\sigma}$ ,  $\mathbf{C}$  and  $\boldsymbol{\varepsilon}$  is the displacement field, gradient operator, stress tensor, elasticity tensor, and strain tensor. Thus, we can express the stress  $\boldsymbol{\sigma}$  in terms of displacement  $\mathbf{u}$  in the equilibrium equation

$$\nabla \cdot \boldsymbol{\sigma} + \mathbf{f} = 0, \quad (13)$$

where  $\mathbf{f}$  is the body force, such as gravity.  $\rho$  and  $\ddot{\mathbf{u}}$  are the density and acceleration.  $\nabla \cdot ()$  means divergence operator.

We solve the equilibrium equations represented by the displacement, called Navier-Lamé equations (LN equations), which is the displacement solution method. LN equations can be written in the form

$$\begin{cases} Gu_{i,jj} + (\lambda + G)u_{j,ji} + f_i = 0 & \mathbf{x} \in \Omega \\ u_i = \bar{u}_i & \mathbf{x} \in \partial\Omega, \end{cases} \quad (14)$$

where the comma notation “,” indicates partial derivatives, such as  $u_{x,x} = \partial u_x / \partial x$ , and the subscripts  $i, j$  conforms to the Einstein notation, such as  $\sigma_{kk} = \sigma_{xx} + \sigma_{yy} + \sigma_{zz}$  and  $u_i$  means  $i$  can be  $\{x, y, z\}$ .  $\lambda$  and  $G$  are Lamé parameters

$$\begin{cases} \lambda = \frac{\nu E}{(1+\nu)(1-2\nu)} \\ G = \frac{E}{2(1+\nu)}, \end{cases} \quad (15)$$

where  $E$  and  $\nu$  represent the Young modulus and Poisson ratio respectively. We can get the solution of  $\mathbf{u}$  by solving Eq. (14) with well-defined boundary conditions, which we called the displacement method because our solution variable is only the displacement  $\mathbf{u}$ . When only displacement boundary conditions are applied, the displacement method is preferred over the stress method.

The stress method is an approach in which stress  $\boldsymbol{\sigma}$  is the primary unknown quantity to be determined. We substitute the constitutive equations into Saint-Venant compatibility equations

$$\nabla \times \boldsymbol{\varepsilon} \times \nabla = 0, \quad (16)$$

where  $\nabla \times$  denotes the curl operator. In the constitutive equations, strain is expressed in terms of stress

$$\varepsilon_{ij} = \frac{1+\nu}{E} \sigma_{ij} - \frac{\nu}{E} \sigma_{kk} \delta_{ij}, \quad (17)$$

where  $\delta_{ij}$  is the Kronecker delta, which means  $\delta_{ij} = 1$ , only when  $i = j$  (not summed). The compatibility equations guarantee single-valued and continuous displacement. We can rewrite Eq. (16) in terms of stress  $\boldsymbol{\sigma}$  as

$$\nabla^2 \sigma_{ij} + \frac{1}{1+\nu} \theta_{,ij} = -(f_{i,j} + f_{j,i}) - \frac{\nu}{1-\nu} \delta_{ij} f_{k,k}, \quad (18)$$

where  $\theta = \sigma_{kk}$ . Eq. (18) are known as the Beltrami-Michell compatibility equations (BM equations). Note that the BM equations are dependent, which means the independent equations are less than 6 if the problem is 3D. Because the number of the basic unknowns (stress) is 6, we need to add the additional equations, i.e., the equilibrium equations in terms of stress, to make the equation closed. Thus the closed equations of elastostatics problem in stress solution can be summarized as:

$$\begin{cases} \nabla^2 \sigma_{ij} + \frac{1}{1+\nu} \theta_{,ij} + (f_{i,j} + f_{j,i}) + \frac{\nu}{1-\nu} \delta_{ij} f_{k,k} = 0 & \mathbf{x} \in \Omega \\ \sigma_{ij,i} + f_j = 0 & \mathbf{x} \in \Omega \\ \sigma_{ij} n_j = \bar{t}_i & \mathbf{x} \in \partial\Omega, \end{cases} \quad (19)$$

where we only consider the Neumann boundary conditions (specified surface tractions) because the stress solution is quite difficult to deal with displacement boundary conditions due to boundary integrals.



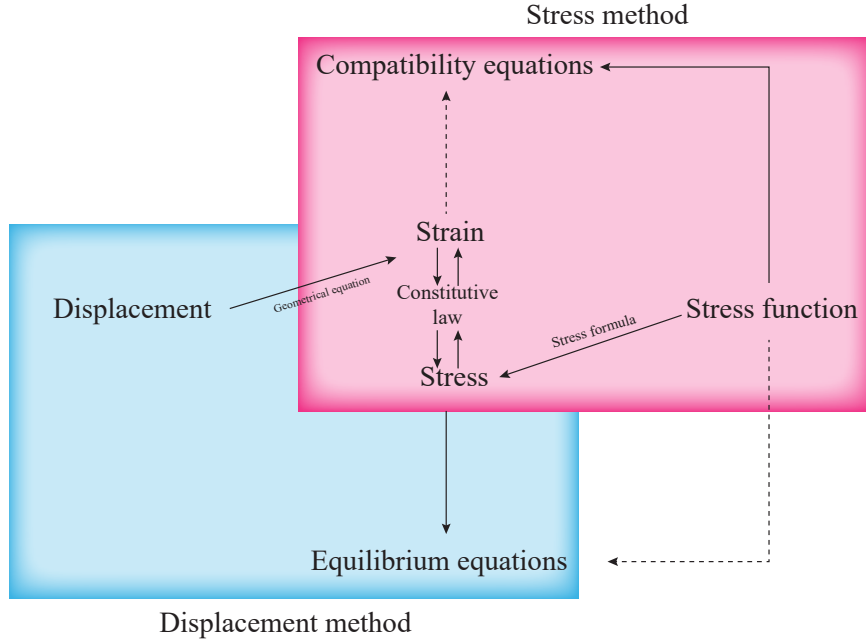


**FIGURE 2** The relation between displacement and stress solution. The black solid line arrow is the derivation process; the dotted arrow indicates that the equation is automatically satisfied

In order to solve the non-independence problem of the stress solution in Eq. (34), we can use some tricks, i.e., Bianchi Identity

$$\begin{aligned} L_{ij,j} &= 0 \\ L_{ij} &= e_{ink}e_{jml}\Phi_{mn,kl}, \end{aligned} \quad (20)$$

where  $e_{ijk}$  is the permutation symbol. Since the characteristic of  $L_{ij}$  satisfy the similar form of equilibrium equation, the stress function  $\Phi$  can be used to be the basic unknown variable instead of stress. Then, Eq. (13) in the absence of body forces can be expressed as:

$$\begin{cases} \nabla^2(e_{ink}e_{jml}\Phi_{mn,kl}) + \frac{1}{1+\nu}(e_{pnk}e_{pml}\Phi_{mn,kl})_{,ij} = 0 & \mathbf{x} \in \Omega \\ (e_{ink}e_{jml}\Phi_{mn,kl})n_j = \bar{t}_i & \mathbf{x} \in \partial\Omega \end{cases}, \quad (21)$$

where the stress function  $\Phi_{ij}$  (symmetry) has 3 independent components in three-dimensional elasticity. Eq. (21) above is the stress function method, which is the other form of the stress solution. There are  $C_6^3 - 3 = 17$  possible choices of the stress function. The reason for subtracting 3 is that there are 3 combinations that automatically satisfy Eq. (21). The most common choices of the stress function are Maxwell stress function and Morera stress function,

$$\Phi_{Maxwell} = \begin{bmatrix} \Phi_{11} & 0 & 0 \\ & \Phi_{22} & 0 \\ Sym & & \Phi_{33} \end{bmatrix}; \Phi_{Morera} = \begin{bmatrix} 0 & \Phi_{12} & \Phi_{13} \\ & 0 & \Phi_{23} \\ Sym & & 0 \end{bmatrix}. \quad (22)$$

To our best knowledge, this is the first attempt to leverage the power of DEM based on the principle of the complementary energy method, so we focus on the most common two-dimensional problems in solid mechanics, i.e., the plane state of stress or strain and torsion problems. Fig. 2 shows the relation between displacement and stress solution.

In the two-dimensional stress and strain problems, the Maxwell stress function can be reduced to the Airy stress function, i.e.,  $\Phi_{11} = \Phi_{22} = 0, \Phi_{33} \neq 0$ . Besides, in the torsion problem of the cylindrical body, the Morera stress function can be

reduced to the Prandtl stress function, i.e.,  $\Phi_{12} = \Phi_{13} = 0$ ,  $\partial\Phi_{23}/\partial x \neq 0$ , which is shown in Eq. (23).

$$\Phi_{Airy} = \begin{bmatrix} 0 & 0 & 0 \\ 0 & 0 & 0 \\ Sym & \Phi_{33} & \end{bmatrix}; \Phi_{Prandtl} = \begin{bmatrix} 0 & 0 & 0 \\ 0 & \Phi_{23} & \\ Sym & 0 & \end{bmatrix} \quad (23)$$

### 2.4.1 | Airy stress function

Airy stress function is a special and simple form of the Maxwell stress function for plane problems. Only the stress function component  $\Phi_{33}$  of the Maxwell stress function is not zero, so we use Airy function  $\phi_A$  to replace the only Maxwell stress function not equal to zero. Thus, the Eq. (21) can be simplified to

$$\begin{cases} \nabla^2 \nabla^2 \phi_A = -(1-\nu) \nabla^2 V & \mathbf{x} \in \Omega \\ l \left( \frac{\partial^2 \phi_A}{\partial y^2} + V \right) - m \left( \frac{\partial^2 \phi_A}{\partial x \partial y} \right) = \bar{t}_x & \mathbf{x} \in \partial\Omega, \\ -l \left( \frac{\partial^2 \phi_A}{\partial x \partial y} \right) + m \left( \frac{\partial^2 \phi_A}{\partial x^2} + V \right) = \bar{t}_y & \mathbf{x} \in \partial\Omega \end{cases} \quad (24)$$

where  $l$  and  $m$  are the direction cosines of the outer normal to the boundary curve;  $\bar{t}_x$  and  $\bar{t}_y$  are the surface tractions acting on the boundary surface;  $\nabla^2 \nabla^2$  is a biharmonic operator, which is expressed in the Cartesian coordinate system as :

$$\nabla^2 \nabla^2 = \frac{\partial}{\partial x^4} + 2 \frac{\partial}{\partial x^2 \partial y^2} + \frac{\partial}{\partial y^4}. \quad (25)$$

Note  $V$  is the potential of the body force, and the Airy stress function can only solve problems with the potential of the body force, and can not directly deal with displacement boundary conditions. If the problem has displacement boundary conditions, we can use Saint Venant's theory to transform the displacement (Dirichlet) boundary into the force boundary condition. The stress is expressed by the Airy stress function as

$$\begin{cases} \sigma_{xx} = \frac{\partial^2 \phi_A}{\partial y^2} + V \\ \sigma_{yy} = \frac{\partial^2 \phi_A}{\partial x^2} + V \\ \sigma_{xy} = -\frac{\partial^2 \phi_A}{\partial x \partial y} \end{cases} \quad (26)$$

The Airy stress function has the following important properties :

1. A difference of a linear function in Airy stress function does not affect its solution, as the lowest derivative order of Eq. (24) is two without body force, so the linear function will not affect the solution result.
2. The value of the Airy stress function is the moment of the external force from the reference point to the current position at the boundary, and the directional derivative of the Airy stress function is the integral of the external force vector. This property is significant to guess the formation of the Airy stress function, as we explain in Fig. 3a.

### 2.4.2 | Prandtl stress function

Prandtl stress function is a special form of the Morera stress function to deal with the torsion problem of a cylindrical body, as shown in Fig. 3b. Only the stress function component  $\Phi_{23}$  of the Morea stress function is not zero, so we use Prandtl function  $\phi_P$  to replace the only Morea stress function not equal to zero. Thus, the Eq. (21) can be simplified to

$$\begin{cases} \nabla^2 \phi_P = -2G\alpha & \mathbf{x} \in \Omega \\ M_t = 2 \iint \phi_P dx dy & \mathbf{x} \in \Omega, \\ \phi_P = C & \mathbf{x} \in \partial\Omega \end{cases} \quad (27)$$

where  $\alpha$  is the rate of twist, i.e.  $\alpha = d\theta/dz$ .  $G$  is one of the Lamé parameters, i.e., the shear modulus, and  $M_t$  is the torque acting on the boundary condition at the ends  $z = H$ .  $M_t = 2 \iint \phi_P dx dy$  is the boundary condition at the ends of the

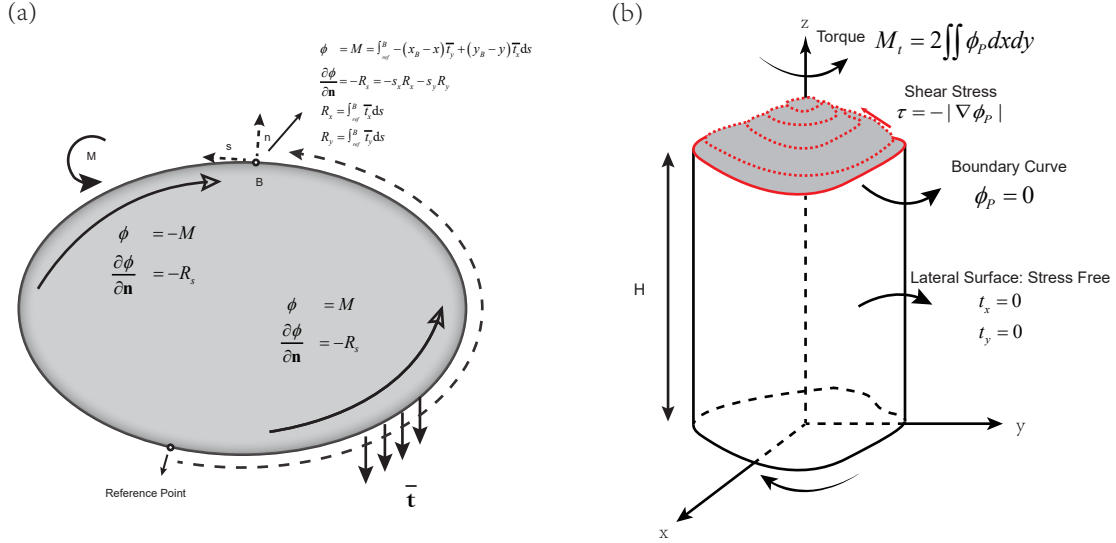


**FIGURE 3** The illustration of Airy and Prandtl stress function: (a) The value of the Airy stress function: the reference point means  $\phi_A = \partial\phi/\partial x = \partial\phi/\partial y = 0$ .  $\bar{t}$  is the surface force.  $\mathbf{n}$  and  $\mathbf{s}$  is the normal and tangential direction, respectively.  $R_x$  ( $R_y$ ) means the integral of the surface force in the  $x$  ( $y$ ) direction at the boundary from the reference point to the current position  $B$ .  $M$  is the moment of the external force about the current point at the boundary from the reference point. Counterclockwise is the positive direction of the moment. When counterclockwise at the boundary,  $\phi$  is equal to  $M$ . However,  $\phi$  is equal to  $-M$  as clockwise. (b) The value of the Prandtl stress function: the red lines represent the contours of the Prandtl stress function. The value of shear stress is equal to the negative gradient of the Prandtl stress function. The direction of the shear stress points is the tangent direction of the contour of the Prandtl stress function. The Prandtl stress is equal to the constant (we usually choose zero) on the boundary.

cylindrical.  $\phi_p = C$  is the lateral surface boundary condition without surface force, and no loss of generality is involved in setting  $\phi_p = 0$  in a connected region ( $\phi_p = 0$  in a connected region by default unless otherwise stated). Note that  $\alpha$  is unknown, so we usually solve

$$\begin{cases} \nabla^2 \phi_p = -2G\alpha & \mathbf{x} \in \Omega \\ \phi_p = 0 & \mathbf{x} \in \partial\Omega \end{cases} \quad (28)$$

first with an unknown constant  $\alpha$ . We can readily get  $\phi_p$  with a unknown constant  $\alpha$ , because the equation is the standard Poisson equation (there are many well-establish methods in potential theory<sup>80</sup> to help us to solve it). Then we substitute  $\phi_p$  with a unknown constant  $\alpha$  into  $M_t = 2 \iint \phi_p dx dy$ , and we can solve for  $\alpha$  eventually. The relation between Prandtl stress function and the stress in the Cartesian coordinate system can be expressed as:

$$\begin{cases} \tau_{zx} = \frac{\partial \phi_p}{\partial y} \\ \tau_{zy} = -\frac{\partial \phi_p}{\partial x} \end{cases} \quad (29)$$

The Prandtl stress function has important properties as shown in Fig. 3b. We can use the minimum complementary energy variation principle to convert it into the corresponding energy form. In the next section, we introduce the principle of minimum complementary energy we use.

### 3 | METHOD

In this section, we introduce the principle of minimum complementary energy. The proposed DCEM mainly uses neural networks to fit the admissible stress function field. However, note that constructing the admissible Airy stress function field

is more intricate compared to constructing the admissible displacement field based on the principle of minimum potential energy.

### 3.1 | Introduction to the principle of minimum complementary energy

The above displacement and stress solutions are strong forms. From the variational formulation, we can get energy form of stress solution. The traditional deep energy form is based on the principle of minimum potential energy. There is another important energy principle in solid mechanics called the principle of minimum complementary energy. However, there is currently no research on deep energy algorithms for complementary energy principle.

The minimum complementary energy principle is a variational principle with stress function or stress as the basic unknown variable. The complementary energy  $\Pi_c$  is composed of the complementary strain energy  $U_c$  and the complementary potential  $V_c$ , and its expression is:

$$\Pi_c = U_c + V_c. \quad (30)$$

The strain complementary energy  $U_c$  is the integrated overall energy of the complementary strain energy density  $W_c$  on the solution domain, and  $W_c$  expression is:

$$U_c = \int_{\Omega} W_c d\Omega \quad (31)$$

The density of complementary strain energy  $W_c$  is the energy density in the integral form of stress as the basic unknown variable, and its expression is:

$$W_c = \int_{\sigma_{ij}} \varepsilon_{ij} d\sigma_{ij}. \quad (32)$$

The complementary potential  $V_c$  is expressed as

$$V_c = - \int_{\Gamma^u} \bar{u}_i p_i d\Gamma, \quad (33)$$

where its calculation method is the given essential displacement boundary condition  $\bar{\mathbf{u}}$  multiplied by the constraint reaction force  $\mathbf{p} = \mathbf{n} \cdot \boldsymbol{\sigma}$  with the stress field as the basic unknown quantity, and its physical meaning is the excess energy absorbed by the support system or transmitted to other objects by the support system.

The admissible stress field must satisfy the given force boundary conditions and equilibrium equations

$$\begin{cases} \nabla \cdot \boldsymbol{\sigma} + \mathbf{f} = 0 \\ \boldsymbol{\sigma} \cdot \mathbf{n} = \bar{\mathbf{t}}, \end{cases}, \quad (34)$$

in advance. However, it is challenging to construct the admissible stress field in advance because the equilibrium equations are not easy to satisfy. Thus, it is common to use the stress function method to replace the stress field because the stress function naturally satisfies the equilibrium equations. Only the force boundary conditions instead of equilibrium equations should be considered. We put admissible stress function  $\phi_{admiss}$  into Eq. (30), and optimize the complementary energy functional to minimize it:

$$\phi_{true} = \arg \min_{\phi_{admiss}} \Pi_c(\phi_{admiss}). \quad (35)$$

For nonlinear problems, the key to use the principle of minimum complementary energy is the transformation of the first Piola stress (Lagrange's stress) and the deformation gradient  $\mathbf{F}$ <sup>60</sup>. If the principle of minimum potential energy can solve the nonlinear problem, then the problem must be solved by the principle of minimum complementary energy, which is proved in [Appendix A](#); in addition, in mathematics, strain energy and strain complementary energy are essentially Legendre transformations, which we also prove in [Appendix A](#).

### 3.2 | DCEM: Deep complementary energy method based on the principle of minimum complementary energy

Unlike the minimum potential energy using the neural network to approximate the displacement field, we use a neural network to approximate the stress function. Then the complementary energy is optimized to the minimum by the principle of minimum complementary energy. Unfortunately, not all stress functions satisfy the conditions of the given force boundary conditions in advance. Therefore, if we use the principle of minimum complementary energy, admissible stress functions that satisfy the force boundary conditions must be constructed in advance. Therefore, the key to the DCEM lies in the construction of admissible stress functions. The expressions of the admissible stress functions can be written as:

$$\phi_i(\mathbf{x}) = NN_{p(i)}(\mathbf{x}) + \sum_{m=1}^n NN_{g(i)}^{(m)}(\mathbf{x}) * NN_{b(i)}^{(m)}(\mathbf{x}), \quad (36)$$

where  $NN_p$  is the particular solution network only satisfying the non-homogeneous force boundary condition as  $\mathbf{x}$  at the force boundary condition;  $NN_g$  is the generalized network (no special requirement like particular solution network and basis function network  $NN_b$ ), and  $NN_b$  is the basis function network related to different stress functions such as Airy and Prandtl stress function. The three types are analogous to boundary networks, generalized networks, and distance networks, respectively, of admissible displacement fields in<sup>81,77,76</sup>. It is worth noting that distance networks are a special case of basis function networks. Any function can be used as the distance function as long as the distance function is zero at the given displacement boundary in the admissible displacement field. Thus, the distance function is not unique, which will be discussed in detail in Section 5.1. It is possible to use different distance functions to construct the admissible field to decrease the approximation error theoretically<sup>64</sup>. In the Prandtl stress function, the construction of the admissible stress function is the same as the construction of the displacement field, while the construction of admissible Airy stress function is more complicated than the construction of admissible displacement. The admissible displacement field should consider the Dirichlet boundary condition (the displacement boundary), while the admissible stress function should consider the Neumann boundary condition (the force boundary). But in the Airy stress function, not only the basis function is zero at the given force boundary, but also the normal derivative of the basis function is required to be zero at the force boundary, which is shown in Appendix C. Compared with the admissible displacement field, the basis function in the Airy stress function has the extra condition that the normal derivative is zero, mainly due to the relationship between the stress function and the stress. As a result, the basis function is related to the different stress function.

In the Airy stress function, the basis function can be obtained from the distance function, defined as:

$$NN_b = \lambda * Dis^{order}, \quad (37)$$

where

$$\begin{cases} Dis(x) = 0, x \in \Gamma^t \\ Dis(x) \neq 0, x \in \Omega \end{cases}, \quad (38)$$

$\Gamma^t$  represents the boundary of the domain, and  $\Omega$  is the domain itself. The parameter *order* is a real number greater than 1 (in this example, *order* = 2), and  $\lambda$  is a scalable factor ( $\lambda = 1/Maxdis^{order}$ ) used for the normalization of the basis function. The construction of the basis function ensures that it satisfies the conditions  $B(x) = 0$  and  $\partial B(x)/\partial \mathbf{n} = 0$  when  $\mathbf{x} \in \Gamma^t$ , because:

$$\frac{\partial NN_b}{\partial \mathbf{n}} = \lambda * order * Dis^{order-1} \frac{\partial Dis}{\partial \mathbf{n}} = 0, x \in \Gamma^t. \quad (39)$$

This property ensures that the basis function satisfies the natural boundary conditions, making it suitable for basis function in the Airy stress function, as is shown in Section 4.1.2.

There are many ways of constructing admissible stress function in theory, such as Coefficient function method and Eq. (36) (Basis function method). Coefficient function method is to construct many admissible basis functions fields (such as the orthogonal polynomials, i.e., Legendre polynomials, Chebyshev polynomials, periodic polynomials) satisfying the homogeneous boundary conditions in the given force boundary condition, then fit the constants in front of the basis functions. Eq. (36) is based on the idea of distance function, but it needs to meet the condition that the normal derivative is zero additionally in Airy stress function, as explained in Appendix C. Of course, the "omnipotent" penalty function

**TABLE 1** The different methods for constructing admissible stress function in Airy stress function.  $\Gamma^f$  means the force boundary condition. Homogeneous force boundary condition (HFB) means when  $\mathbf{t}(\mathbf{x}) = 0$  when  $\mathbf{x} \in \Gamma^f$ , and non-homogeneous force boundary condition (non-HFB) means when  $\mathbf{t}(\mathbf{x}) = \bar{\mathbf{t}}$  when  $\mathbf{x} \in \Gamma^f$

Methods in Airy stress function	$\phi(\mathbf{x}) = A(\mathbf{x}) + B(\mathbf{x}) * C(\mathbf{x})$		
	$A(\mathbf{x})$	$B(\mathbf{x})$	$C(\mathbf{x})$
Coefficient function method		Constant trainable parameters	Satisfy HFB when $\mathbf{x} \in \Gamma^f$
Basis function method	Satisfy non-HFB ( $\mathbf{x} \in \Gamma^f$ )	$B(\mathbf{x}) = 0; \partial B(\mathbf{x})/\partial \mathbf{n} = 0$ ( $\mathbf{x} \in \Gamma^f$ )	Neural network
Penalty function method		$\mathcal{L}_p = \beta_1[\hat{\phi}(\mathbf{x}) - \phi(\mathbf{x})]^2 + \beta_2[\partial \hat{\phi}(\mathbf{x})/\partial \mathbf{n} - \partial \phi(\mathbf{x})/\partial \mathbf{n}]^2$	

method can also be used to construct the admissible stress function. Table 1 shows the different methods for constructing admissible stress functions.

The algorithm flow of DCEM is:

1. According to the force boundary conditions, we construct the admissible stress function. When dealing with the Airy stress function, we can choose one of the methods for constructing the admissible stress function in Table 1. If we choose the basic function method in Table 1. The particular solution network should be trained, and training points are  $\{\mathbf{x}_i \in \Gamma^f, \bar{\mathbf{t}}_i\}_{i=1}^n$ , so that the particular solution network can fit the force boundary condition. For example, the force boundary condition expressed by the Airy stress function for the plane stress problem is:

$$\begin{aligned} n_x \left( \frac{\partial^2 NN_p}{\partial y^2} + V \right) - n_y \left( \frac{\partial^2 NN_p}{\partial x \partial y} \right) &= \bar{t}_x \\ -n_x \left( \frac{\partial^2 NN_p}{\partial x \partial y} \right) + n_y \left( \frac{\partial^2 NN_p}{\partial x^2} + V \right) &= \bar{t}_y, \end{aligned} \quad (40)$$

and the property of the Airy stress function can be used to construct the particular solution network, i.e.,  $\phi = M$  and  $\partial \phi / \partial \mathbf{n} = -R_s$ , as shown in Fig. 3 and proof in Appendix B. If it is a free torsion problem, the particular solution network must ensure that the Prandtl stress function at the boundary conditions is constant. It is convenient to set the particular solution network  $NN_p$  to be zero when dealing with the connected region. Noting that through the properties of the Airy stress function in Section 2.4.1, it is feasible to obtain the particular solution, which is equivalent to Eq. (40), as shown in proof Appendix B.

2. Using the principle of the minimum complementary energy, we get certain admissible stress function by AD algorithm in Pytorch when the loss function (complementary energy is obtained by using numerical integration, we use simpson integration in this paper) converges .
3. According to relation between stress and stress function, we get the stress by AD algorithm.

It is worth noting that, according to the minimum complementary energy principle, the admissible stress function needs to satisfy the force boundary condition in advance; according to the minimum potential energy principle, the admissible displacement field in the deep energy method needs to satisfy the displacement boundary condition in advance. Therefore, in theory, if displacement boundary conditions mainly dominate the boundary conditions of this problem, it would be more appropriate to use the principle of minimum complementary energy because there are fewer constraints on the admissible stress function field than the admissible displacement field in the minimum potential energy principle, so the powerful fitting ability of the neural network can be released because the form of the admissible function field through the distance function will limit the function space of the neural network to a certain extent. In contrast, if force boundary conditions dominate the problem, it will be more advantageous to use the principle of minimum potential energy because the assumptions on the displacement function are reduced.

### 3.3 | DCEM-P: DCEM with biharmonic function in Airy stress function

The strong form of the Airy stress function satisfies the biharmonic equation

$$\nabla^4 \phi = 0. \quad (41)$$

We can add some terms  $\phi_{bh}$  naturally satisfying Eq. (41), such as  $x^2, y^2$ . The trainable parameters  $a_i$  before these terms can be determined by the loss function (the complementary energy  $\Pi_c$ ), i.e.

$$\begin{aligned} \phi^{true} &= \arg \min_{a_i, \theta_{NN_g^{(m)}}} \Pi_c(\phi) \\ \phi(\mathbf{x}) &= NN_p(\mathbf{x}; \theta_{NN_p^{(m)}}) + \sum_{m=1}^n NN_g^{(m)}(\mathbf{x}; \theta_{NN_g^{(m)}}) * NN_b^{(m)}(\mathbf{x}; \theta_{NN_b^{(m)}}) + \sum_{i=1}^s a_i * \phi_{bh}^i. \end{aligned} \quad (42)$$

The result presented later shows that DCEM-P can converge faster and be more accurate than DCEM. Because the DCEM is similar to DCEM-P, we only present the algorithm of DCEM-P in [Algorithm 1](#).

---

**Algorithm 1** The algorithm of DCEM-P

---

- 1: **Step 1:** Training the particular net  $NN_p$ .
  - 2: Allocate training points on the force boundary conditions, i.e.,  $\{\mathbf{x}_i \in \Gamma^t, \bar{t}_i\}_{i=1}^n$ .
  - 3: **if** Prandtl stress function: **then**
  - 4:    $NN_p = 0$  (connected region).
  - 5: **end if**
  - 6: **if** Airy stress function: **then**
  - 7:    $Loss_p = \sum_{i=1}^n [l(\partial^2 NN_p(\mathbf{x}_i)/\partial y^2) - m(\partial^2 NN_p(\mathbf{x}_i)/\partial x \partial y) - \bar{t}_{xi}]^2 + \sum_{i=1}^n [-l(\partial^2 NN_p(\mathbf{x}_i)/\partial x \partial y) + m(\partial^2 NN_p(\mathbf{x}_i)/\partial x^2) - \bar{t}_{yi}]^2$ .
  - 8:   Minimize  $Loss_p$  to get the optimal parameters  $\theta_p$  of  $NN_p$ .
  - 9: **end if**
  - 10: **Step 2:** Training the basis net  $NN_b$ .
  - 11: Allocate training points  $\{\mathbf{x}_i \in \Gamma^t, d_i\}_{i=1}^m$  on the domain and boundary, where  $d_i$  is the nearest distance from  $\mathbf{x}_i$  to the force boundary conditions.
  - 12: **if** Prandtl stress function: **then**
  - 13:    $Loss_b = \sum_{i=1}^m [NN_b(\mathbf{x}_i) - d_i]^2$ .
  - 14: **end if**
  - 15: **if** Airy stress function: **then**
  - 16:    $Loss_b = \sum_{i=1}^m [NN_b(\mathbf{x}_i) - d_i]^2 + \sum_{i=1}^r [NN_b(\mathbf{x}_i)]^2 + \sum_{i=1}^r [\partial NN_b(\mathbf{x}_i)/\mathbf{n}]^2$ , where  $r$  is the number of points on the force boundary condition and  $\mathbf{n}$  is the normal direction of the force boundary.
  - 17: **end if**
  - 18: Minimize  $Loss_b$  to get the optimal parameters  $\theta_b$  of  $NN_b$ .
  - 19: **Step 3:** Select the terms of biharmonic function  $\phi_{bh}$  in Airy stress function.
  - 20: **Step 4:** Training the general net  $NN_g$ .
  - 21:  $\phi(\mathbf{x}) = NN_p(\mathbf{x}) + NN_g(\mathbf{x}; \theta_{NN_g}) * NN_b(\mathbf{x}) + \sum_{i=1}^s a_i * \phi_{bh}^i$ .
  - 22: Minimize the complementary energy and get the optimal parameters of  $\theta_{NN_g}$  and  $a_i$  (freeze the  $NN_p$  and  $NN_b$ ).
- 

### 3.4 | DCEM-O: Deep operator energy method based on the principle of minimum complementary energy

This idea's starting point is to reuse the existing calculation results fully and not waste the previous calculation results to improve the computational efficiency of DCEM. The idea of DCEM-O is to use the DeepONet framework to help DCEM make operator learning (DeepONet serves as the framework for our operator learning), as mentioned in Section 2.2. Trunk

net can build partial differential operators to construct the physical loss. The algorithmic flow of DCEM-O is shown in Algorithm 2

---

**Algorithm 2** The algorithm of DCEM-O
 

---

- 1: **Training:**
  - 2: **Data:** The high-fidelity stress function  $\{\mathbf{x}_s^j, \phi_s^j\}_{s=1}^n$  and variable field  $\{\mathbf{x}_i^j, f_i^j\}_{i=1}^m$  such as geometry, material information as the input of the branch net and  $j = 1, 2, \dots, t$ .
  - 3: **Step 1:** Training the branch  $NN_{br}$  and trunk net  $NN_t$ .
  - 4: input the variable field  $\{\mathbf{x}_i^j, f_i^j\}_{i=1}^m$  to the branch net; input the  $\mathbf{x}_s^j$  to the trunk net and  $\phi_s^j$  to the output stress function.
  - 5: Minimize the operation loss.
  - 6: **Test:**
  - 7: **Step 2:** Training the particular net  $NN_p$  as DCEM.
  - 8: **Step 3:** Training the basis net  $NN_b$  as DCEM.
  - 9: **Step 4:** Training the branch  $NN_{br}$  and trunk net  $NN_t$  again by minimizing the complementary energy to obtain the optimal parameters  $\theta_{br}$  and  $\theta_t$  (freeze the particular and basis net).
- 

Fig. 4 shows the framework of DCEM-O. We first construct the particular solution and basis function network at the force boundary condition, which is the same as the steps of DCEM. We only change the general network to the network structure of DeepONet. The training process is employed in a serial fashion; the training method is first to learn the operator in the existing data, i.e., not to construct the physical-based complementary energy functional first. After training based on the existing data, we consider optimization based on the principle of complementary energy based on physical laws. The input of our data in branch net here can be different geometric shapes, materials, and force boundary conditions (other field variables related to the problem can also be inputted to branch net), and the output is the existing high-fidelity stress function result, such as the stress-function element method. Finally, we optimize the parameters of the trunk and branch net based on the principle of minimum complementary energy.

The key of the operator learning with physical law lies in effectively integrating the principles of physics with data-driven approaches. Various methods have been proposed to bridge the gap between physical laws and data-driven techniques<sup>42,82,62</sup>. The AD and numerical differentiation can be used to construct the physical loss. In our study, we opt for the AD algorithm to create the physical loss. This choice is attributed to the fact that finite difference methods (numerical differentiation) necessitate a fine-resolution uniform grid. In the absence of such conditions, numerical errors in derivatives can become magnified in the output solution. As a result, the AD algorithm is preferred for constructing the physical loss. The hybrid optimization<sup>42,82,62</sup>, involves combining data loss and physical loss into a single loss function for optimization, using different hyperparameters. Specifically, the hybrid optimization strategy can be expressed as:

$$\begin{cases} \mathcal{L}(\theta) = \mathcal{L}_{data}(\theta) + \lambda * \mathcal{L}_{phy}(\theta) \\ \mathcal{L}_{data}(\theta) = \frac{1}{I*J} \sum_{j=1}^J \sum_{i=1}^I |NN_O(\mathbf{y}^{(i)}, \mathbf{u}^{(j)}; \theta) - \mathbf{u}^{(j)}(\mathbf{y}^{(i)})|^2 \\ \mathcal{L}_{phy}(\theta) = \frac{1}{I*J} \sum_{j=1}^J \sum_{k=1}^K |Phy(NN_O(\mathbf{x}^{(k)}, \mathbf{u}^{(j)}; \theta))|^2 \end{cases}, \quad (43)$$

where the details of Eq. (43) are elaborated in Section 2.2. This approach combines data loss (operator loss) and physical loss with different hyperparameters into the same loss function for optimization together. However, in our research, we have chosen a sequential optimization strategy instead of hybrid optimization. This choice is due to the challenge of selecting appropriate hyperparameters. We first optimize the data loss and subsequently optimize the physical loss.



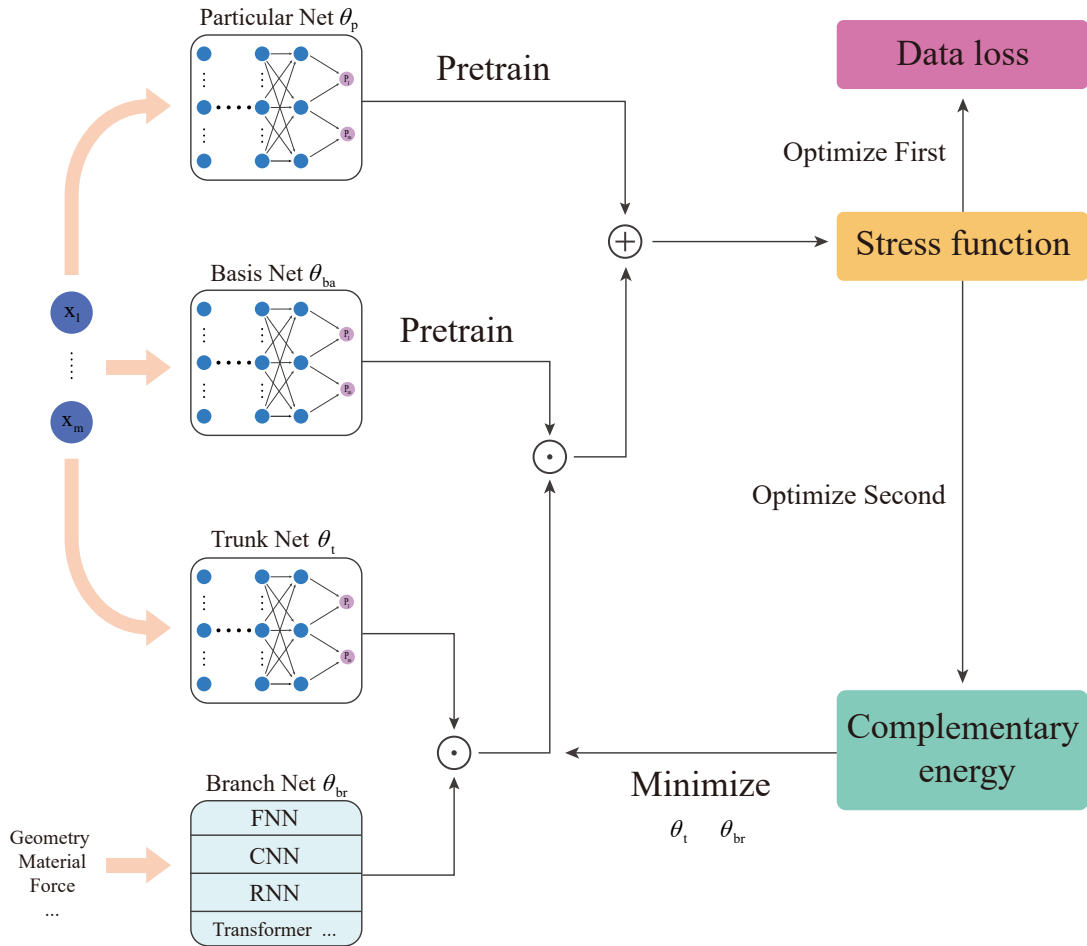


**FIGURE 4** The schematic of deep operator energy method based on the principle of minimum complementary energy (DCEM-O)

## 4 | RESULT

In this section, we introduce several benchmark problems to assess the robustness and effectiveness of the DCEM. Therefore, we will compare the solutions obtained using DCEM with those from DCM and DEM, using the reference solution from FEM as a basis for comparison when analytical solutions are not available. We will start by examining the Airy stress function, followed by the Prandtl stress function. The reference solution will be obtained using the Finite Element Method (FEM). Although the geometry and boundary conditions may not be complex, the FEM solution is considered to represent an accurate approximation of the exact solution.

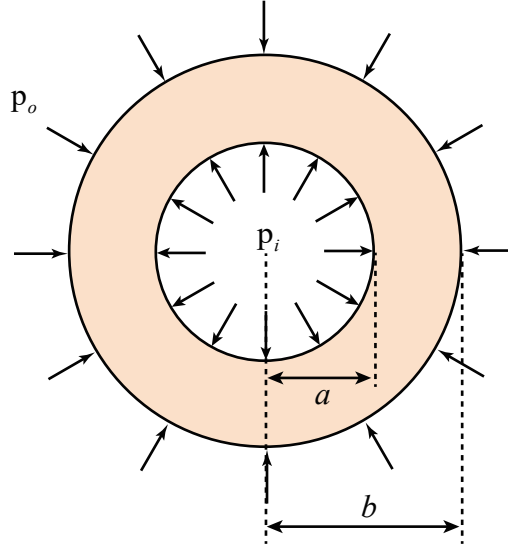


**FIGURE 5** Schematic diagram of the circular tube: the value of parameters are  $p_o = 10$ ,  $p_i = 5$ ,  $a = 0.5$ ,  $b = 1.0$ , Young's modulus  $E = 1000$ , and Poisson ratio  $\nu = 0.3$

## 4.1 | Airy stress function

### 4.1.1 | Circular tube: full displacement boundary conditions

The circular tube is of interest to the question of the thick pressure vessel, which is the common container for gas and storage in engineering<sup>83</sup>.

In the Section 4.2, all the boundary conditions are force boundary conditions. If we use DEM, the admissible displacement is not required. In this example, all the boundary conditions are displacement boundary conditions. As a result, the admissible stress function is not required in DCEM. The DEM can also be used to solve the full displacement boundary problem, but we have to require strong assumptions about admissible displacement fields.

As is shown in Fig. 5, we utilize Eq. (44) to convert the full pressure boundary conditions to the full displacement boundary conditions. The transformation enables a comparison of DEM and DCEM performance, highlighting varied advantages and disadvantages associated with different energy principles under full displacement boundary conditions. The DCEM does not need to assume the admissible stress function because there are no force boundary conditions. We use the displacement solution of the famous Lamé formula to construct the displacement boundary condition. The analytical solution of the Lamé stress and displacement is:

$$\begin{aligned}
 \sigma_r &= \frac{a^2}{b^2 - a^2} \left(1 - \frac{b^2}{r^2}\right) p_i - \frac{b^2}{b^2 - a^2} \left(1 - \frac{a^2}{r^2}\right) p_o \\
 \sigma_\theta &= \frac{a^2}{b^2 - a^2} \left(1 + \frac{b^2}{r^2}\right) p_i - \frac{b^2}{b^2 - a^2} \left(1 + \frac{a^2}{r^2}\right) p_o \\
 u_r &= \frac{1}{E} \left[ \frac{(1 - \nu)(a^2 p_i - b^2 p_o)}{b^2 - a^2} r + \frac{(1 + \nu)a^2 b^2 (p_i - p_o)}{b^2 - a^2} \frac{1}{r} \right] \\
 v_\theta &= 0,
 \end{aligned} \tag{44}$$

where  $a$  and  $b$  are inner and outer radius respectively,  $E$  and  $\nu$  are Young's modulus and Poisson's ratio,  $p_i$  and  $p_o$  are the uniform pressure at  $r = a$  and  $r = b$ . The compressive stress is positive.

To use the DCEM to solve the problem, we need to express the complementary strain energy and complementary potential in the form of stress function. The stress expressed by the stress function of the axisymmetric problem in polar

coordinates is:

$$\begin{aligned}\sigma_r &= \frac{1}{r} \frac{\partial \phi}{\partial r} \\ \sigma_\theta &= \frac{\partial^2 \phi}{\partial r^2}.\end{aligned}\quad (45)$$

According to the constitutive law, the strain in polar coordinates is:

$$\begin{aligned}\varepsilon_r &= \frac{1}{E}(\sigma_r - \nu \sigma_\theta) = \frac{1}{E} \left( \frac{1}{r} \frac{\partial \phi}{\partial r} - \nu \frac{\partial^2 \phi}{\partial r^2} \right) \\ \varepsilon_\theta &= \frac{1}{E}(\sigma_\theta - \nu \sigma_r) = \frac{1}{E} \left( \frac{\partial^2 \phi}{\partial r^2} - \nu \frac{1}{r} \frac{\partial \phi}{\partial r} \right)\end{aligned}\quad (46)$$

The complementary strain energy is expressed as a stress function:

$$\begin{aligned}W_c &= \int_{\Omega} \frac{1}{2} \sigma_{ij} \varepsilon_{ij} d\Omega = \int_{\Omega} \frac{1}{2} (\sigma_r \varepsilon_r + \sigma_\theta \varepsilon_\theta) 2\pi r dr \\ &= \int_{\Omega} \frac{1}{2} \left[ \frac{1}{r} \frac{\partial \phi}{\partial r} \frac{1}{E} \left( \frac{1}{r} \frac{\partial \phi}{\partial r} - \nu \frac{\partial^2 \phi}{\partial r^2} \right) + \frac{\partial^2 \phi}{\partial r^2} \frac{1}{E} \left( \frac{\partial^2 \phi}{\partial r^2} - \nu \frac{1}{r} \frac{\partial \phi}{\partial r} \right) \right] 2\pi r dr\end{aligned}\quad (47)$$

The complementary potential is:

$$\begin{aligned}V_c &= u_r \sigma_r 2\pi r |_{r=b} - u_r \sigma_r 2\pi r |_{r=a} \\ &= u_r \frac{\partial \phi}{\partial r} 2\pi |_{r=b} - u_r \frac{\partial \phi}{\partial r} 2\pi |_{r=a}\end{aligned}\quad (48)$$

In order to research the accuracy of DCEM, the analytical solution is brought into the complementary strain energy  $W_c = 79\pi/960$  and complementary potential  $V_c = 79\pi/480$  ( $p_o = 10$ ,  $p_i = 5$ ,  $a = 0.5$ ,  $b = 1.0$ , Young's modulus  $E = 1000$ , and Poisson ratio  $\nu = 0.3$ ). Fig. 6 shows the stress prediction of DCEM compared with the analytical solution. The points are uniformly distributed. This problem is axisymmetric so the problem can be reduced to a one-dimensional problem. Thus, the number of the input and output neurons are both 1 (the input is  $r$ , the output is Airy stress function), 3 hidden layers, each layer 20 neurons, optimization function Adam, 2000 iterations. The absolute error of  $\sigma_r$  is smaller than  $\sigma_\theta$ , the primary error of  $\sigma_r$  is on the inner ring boundary, the primary error of  $\sigma_\theta$  is on inner and outer ring boundary. Fig. 7 shows the comparison between the stress and the analytical solution in the radial direction. The  $\mathcal{L}_2^{rel}$  errors of  $\sigma_r$ ,  $\sigma_\theta$  and  $u_r$  are  $\sim 10^{-5}$ ,  $\sim 10^{-4}$ , and  $\sim 10^{-3}$  respectively. The error of  $\sigma_r$  is smaller than  $\sigma_\theta$ , mainly because  $\sigma_r$  is the first derivative of the stress function, but  $\sigma_\theta$  is the second derivative of the stress function. With increasing derivative order, the error in general tends to become larger. More importantly, the stress is more accurate than displacement. In FEM, FEM based on stress is also more accurate than FEM based on displacement in term of stress, which is consistent with the conclusion of the comparison between DEM and DCEM. We also compute the  $\mathcal{H}_1^{rel}$  and  $\mathcal{L}_2^{rel}$  in different number of domain points and neural network in Fig. 7d,e. The  $\mathcal{L}_2^{rel}$  relative error norm and  $\mathcal{H}_1^{rel}$  relative error seminorm in DCEM are calculated as follows

$$\begin{aligned}\|e\|_{\mathcal{L}_2^{rel}} &= \frac{\|\phi^{pred} - \phi^{exact}\|_{\mathcal{L}_2}}{\|\phi^{exact}\|_{\mathcal{L}_2}} = \frac{\int_{\Omega} (\phi^{pred} - \phi^{exact})^2 dr}{\int_{\Omega} (\phi^{exact})^2 dr} \\ \|e\|_{\mathcal{H}_1^{rel}} &= \frac{\|\phi^{pred} - \phi^{exact}\|_{\mathcal{H}_1}}{\|\phi^{exact}\|_{\mathcal{H}_1}} = \frac{\int_{\Omega} (E^{pred} - E^{exact})^2 dr}{\int_{\Omega} (E^{exact})^2 dr} \\ E &= \int_{\Omega} \left( \frac{\partial \phi}{\partial r} \right)^2 dr.\end{aligned}\quad (49)$$

The results show all neural network architectures exhibit promising results compared to the exact solution. However, it's important to note that all methods don't exhibit convergence concerning the number of hidden layers, i.e., adding more hidden layers doesn't consistently lead to improved accuracy. Besides, since all boundaries are displacement boundaries, the admissible stress function does not need to be constructed in advance.

Considering the strong form of the stress function:

$$\nabla^4 \phi = 0. \quad (50)$$

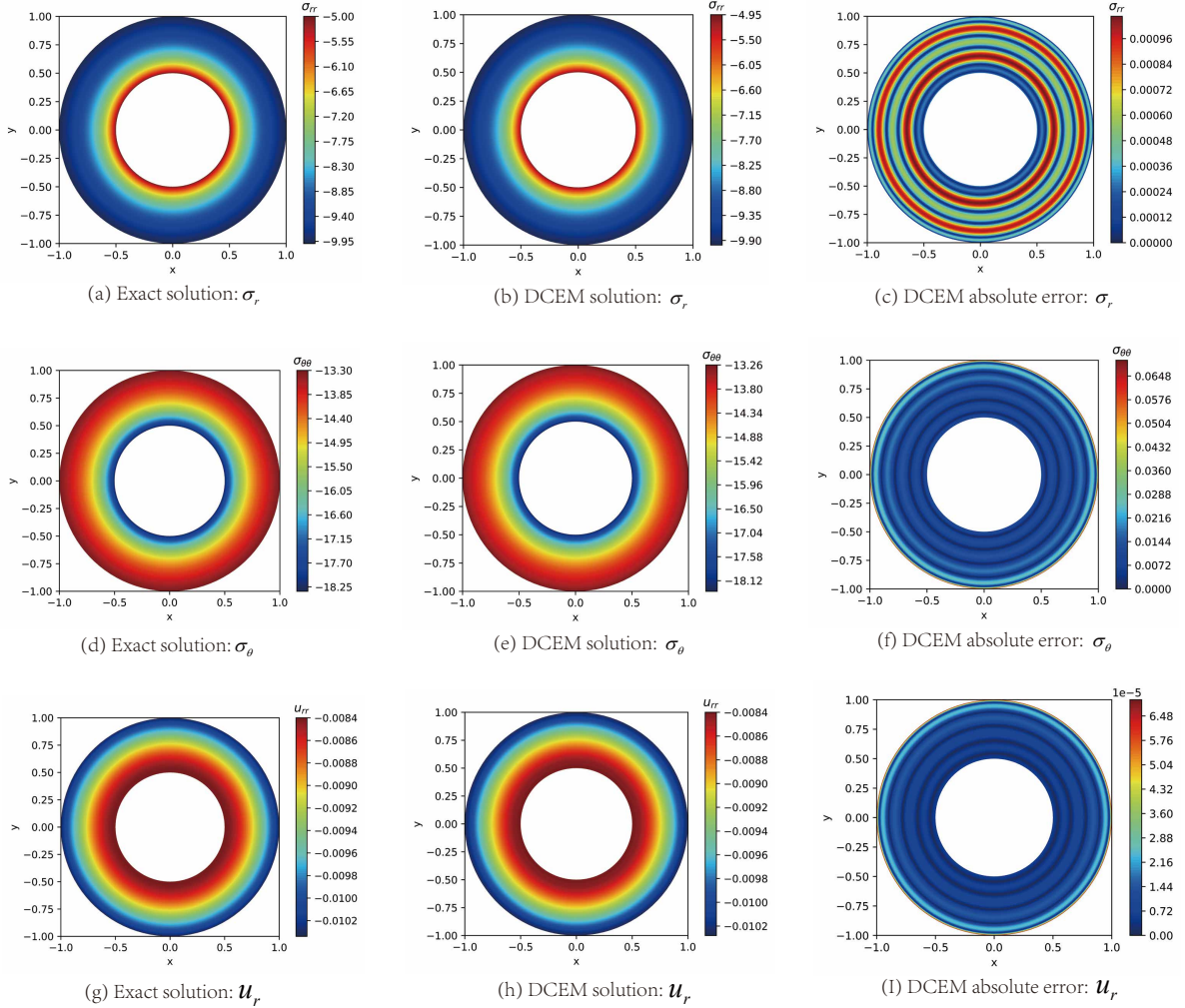


**FIGURE 6** The result of stress  $\sigma_r$ ,  $\sigma_\theta$  and  $u_r$  of the circular tube by DCEM: the exact solution of  $\sigma_r$  (a),  $\sigma_\theta$  (d) and  $u_r$  (g); the prediction of DCEM in  $\sigma_r$  (b),  $\sigma_\theta$  (e) and  $u_r$  (h); the absolute error of DCEM in  $\sigma_r$  (c),  $\sigma_\theta$  (f) and  $u_r$  (i).

Adding some basis functions that naturally satisfy the biharmonic equation as shown in Eq. (50) will improve the accuracy and convergence speed of DCEM. Thus, DCEM-P is proposed by adding some basis functions to the DCEM model. Take the circular tube as an example, and the biharmonic equation for the axisymmetric problem is simplified as follows:

$$\frac{d^4\phi}{dr^4} + \frac{2}{r} \frac{d^3\phi}{dr^3} - \frac{1}{r^2} \frac{d^2\phi}{dr^2} + \frac{1}{r^3} \frac{d\phi}{dr} = 0. \quad (51)$$

The biharmonic function satisfying this equation is  $\ln(r)$ ,  $r^2$  and  $r^2\ln(r)$ . The stress of these biharmonic function are shown in Table 2, and we add the biharmonic function to the stress function field:

$$\phi = NN(r; \theta) + a_1\ln(r) + a_2r^2 + a_3r^2\ln(r), \quad (52)$$

where  $a_1$ ,  $a_2$  and  $a_3$  are set as optimization variables for optimization. Fig. 8 compares the stress  $L_2$  error with the biharmonic function, i.e., adding  $\ln(r)$ ,  $r^2$ ,  $r^2\ln(r)$  separately and all biharmonic functions. After adding the biharmonic function, the stress accuracy has been improved to a certain extent, and the convergence speed has been accelerated at the same time. The improved effect of the biharmonic function  $\ln(r)$  is the most obvious because the analytical solution contains the  $1/r^2$  item. Thus it is equivalent to naturally constructing the stress function item that satisfies the analytical solution,

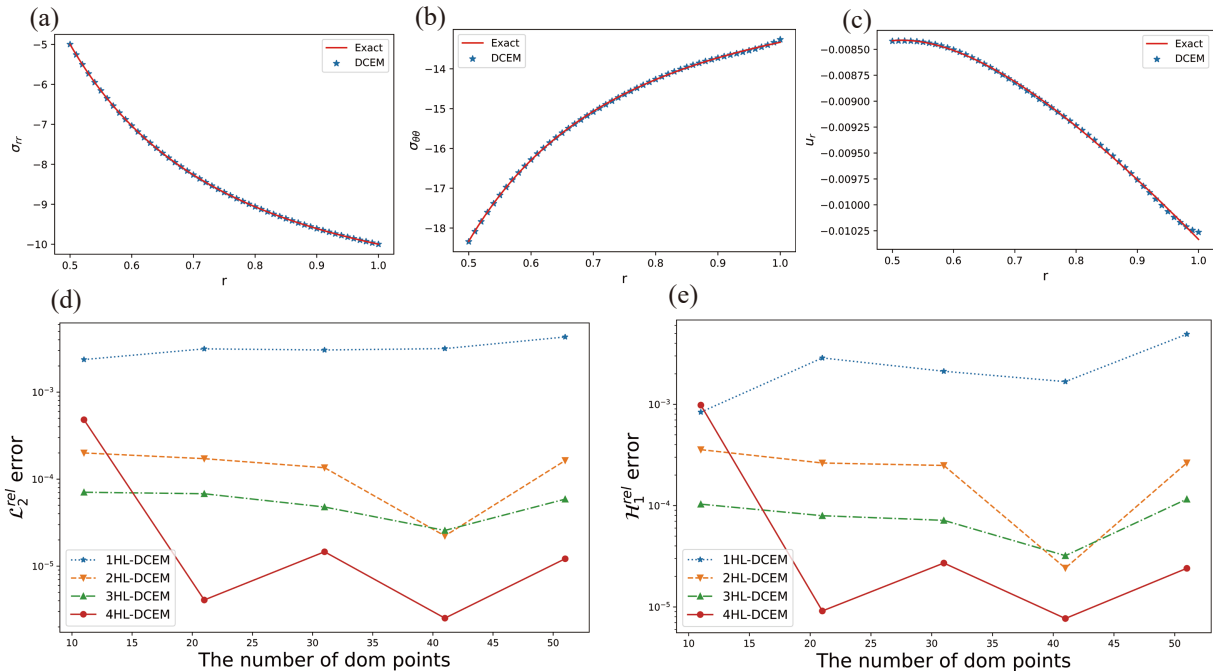


**FIGURE 7** The stress  $\sigma_r$  (a),  $\sigma_\theta$  (b) and  $u_r$  (c) of the circular tube in the radial direction under prediction solution of the DCEM compared with analytical solution. The error in terms of  $\mathcal{L}_2^{rel}$  norm (d) and  $\mathcal{H}_1^{rel}$  seminorm (e) of DCEM with respect to the training steps in Airy stress function. Four different neural networks were constructed, each having a different number of hidden layers (HL): 1HL, 2HL, 3HL, and 4HL. Each hidden layer consists of 30 neurons. The number of domain points are the number of uniformly distributed points in the radius.

**TABLE 2** The stress fields (polar coordinates) are obtained by the Airy stress function satisfying the biharmonic function.

Biharmonic function	$\ln(r)$	$r^2$	$r^2 \ln(r)$
$\sigma_r$	$1/r^2$	2	$1 + 2\ln(r)$
$\sigma_\theta$	$-1/r^2$	2	$3 + 2\ln(r)$
$\tau_{r\theta}$	0	0	0

and the accuracy and convergence speed is naturally fast. In addition, all biharmonic are added, and the accuracy and convergence speed is almost the same as just adding  $\ln(r)$ , which shows that DCEM-P can well adjust the best biharmonic terms adaptively, making it prominent  $\ln(r)$ . After adding the biharmonic function, there will be a sudden change in a certain iteration step, which is caused by a dynamic game between the neural network approximation and the trainable coefficient of the biharmonic function. The gradient of the coefficient of the biharmonic function is larger than that of trainable parameters of the neural network. As a result, we adjust the learning rate of different parameters according to gradient. To be specific,

$$lr_{bh} = lr_{nn} * \frac{\text{mean}\{|\nabla_{nn}Loss|\}}{\text{mean}\{|\nabla_{bh}Loss|\}}, \quad (53)$$

where  $lr_{bh}$  is the learning rate of coefficient of biharmonic function, and  $lr_{nn}$  is the learning rate of the trainable parameters of neural network.  $\nabla_{nn}Loss$  means the gradient of the trainable parameters including weight but without bias of neural network.  $\nabla_{bh}Loss$  means the gradient of the coefficient of biharmonic function.

Next, we compare the accuracy and efficiency of the DEM, the PINNs displacement strong form (LN equation), and the DCEM (without adding the biharmonic function) under full displacement boundary conditions, the strong form of the PINNs stress function is not compared since the strong form of the stress function is inconvenient to deal with the

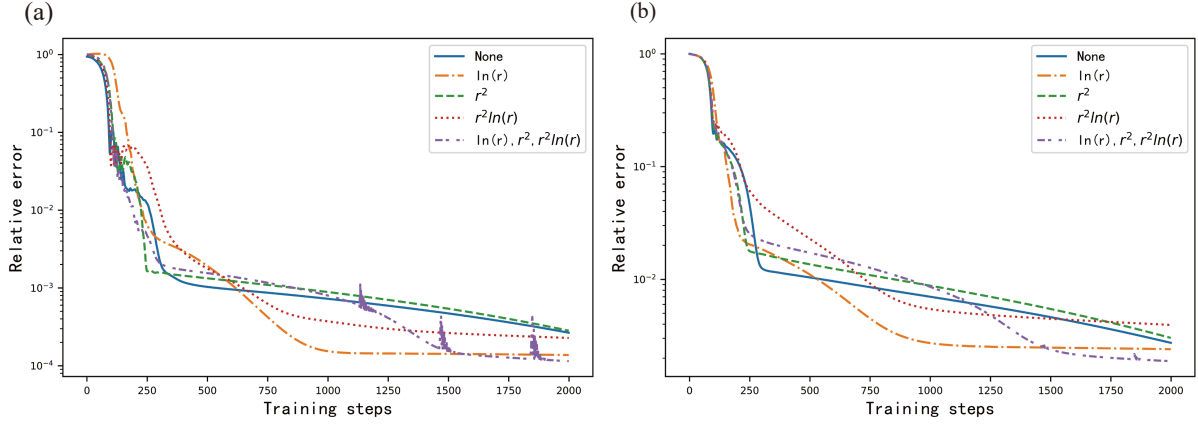


**FIGURE 8** The overall relative  $\mathcal{L}_2$  errors of stress  $\sigma_r$  (a) and  $\sigma_\theta$  (b) in different biharmonic functions of the circular tube under the DCEM-P.

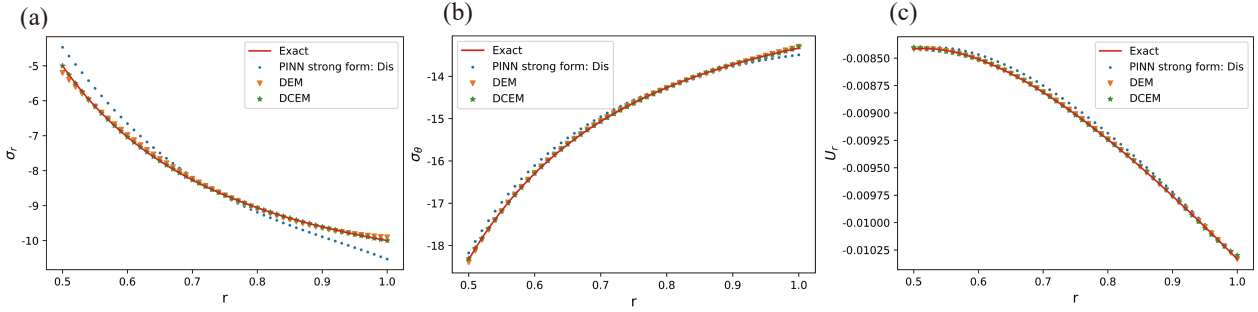


**FIGURE 9** Comparison of the predicted stress  $\sigma_r$  (a),  $\sigma_\theta$  (b) and  $u_r$  (c) with the analytical solution of the circular tube under the strong form of PINNs displacement, DEM, and DCEM in the radial direction

displacement boundary conditions because it needs to be given in the form of boundary integrals. Thus, the strong form of the stress function is not considered. The construction method of the admissible displacement field in DEM and the strong form of PINNs displacement is:

$$u = \left(1 - \frac{r}{a}\right) \frac{a}{a-b} u_r|_{r=b} + \left(1 - \frac{r}{b}\right) \frac{b}{b-a} u_r|_{r=a} + (r-a)(r-b) * NN(r; \theta). \quad (54)$$

It is not difficult to verify that the above admissible displacement field satisfies the given displacement boundary condition. The configurations of these three methods are the same (10,000 points in the radial direction, optimizer Adam, 3 hidden layers of neural network, 20 neurons in each layer). Since the strong form of PINNs displacement involves the second-order derivative, the computation time is larger than that of the DEM with only the first-order derivative. In addition, the DCEM and DEM also involves the numerical integrals. As a result, the calculation of DCEM is required for precise numerical integration. In terms of the stress, Fig. 9 and Fig. 10 show that DCEM is the closest to the analytical solution, and the precision is the highest, while DEM have the most accurate in term of displacement. The precision of the DCEM is the highest because there is no assumption on the form of the stress function, and DCEM completely releases the strong fitness ability of the neural network. However, the DEM and the PINNs displacement strong form are optimized under a certain displacement assumption space, and the optimization space is not as large as the DCEM. Thus, the approximation error of DEM is greater than the DCEM in term of stress. Because DCEM is based on stress directly and DEM is base on displacement directly, the accuracy of displacement obtained by DEM is higher than DCEM. The phenomenon is similar to FEM based on displacement or stress. In sum, for the problem of dealing with full-displacement boundary conditions, the DCEM is theoretically more suitable than the DEM and the PINNs displacement strong form in term of stress.

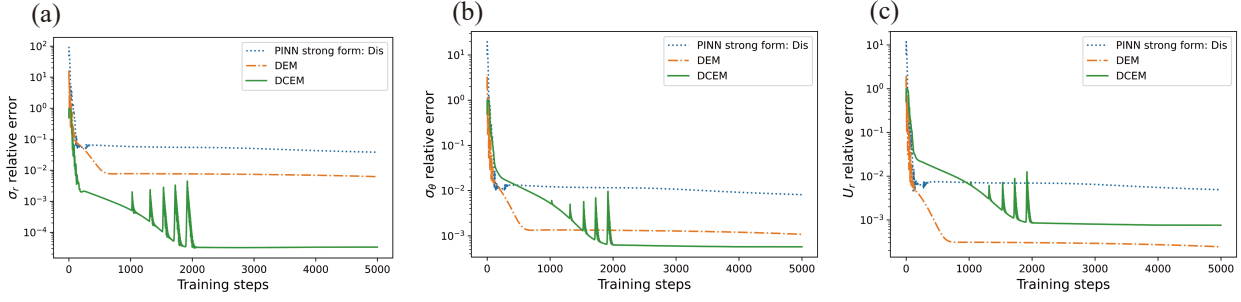


**FIGURE 10** Relative error  $\mathcal{L}_2$  of the stress  $\sigma_r$  (a),  $\sigma_\theta$  (b) and  $u_r$  (c) of the circular tube under the strong form of PINNs displacement, DEM and DCEM

We compare the DCEM-O (operator learning based on DCEM) with DCEM in this full-displacement boundary example. The input of the branch net is pressure,  $p_i$  and  $p_o$ . Because the problem does not have the force boundary condition, the basis and particular solution are not required. The output of the DCEM-O can be written as:

$$\phi = NN_B(p_i, p_o; \theta) * NN_T(r; \theta). \quad (55)$$

The architecture of the trunk net is 6 hidden layers and 30 neurons in every hidden layer. The architecture of the branch net is 3 hidden layers and 30 neurons in every hidden layer. We use 10000 different  $p_i$ ,  $p_o$  (Boundary conditions), Poisson's ratio (Material property), and  $b$  (Geometry) as the input of the branch net. The input of trunk net is all 10 equal spacing points:  $p_i$  from 4.0 to 6.0,  $p_o$  from 9.0 to 11.0, Poisson's ratio from 0.3 to 0.49 and  $b$  from 0.9 to 1.1, respectively. Every input of  $p_i$ ,  $p_o$ , Poisson's ratio, and  $b$  is divided into all 10 equal spacing points, resulting in a total of  $10 \times 10 \times 10 = 10,000$  data points. The output of DCEM-O is the Airy stress function  $\phi$ , and the output training dataset is from the analytical solution of the problem or the high fidelity numerical experiment (FEM based on the stress function element<sup>84</sup>). The analytical solution of the circular tube can be written as:

$$\phi = \frac{a^2}{b^2 - a^2} \left[ \frac{r^2}{2} - b^2 \ln(r) \right] p_i - \frac{b^2}{b^2 - a^2} \left[ \frac{r^2}{2} - a^2 \ln(r) \right] p_o. \quad (56)$$

Note that the test dataset (we test  $p_i = 5$ ,  $p_o = 10$ , Poisson's ratio 0.5, and  $b = 1.0$ ) is out of the training set. The test is interesting because the Poisson's ratio is incompressible and the extrapolation capability of DCEM-O can be tested. Fig. 11 shows the comparison of DCEM with DCEM-O, and the absolute error of DCEM-O is lower than DCEM in the same iteration. Fig. 11s,t,u shows the DCEM-O can converge faster than the DCEM in the initial iteration step, and both can converge to the exact solution at the 5000 iteration.

#### 4.1.2 | Wedge: infinite problem

The wedge problem is a common problem in engineering, and it can be encountered in various scenarios such as the curling up of the sharp leading edge of a supersonic wing<sup>85</sup>. In elasticity mechanics, the stress function method is commonly used to solve this problem<sup>79</sup>. In this problem, a normal pressure distribution  $p = qr^m$  acts on the wedge, as depicted in Fig. 12a.

The Airy stress function for this problem can be expressed analytically as follows:

$$\phi = r^{m+2} \{ a * \cos[(m+2)\theta] + b * \sin[(m+2)\theta] + c * \cos(m\theta) + d * \sin(m\theta) \}, \quad (57)$$

where the constants  $a$ ,  $b$ ,  $c$ , and  $d$  are determined by the shape and load of the boundary. For the specific case of  $m = 0$  and  $\alpha = \pi$ , which corresponds to a semi-infinite uniform pressure on the upper boundary of an elastic medium of infinite extent, the Airy stress function simplifies to:

$$\phi = cr^2 [\alpha - \theta + \sin(\theta)\cos(\theta) - \cos^2(\theta)\tan(\alpha)], \quad (58)$$

where  $c = q/[2(\tan(\alpha) - \alpha)]$ ,  $\alpha = \pi$ ,  $q = 5$ ,  $E = 1000$ , and  $\mu = 0.3$ , as shown in Fig. 12b.

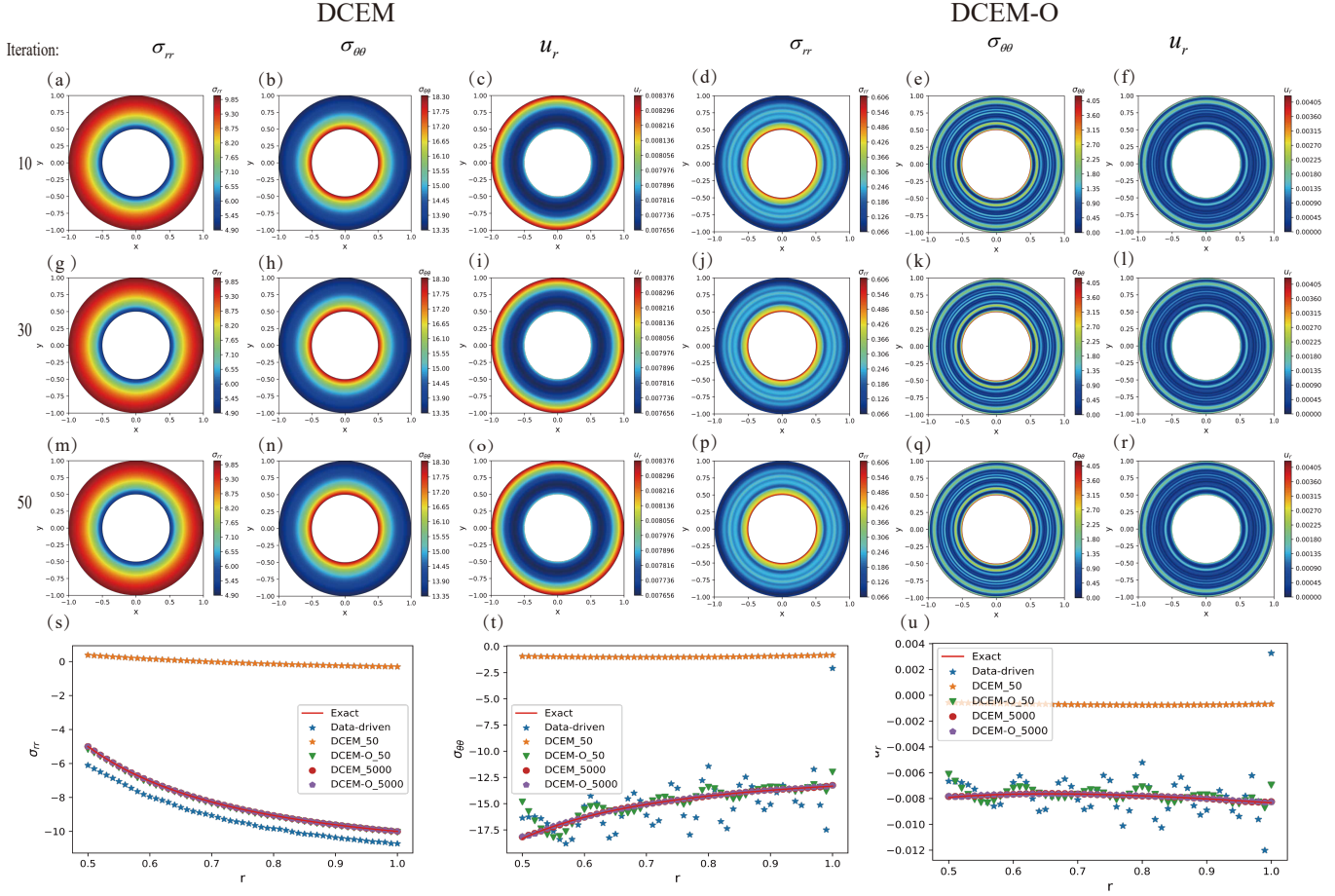


**FIGURE 11** Comparison of DCEM and DCEM-O in Airy stress function of circular tube: (a, b, c, d, e, f), (g, h, i, j, k, l), and (m, n, o, p, q, r) the absolute error in the number of iterations 10, 30, and 50 respectively; (a, g, m, d, j, p)  $\sigma_{rr}$ ; (b, h, n, e, k, q)  $\sigma_{\theta\theta}$ ; (c, i, o, f, l, r)  $u_r$ ; (a, b, c, g, h, i, m, n, o) the result of DCEM; (d, e, f, j, k, l, p, q, r) the result of DCEM-O; (s) the prediction of  $\sigma_{rr}$  by DCEM and DCEM-O of initial 50 and converged 5000 iterations; (t) the prediction of  $\sigma_{\theta\theta}$  by DCEM and DCEM-O of initial 50 and converged 5000 iterations; (u) the prediction of  $u_r$  by DCEM and DCEM-O of initial 50 and converged 5000 iterations. Data-driven means DCEM-O predict the stress without fine-tuning by the physical laws.

Using the stress formulas based on polar coordinates, we can obtain the analytical solutions for stress components:

$$\begin{aligned}
 \sigma_r &= \frac{1}{r^2} \frac{\partial^2 \phi}{\partial \theta^2} + \frac{1}{r} \frac{\partial \phi}{\partial r} = 2c[\alpha - \theta - \sin^2(\theta)\tan(\alpha) - \sin(\theta)\cos(\theta)] \\
 \sigma_\theta &= \frac{\partial^2 \phi}{\partial r^2} = 2c[\alpha - \theta + \sin(\theta)\cos(\theta) - \cos^2(\theta)\tan(\alpha)] \\
 \tau_{r\theta} &= -\frac{\partial}{\partial r} \left( \frac{1}{r} \frac{\partial \phi}{\partial \theta} \right) = c[1 - \cos(2\theta) - \sin(2\theta)\tan(\alpha)].
 \end{aligned} \tag{59}$$

To verify the accuracy of the DCEM algorithm, we use the analytical solution and compare it with the PINNs strong form of the stress function as shown in Eq. (50). Due to the infinite characteristic of the problem, it is challenging to solve it using the displacement method, so we do not attempt to solve it using the DEM.

The key to DCEM lies in constructing the admissible stress function that satisfies both the boundary value condition and the derivative condition, which is different from the admissible displacement field. According to the properties of Airy



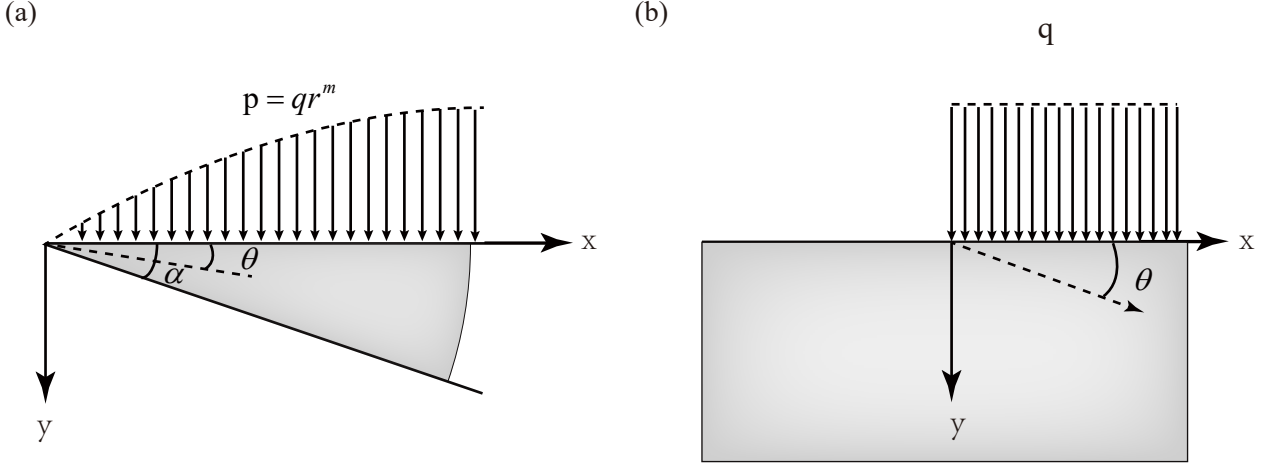


**FIGURE 12** (a) The schematic of the problem of the wedge. (b) Semi-infinite uniform pressure on the half-space infinite elastic medium.

stress function as explained in [Appendix B](#), the form of the stress function is:

$$\phi = r^2 f(\theta) \quad (60)$$

We can use the neural network to approximate  $f(\theta)$ . Since DCEM must satisfy the force boundary condition in advance before we use the principle of minimum complementary energy, the basis function method in [Table 1](#) is used to construct the admissible stress function to satisfy the requirement of the DCEM. The admissible stress function can be expressed as:

$$f_{NN}(\theta) = NN_p(\theta) + NN_b(\theta) * NN_g(\theta), \quad (61)$$

where particular network  $NN_p$  satisfy the boundary condition when on the natural boundary (cubic polynomial is used in  $NN_p$ ), i.e.,

$$\begin{cases} NN_p(0) = -\frac{1}{2}q \\ NN_p(\alpha) = 0 \\ NN_p'(0) = 0 \\ NN_p'(\alpha) = 0. \end{cases} \quad (62)$$

The basis network  $NN_b$  is constructed based on the distance function, and  $NN_b$  is expressed as follows:

$$NN_b(\theta) = \lambda * [\theta * (\alpha - \theta)]^2, \quad (63)$$

where  $\lambda = \alpha^4/16$  is used for normalization because the maximum of  $NN_b$  without  $\lambda$  is  $16/\alpha^4$  when  $NN_b(\alpha/2)$ .  $NN_g$  is generalized network, the trainable parameters of which is determined by the principle of the minimum complementary energy. It is easy to verify that the  $f_{NN}(\theta)$  satisfy the requirement of the admissible stress function, i.e.  $f_{NN}(0) = -1/(2q)$ ,  $f_{NN}(\alpha) = 0$ ,  $f'_{NN}(0) = 0$ ,  $f'_{NN}(\alpha) = 0$ .

To better quantify the overall error of the DCEM, we analyze the variation trend of its  $\mathcal{L}_2^{rel}$  error with the number of iterations. As shown in [Fig. 13a](#), the relative errors of  $\sigma_r$ ,  $\sigma_\theta$ ,  $\tau_{r\theta}$ , and  $u_r$  in DCEM are approximately  $\sim 10^{-3}$ ,  $\sim 10^{-5}$ ,  $\sim 10^{-4}$ , and  $\sim 10^{-5}$ , respectively. Compared with PINNs strong form of stress function as shown in [Fig. 13b](#), DCEM exhibits better accuracy and efficiency, especially in efficiency, as demonstrated in [Table 3](#). This improved efficiency is mainly attributed to DCEM's lower order derivatives, which result in higher computational efficiency. Additionally, the convergence speed of DCEM is significantly faster than that of PINNs strong form of stress function. The accuracy of  $\sigma_\theta$  is observed to be the highest among the other stress components. This is because of the relationship between the Airy stress function and stress, as shown in [Eq. \(59\)](#). The accuracy is inversely proportional to the order of the derivative. [Fig. 14](#)

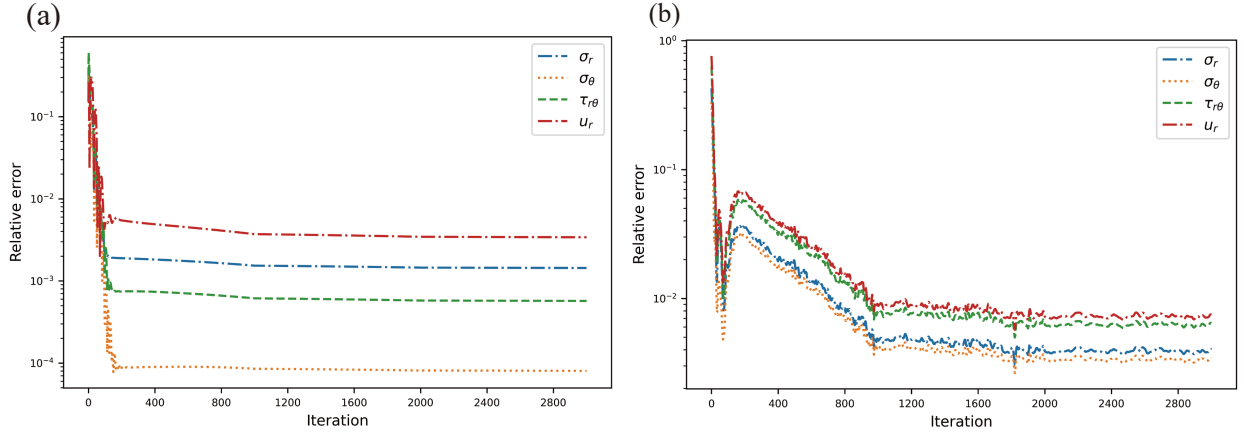


**FIGURE 13** The overall relative error  $\mathcal{L}_2$  of the wedge in  $\sigma_r, \sigma_\theta$ , and  $\tau_{r\theta}$  under DCEM (a) and PINNs strong form (b).

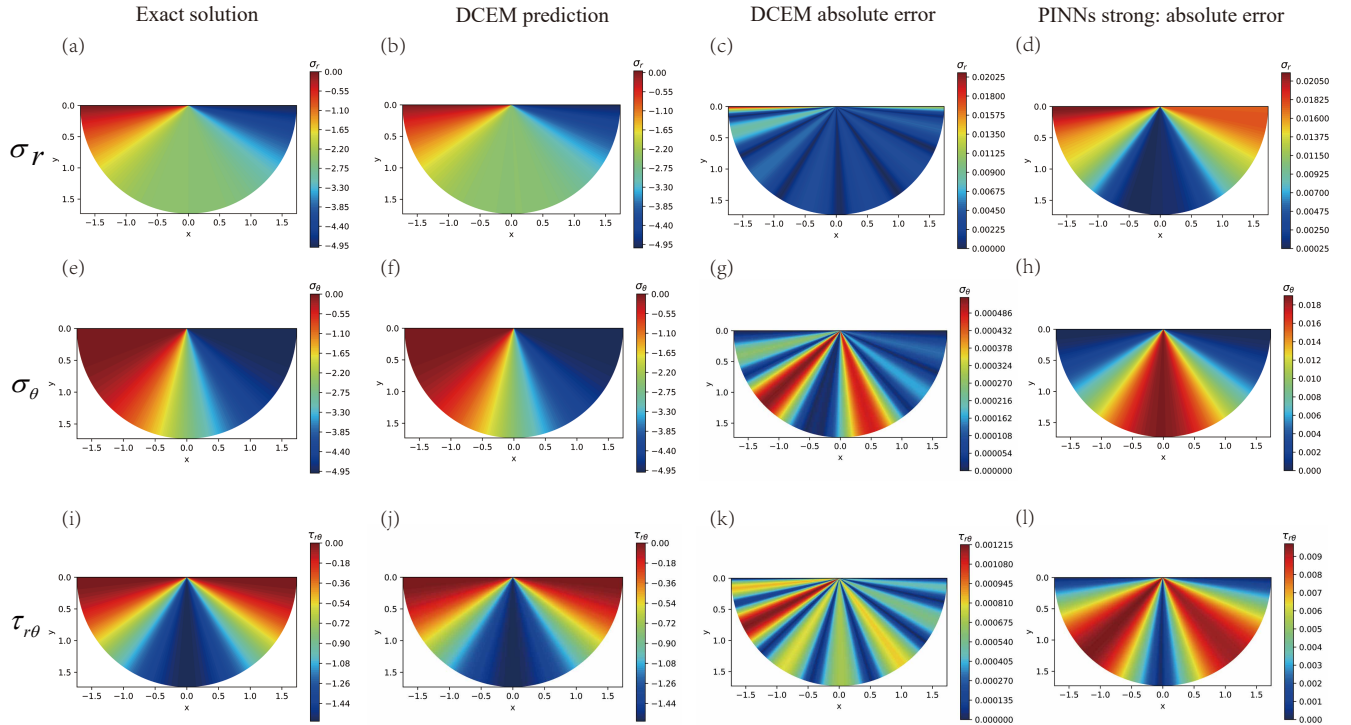


**FIGURE 14** Comparison of DCEM and PINNs strong form of stress function: (a, b, c, d)  $\sigma_r$ ; (e, f, g, h)  $\sigma_\theta$ ; (i, j, k, l)  $\tau_{r\theta}$ ; (a, e, i) exact solution; (b, f, j) DCEM prediction; (c, g, k) the absolute error of DCEM; (d, h, l) the absolute error of PINNs strong form of stress function.

further illustrates the performance of DCEM and PINNs strong form. The contour plots demonstrate that DCEM exhibits higher accuracy than PINNs in terms of the maximum absolute error and the distribution of the error, although both methods are actually quite accurate as shown in Fig. 15.

For further comparison, we analyze different angles  $\alpha$  as shown in Table 3. The results demonstrate that DCEM consistently exhibits better accuracy and efficiency compared to PINNs strong form of stress function across different angles of the wedge. This indicates that DCEM is a robust and reliable method for solving wedge problems with varying

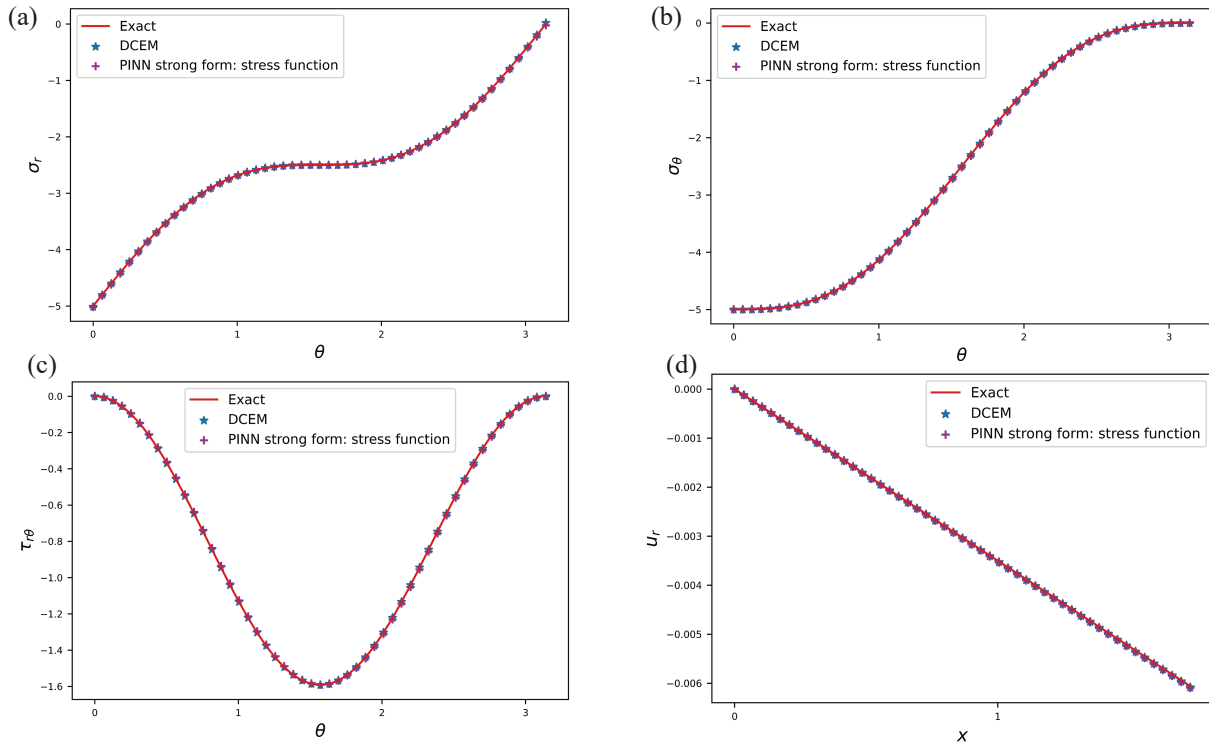


**FIGURE 15** Comparison of the stresses  $\sigma_r$  (a),  $\sigma_\theta$  (b),  $\tau_{r\theta}$  (c) and  $u_r$  (d) of the DCEM and PINNs stress functions of semi-infinite body subjected to a semi-infinite uniform load.

**TABLE 3** Accuracy and efficiency comparison of DCEM, DEM and strong form of stress function for wedge with uniform load

Relative error and converge time	DCEM				PINNs			
	$\alpha = \frac{\pi}{3}$	$\alpha = \frac{\pi}{4}$	$\alpha = \frac{\pi}{5}$	$\alpha = \pi$	$\alpha = \frac{\pi}{3}$	$\alpha = \frac{\pi}{4}$	$\alpha = \frac{\pi}{5}$	$\alpha = \pi$
$\sigma_r$	6.85e-04	7.35e-04	8.23e-04	1.43e-03	2.13e-03	8.71e-03	4.84e-03	4.38e-03
$\sigma_\theta$	1.92e-05	3.01e-05	3.72e-05	8.04e-05	2.98e-03	4.41e-03	4.67e-03	3.77e-03
$\tau_{r\theta}$	1.19e-04	1.59e-04	1.92e-04	5.70e-04	3.41e-03	2.77e-03	1.62e-03	7.03e-03
$u_r$	2.32e-03	2.04e-03	1.88e-3	3.40e-03	7.89e-03	7.07e-03	6.17e-3	8.18e-03
Time(s)	3.49	3.61	3.41	3.35	28.87	30.27	36.11	40.57

geometries. The improved accuracy and efficiency of DCEM make it a promising approach for practical engineering applications where accurate stress analysis is crucial.

We compared DCEM-O (operator learning based on DCEM) with DCEM in solving the wedge problem. In DCEM-O, the branch net takes the geometry information  $\alpha$  and external force  $q$  as input. The output of the DCEM-O can be written as:

$$\phi = r^2 * [NN_p(\theta) + NN_b(\theta) * Branch(\alpha, q; \theta) * Trunk(\theta; \theta)]. \quad (64)$$

The architecture of the trunk net is 6 hidden layers and 30 neurons in every hidden layer. The architecture of the branch net is 3 hidden layers and 30 neurons in every hidden layer. We use the 110 different  $\alpha$  and external force  $q$  as the input of the branch net. The input of the trunk net is 100 equal spacing points. The output of DCEM-O is the Airy stress function  $\phi$ , and the training dataset for DCEM-O is obtained from the analytical solution in Eq. (58), while the test dataset (with  $\alpha = \pi$  and  $q = 5$ ) is different from the training set. Fig. 16 illustrates the comparison of DCEM with DCEM-O. DCEM-O demonstrates significantly higher accuracy in a very small number of iterations, indicating that it converges much faster than DCEM in terms of stress results at the same iteration level. This suggests that the combination of data and physical law is a very efficient and promising approach for solving PDEs.

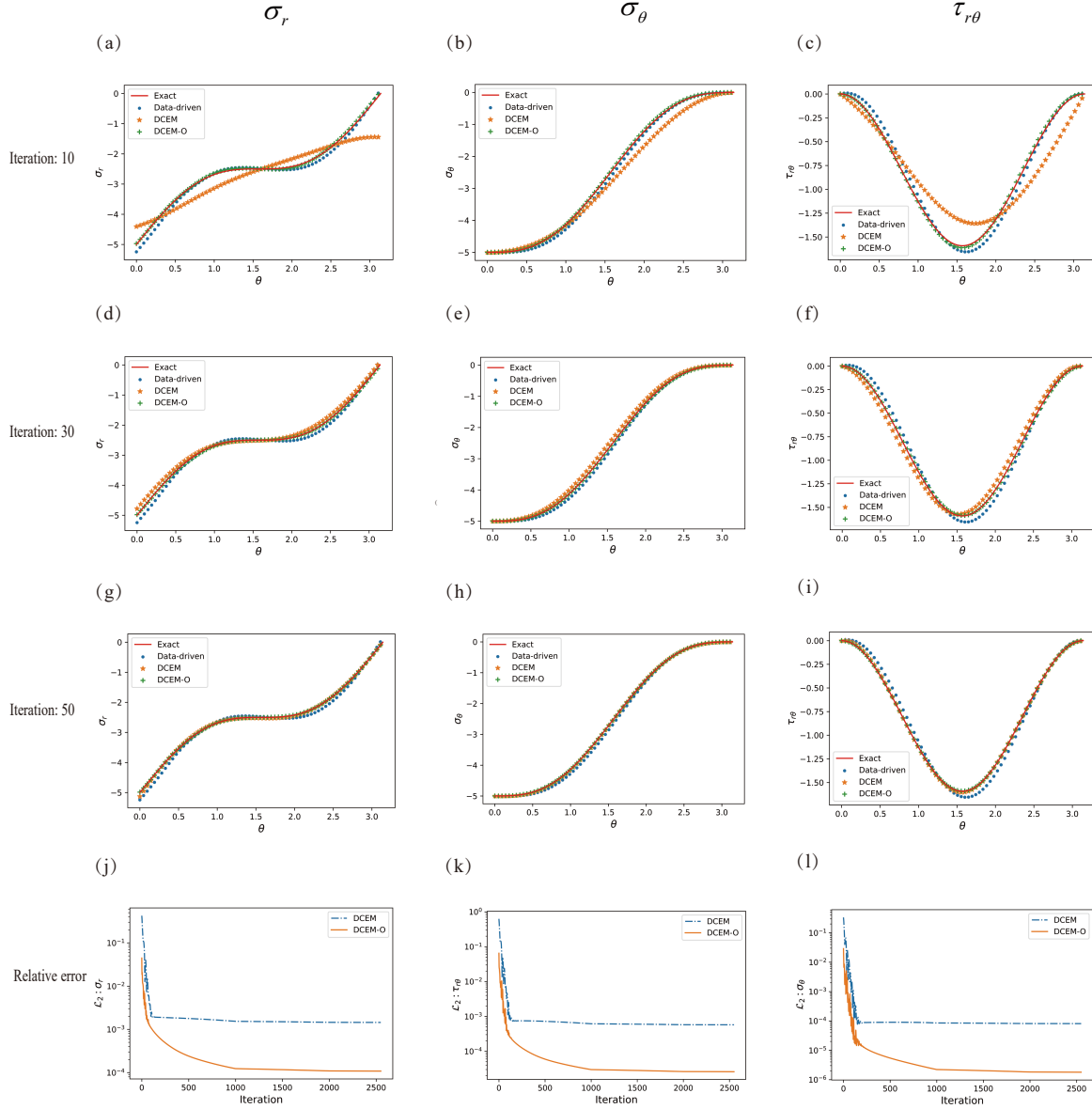


**FIGURE 16** Comparison of DCEM and DCEM-O in Airy stress function of the wedge: (a, b, c), (d, e, f), and (g, h, i) the prediction of  $\sigma_r$ ,  $\sigma_\theta$ , and  $\tau_{r\theta}$  in the number of iterations 100, 500, and 1000 respectively; Data-driven means pure data-driven by DeepONet. The evolution of the overall relative error  $\mathcal{L}_2$  by DCEM and DCEM-O:  $\sigma_r$  (a, d, g, j);  $\sigma_\theta$  (b, e, h, k);  $\tau_{r\theta}$  (c, f, i, l). (j, k, l) is evolution of the relative error  $\mathcal{L}_2^{rel}$  of  $\sigma_r$ ,  $\sigma_\theta$ , and  $\tau_{r\theta}$  respectively with the number of iterations.

### 4.1.3 | Non-uniform tension of plate and central hole: irregular domains

The plate problem is a common problem in solid mechanics, where the square plate with a central hole is often used as a benchmark for stress concentration phenomena, as shown in Fig. 17. In the case of the square plate, as shown in Fig. 17a, the left boundary is subjected to fixed boundary conditions, which means restricting both displacement and rotation to be zero. In the circular hole case, DCEM does not require the construction of possible fields for displacement boundary conditions, so we set the boundary of the hole in the square plate problem to be a fixed boundary. Additionally, non-uniform stretching forces are applied along the boundaries (both the square plate and central hole cases have non-uniform sinusoidal distribution of load), and the specific loading is as shown in Fig. 17b. To break the symmetry of the square plate with a

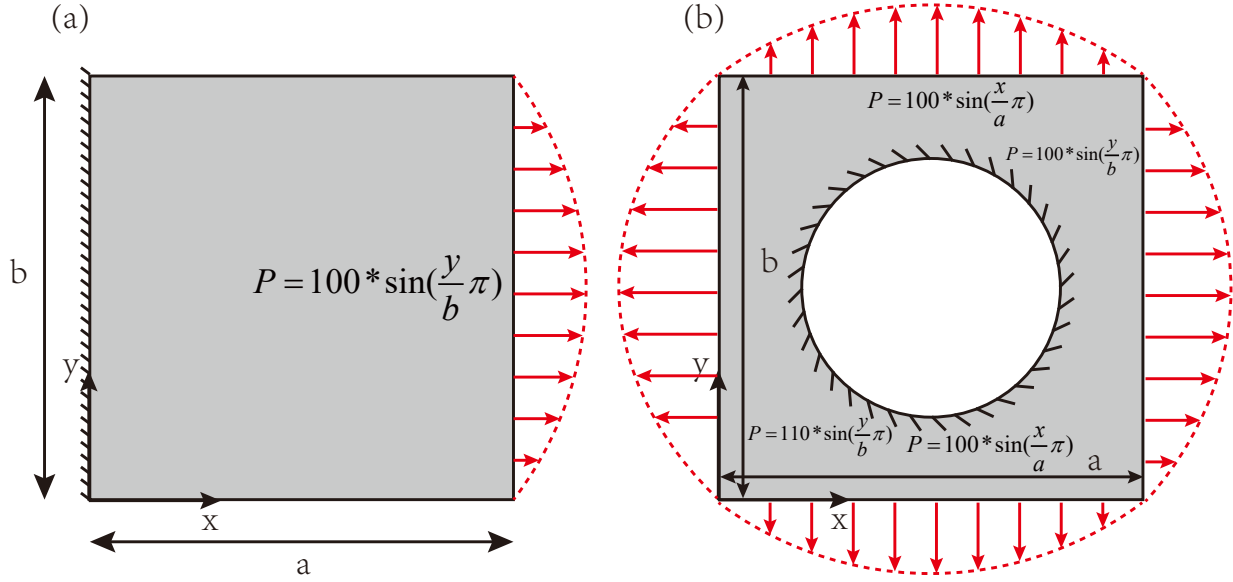


**FIGURE 17** The schematic of non-uniform stretching forces of plate and central hole where the material properties are set with Young's modulus  $E = 70$  MPA and Possion rate  $\nu = 0.3$ : (a) The non-uniform tension of the plate problem where  $a = b = 1$ . The applied force follows a sinusoidal distribution on the right boundary, while the left boundary is subject to a fixed boundary condition. (b) The non-uniform tension of the central hole where  $a = b = 1$ , the boundary of the hole is subjected to a fixed boundary condition, and all the other four sides of the boundary are under the sinusoidal distribution. Specifically, the upper and lower boundaries are  $P = 100\sin(\pi x/a)$ , the right boundary is defined as  $P = 100\sin(\pi y/b)$  and left boundary is subjected to higher force with  $P = 110\sin(\pi y/b)$ .

hole, the magnitude of the load on the left boundary is set to 110, while the other three sides have the same load magnitude of 100. The dimensions are chosen as  $a = b = 1$  mm, the radius of the circular hole is 0.25 mm, and the center of the circle is at the center of the square plate (0.5, 0.5). The Young's modulus is 1000 MPa, and the Poisson's ratio is 0.3.

In the first application of non-uniform tension of plate as shown in Fig. 17a, since there is no analytical solution to the problem of non-uniform stretching of square plates, we rely on the Finite Element Method (FEM) as a reference solution. An extremely fine mesh size is 0.01 mm (200\*200: 40,000 elements in total) in Abaqus/standard. After we refine the mesh further, the result of stress does not change except for the corner of the rectangle due to its singularity. The element type is CPS8R, which means the eight node plane stress element called 8-node serendipity element in FEM (a general purpose plane stress element and R means reduced integration). In this straightforward mechanical problem, the obtained results are considered as the exact solution for the purpose of evaluating the accuracy of DEM and DCEM. The boundary condition of the problem is

$$\begin{aligned}
 u_x|_{x=0} &= 0, & u_y|_{x=0} &= 0 \\
 t_x|_{y=0} &= 0, & t_y|_{y=0} &= 0 \\
 t_x|_{y=b} &= 0, & t_y|_{y=b} &= 0 \\
 t_x|_{x=a} &= 100\sin(\frac{\pi y}{b}), & t_y|_{x=a} &= 0.
 \end{aligned} \tag{65}$$

In order to compare the performance of DEM and DCEM, we focus on the stress predictions. In DEM, the admissible displacement is constructed as

$$\begin{aligned}
 u_x &= x * NN_1(x, y; \theta) \\
 u_y &= x * NN_2(x, y; \theta).
 \end{aligned} \tag{66}$$

The loss function of DEM is

$$\begin{aligned}
\mathcal{L}_{DEM} &= U + V \\
U &= \int_0^a \int_0^b \frac{1}{2} \varepsilon_{ij} \sigma_{ij} dx dy \\
&= \int_0^a \int_0^b \frac{E}{2(1-\nu^2)} \left[ \left( \frac{\partial u_x}{\partial x} \right)^2 + 2\nu \frac{\partial u_x}{\partial x} \frac{\partial u_y}{\partial y} + \left( \frac{\partial u_y}{\partial y} \right)^2 + (1-\nu) \left( \frac{\partial u_x}{\partial y} + \frac{\partial u_y}{\partial x} \right)^2 \right] dx dy \\
V &= \int_0^b t_i u_i dy = \int_0^b t_x |_{x=a} u_x dy = \int_0^b 100 \sin\left(\frac{\pi y}{b}\right) u_x dy
\end{aligned} \tag{67}$$

The output are 2D displacement  $(u_x, u_y)$ , because outputs of two independent networks with different parameters is more accurate than the outputs of single network<sup>41</sup>.

In DCEM, the particular neural network  $NN_p$  is trained in advance to satisfy the force boundary condition on upper, right and lower boundary. These conditions are mathematically expressed as followed:

$$\begin{cases} n_x \frac{\partial^2 \phi}{\partial y^2} - n_y \frac{\partial^2 \phi}{\partial x \partial y} = t_x \\ n_y \frac{\partial^2 \phi}{\partial x^2} - n_x \frac{\partial^2 \phi}{\partial x \partial y} = t_y \end{cases}, \tag{68}$$

where  $n_x$  and  $n_y$  represent the components of the outward normal vector at each boundary point. The quantities  $t_x$  and  $t_y$  correspond to the prescribed forces along the x and y directions, respectively. This formulation ensures that the force boundary conditions are fulfilled within the DCEM framework. The particular network is set to 4 hidden layers and 20 neurons in each layer. The dimension of input is two, i.e., x and y coordinate, and the output is only the Airy stress function, and the learning rate is 1e-3. Through the Eq. (40), the basis function is defined as

$$F_b(x, y) = \frac{1}{64ab^2} [(x-a)(y)(y-b)]^2. \tag{69}$$

As a result, the admissible stress function is followed as

$$\phi = NN_p(x, y) + F_b(x, y) * NN_g(x, y; \theta) \tag{70}$$

It is easy to verify that the force boundary condition is satisfied due to the formual of the basis function.  $NN_g$  is the gernal network and is trained using the principle of the complementary energy. Its architecture and the training scheme are identical to the particular neural network  $NN_p$ . The loss function of DCEM is

$$\begin{aligned}
\mathcal{L}_{DCEM} &= U_c + V_c \\
U_c &= \int_0^a \int_0^b \frac{1}{2} \varepsilon_{ij} \sigma_{ij} dx dy \\
&= \int_0^a \int_0^b \frac{1}{2E} \left[ \left( \frac{\partial^2 \phi}{\partial x^2} \right)^2 + \left( \frac{\partial^2 \phi}{\partial y^2} \right)^2 - 2\nu \frac{\partial^2 \phi}{\partial x^2} \frac{\partial^2 \phi}{\partial y^2} + 2(1+\nu) \left( \frac{\partial^2 \phi}{\partial x \partial y} \right)^2 \right] dx dy \\
V_c &= \int_0^b t_i u_i dy = \int_0^b (t_x u_x |_{x=a} + t_y u_y |_{x=a}) dy = 0.
\end{aligned} \tag{71}$$

To ensure a fair comparison between DEM and DCEM, all the conditions including training scheme, network architecture, and point distribution are kept the same. The point distribution is a uniform grid with a size of 101\*101.

Fig. 18 illustrate the stress prediction results. Both DEM and DCEM have achieved good results, but when it comes to capturing singular stress at the corners, DCEM demonstrates a superior stress prediction performance. Fig. 18a,b,c show the Von-Mises stress at different locations obtained by both methods. DCEM is notably more accurate than DEM in capturing stress values. Fig. 18d shows the relative overall  $\mathcal{L}_2$  error where DCEM outperforms DEM in all stress components. Besides, DCEM has faster convergence speed compared to DEM. For an efficiency comparison between DEM and DCEM, Table 4 demonstrates that the calculation time of DCEM is one-tenth of that of DEM.

The second numerical example involves the non-uniform tension of a specimen with a central hole, as depicted in Fig. 17b. This problem possesses an irregular geometry and can be challenging to solve with DEM when using uniform point distribution and basic Monte Carlo integration<sup>53</sup>. The FEM solution obtained from Abaqus/standard serves as the

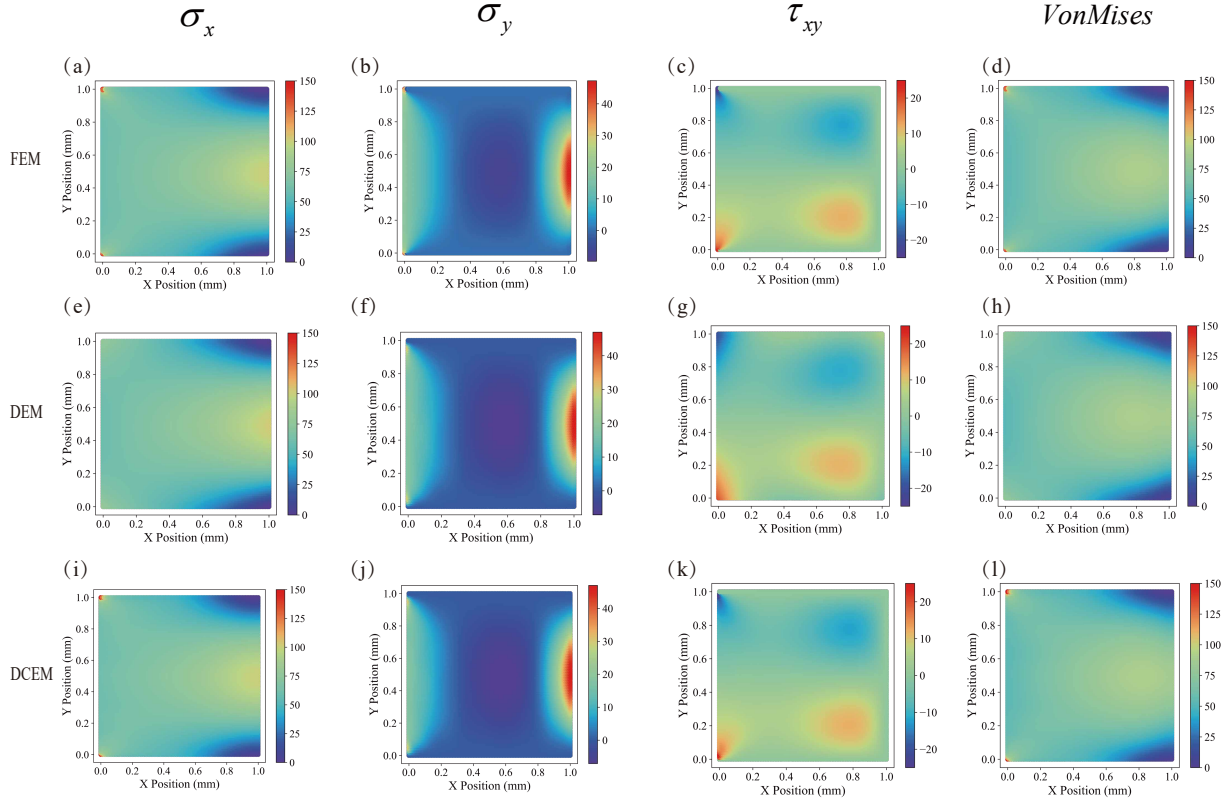


**FIGURE 18** Comparison of FEM, DEM, and DCEM in term of stress in non-uniform tension of plate: The result of FEM (a, b, c, d), DEM (e, f, g, h) and DCEM (i, j, k, l). The result of  $\sigma_x$  (a, e, i),  $\sigma_y$  (b, f, j),  $\tau_{xy}$  (c, g, k), and Von-Mises stress (d, h, l).

**TABLE 4** Comparison of efficiency and accuracy between FEM, DEM and DCEM in non-uniform tension of plate and central hole problem.

Relative error and converge time	Plate			Central hole		
	Points	Relative error of VonMises	Time(s)	Points	Relative error of VonMises	Time(s)
FEM	CPS8R: 40000(ele)	Reference solution	42.09s	CPS8R: 39806(ele)	Reference solution	45.44s
DEM	101*101	0.01109	525.7s	101*101	0.04802	438.7s
DCEM	101*101	0.003728	54.4s	101*101	0.01991	48.1s

reference solution, utilizing 39,806 CPS8R elements. The governing equation remains the same as the rectangular problem, as expressed in Eq. (67) and Eq. (71). All settings are consistent with the plate problem, with the exception of the boundary conditions:

$$\begin{aligned}
 t_x|_{x=0} &= -110\sin\left(\frac{\pi y}{b}\right), t_y|_{x=0} = 0 \\
 t_x|_{y=0} &= 0, t_y|_{y=0} = -100\sin\left(\frac{\pi x}{a}\right) \\
 t_x|_{y=b} &= 0, t_y|_{y=b} = 100\sin\left(\frac{\pi x}{a}\right) \\
 t_x|_{x=a} &= 100\sin\left(\frac{\pi y}{b}\right), t_y|_{x=a} = 0.
 \end{aligned} \tag{72}$$

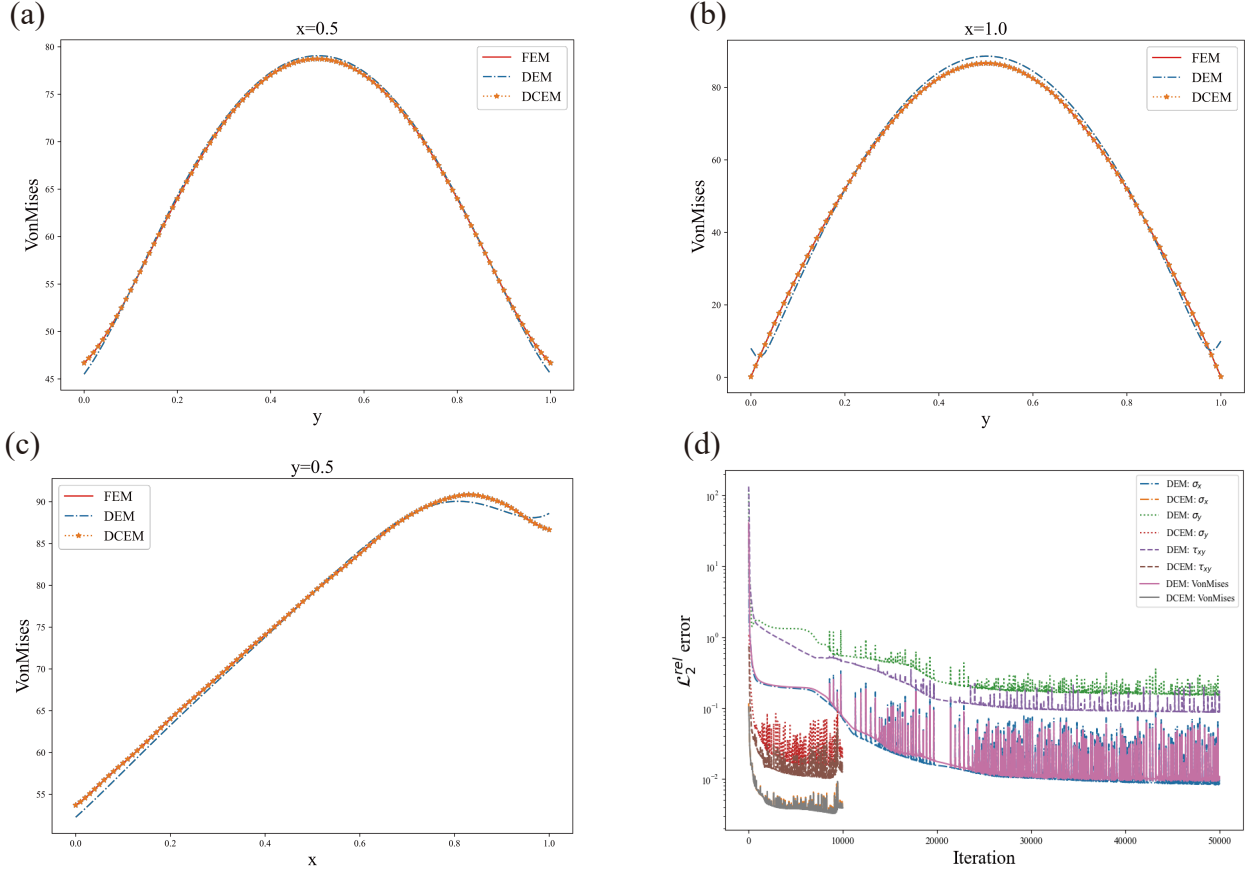


**FIGURE 19** Different location comparison among FEM, DEM, and DCEM in non-uniform tension of plate: Von-Mises on the line of  $x = 0.5$  (a), right boundary  $x = 1.0$  (b),  $y = 0.5$  (c). The overall relative error  $\mathcal{L}_2$  in  $\sigma_x$ ,  $\sigma_y$ ,  $\tau_{xy}$ , and Von-Mises (d).

In DEM, the admissible displacement is constructed as

$$\begin{aligned} u_x &= \left[ \left( \frac{x-0.5}{0.25} \right)^2 + \left( \frac{y-0.5}{0.25} \right)^2 - 1 \right] * NN_1(x, y; \boldsymbol{\theta}) \\ u_y &= \left[ \left( \frac{x-0.5}{0.25} \right)^2 + \left( \frac{y-0.5}{0.25} \right)^2 - 1 \right] * NN_2(x, y; \boldsymbol{\theta}). \end{aligned} \quad (73)$$

In DCEM, due to the fixed displacement boundary (Dirichlet boundary), there's no requirement to handle the boundary of the hole, giving DCEM an advantage in dealing with complex Dirichlet boundaries, attributed to the principle of complementary energy. Fig. 20 illustrate the highly accurate stress results obtained by DCEM. DCEM effectively captures stress concentration, demonstrating its efficiency as shown in Table 4. Fig. 21a,b,c show the Von-Mises stress at different locations obtained by DEM and DCEM. Fig. 21d indicates DCEM's accurate results near the hole boundary, even with uniform distribution (In FEM, the fine mesh is needed). Table 4 and Fig. 21e display the faster convergence speed of DCEM compared to DEM.

In conclusion, DCEM yields superior stress results in elasticity problems. We also present results for other shapes, such as an ellipse, in Fig. 22.



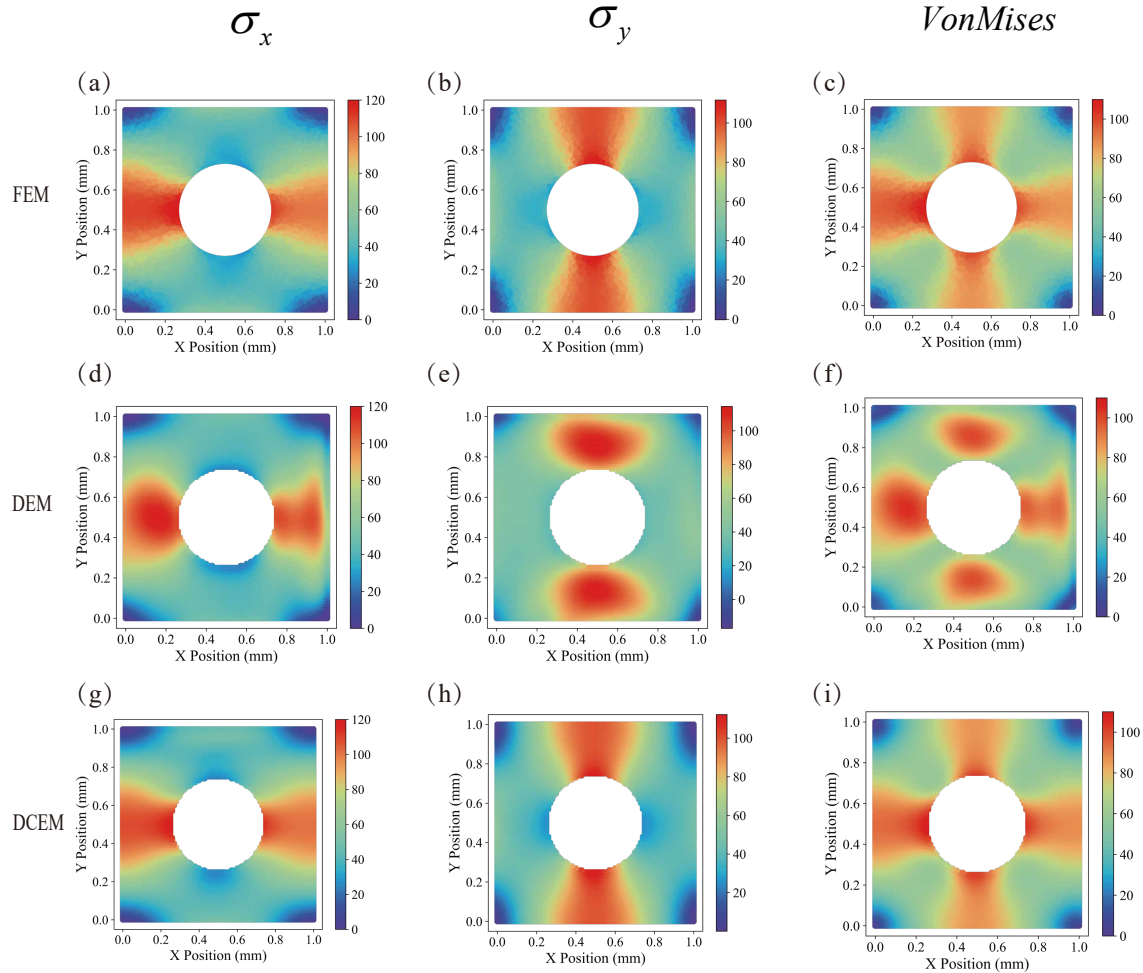


FIGURE 20 Comparison of FEM, DEM, and DCEM in term of stress in non-uniform tension of central hole:

## 4.2 | Prandtl stress function: full natural boundary conditions

A cylindrical rod is a common engineering component that can withstand different loads such as tension, compression, bending, and torsion. The free torsion problem of cylindrical rods is a common problem in engineering<sup>79</sup>, which is often used to transmit torque, as shown in Fig. 23a.

Two common solutions are introduced in Section 2.4, namely the displacement solution and the stress function solution. The strong form expression of the displacement solution is:

$$\begin{cases} \frac{\partial^2 \psi}{\partial x^2} + \frac{\partial^2 \psi}{\partial y^2} = 0 & \mathbf{x} \in \Omega \\ \frac{\partial \psi}{\partial x} n_x + \frac{\partial \psi}{\partial y} n_y = y n_x - x n_y & \mathbf{x} \in \partial\Omega \\ \alpha G \iint (x^2 + y^2 + x \frac{\partial \psi}{\partial y} - y \frac{\partial \psi}{\partial x}) dx dy = M_t, \end{cases} \quad (74)$$

where  $\psi$  is the warping function and  $\alpha$  is rate of twist. The displacement assumption can be written as:

$$\begin{aligned} u &= -\alpha z y \\ v &= \alpha z x \\ w &= \alpha \psi(x, y). \end{aligned} \quad (75)$$

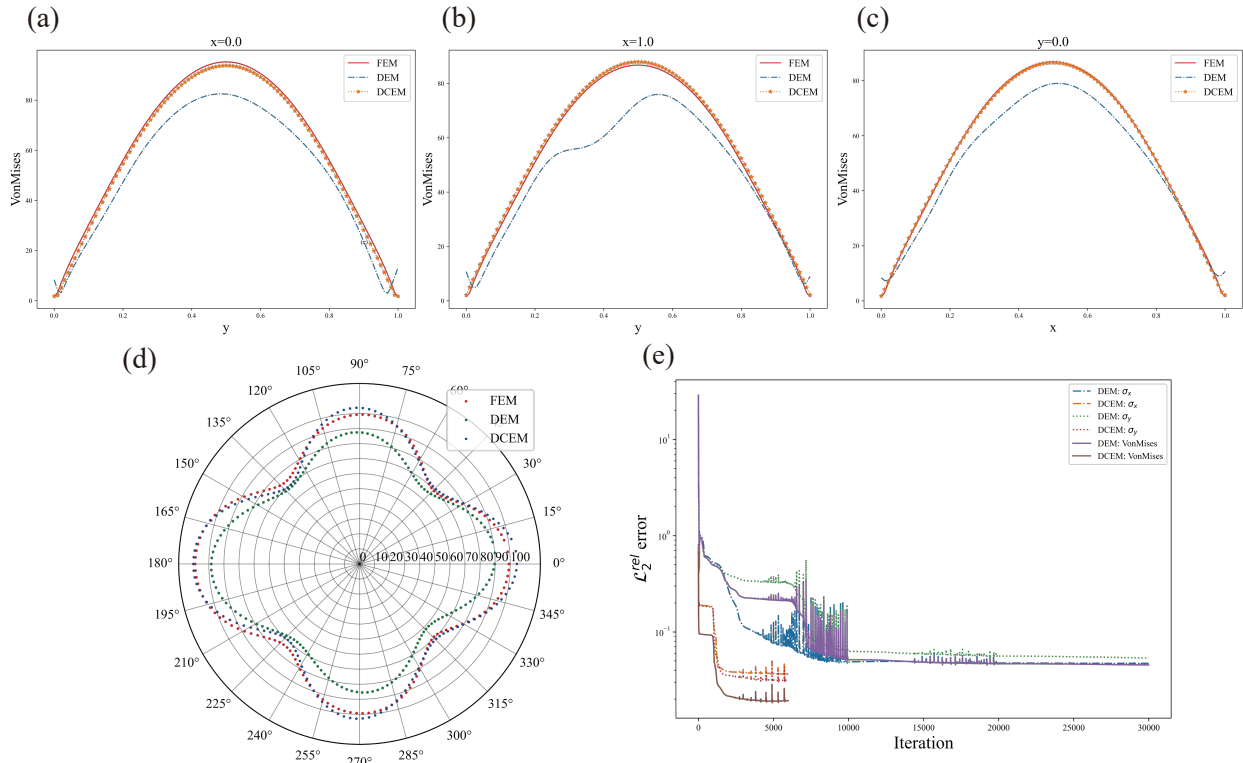


FIGURE 21 Different location comparison among FEM, DEM, and DCEM in non-uniform tension of central hole:

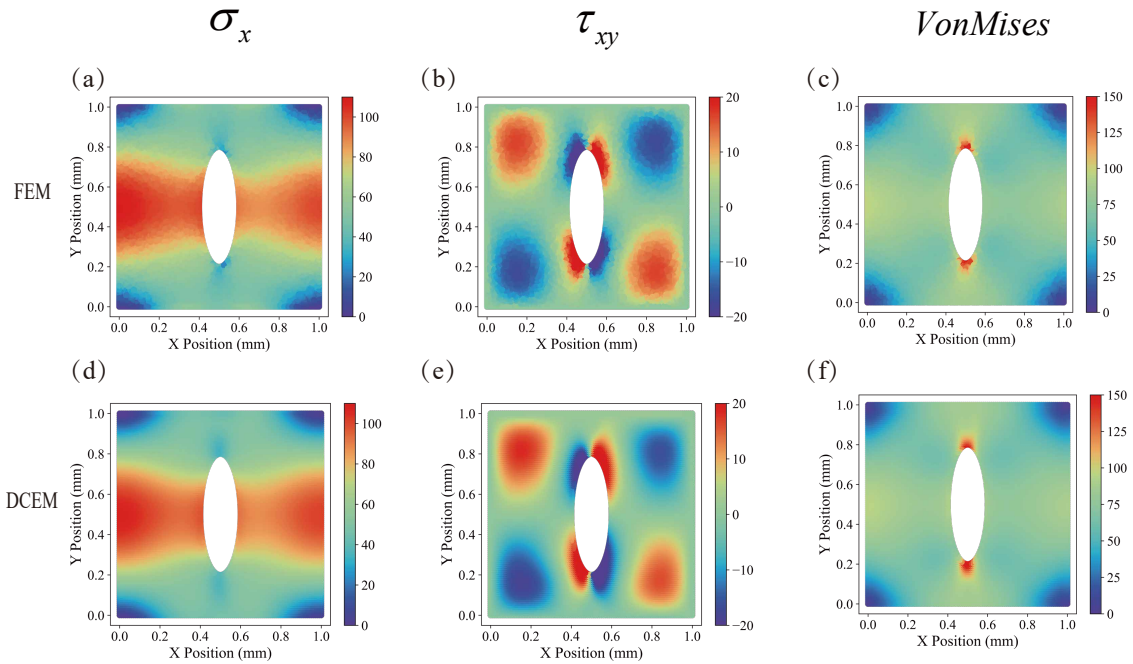
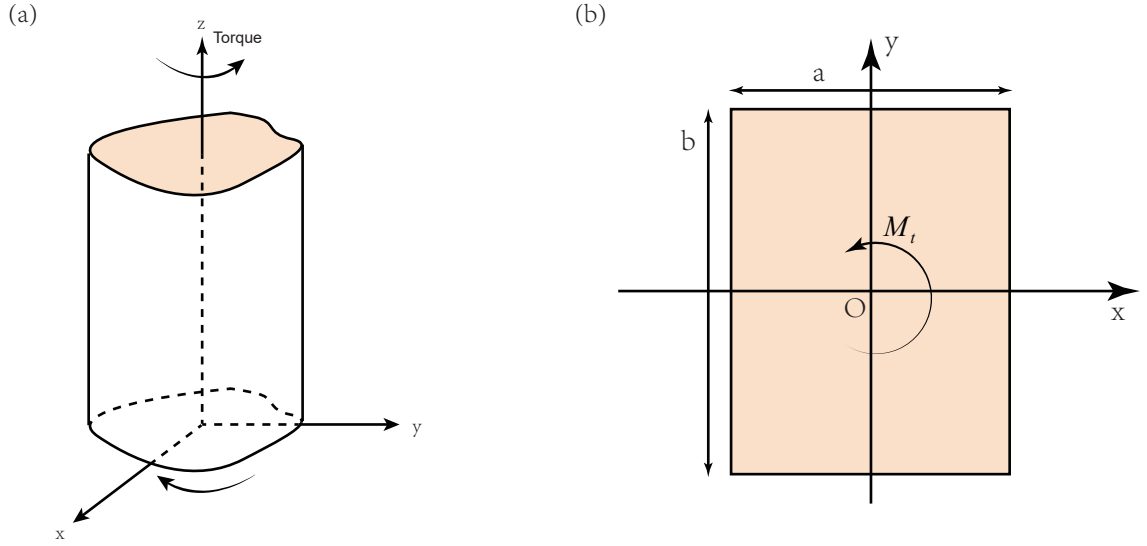


FIGURE 22 Comparison of FEM, DEM, and DCEM in term of stress in non-uniform tension of ellipse hole:



**FIGURE 23** The schematic of the problem of torsion of a cylindrical body (a) and square cross-section of the cylinder (b)

We usually solve the Laplace equation with Neumann boundary conditions first, and get the  $\psi$ . Then we substitute the  $\psi$  into the end boundary condition  $\alpha G \iint (x^2 + y^2 + x\partial\psi/\partial y - y\partial\psi/\partial x)dxdy = M_t$  to get the unknown constant  $\alpha$ .

The energy form of the displacement solution based on the principle of minimum potential energy (DEM) is:

$$\Pi = L \int_{\Omega} \left( \frac{1}{2} \gamma_{zx} \tau_{zx} + \frac{1}{2} \gamma_{zy} \tau_{zy} \right) dxdy - \alpha LM_t, \quad (76)$$

where  $L$  is the length of the cylinder. We substitute the displacement expressed as Eq. (75) into the potential, and obtain

$$\Pi = L \int_{\Omega} \frac{1}{2} G \alpha^2 \left[ \left( \frac{\partial\psi}{\partial x} - y \right)^2 + \left( \frac{\partial\psi}{\partial y} + x \right)^2 \right] dxdy - \alpha LM_t. \quad (77)$$

The constant term  $\alpha LM_t$  and  $G\alpha^2/2$  are removed, because it does not affect the optimization results of  $\psi$ . The above optimization problem is transformed into:

$$\psi = \arg \min_{\psi} \left\{ \int_{\Omega} \left[ \left( \frac{\partial\psi}{\partial x} - y \right)^2 + \left( \frac{\partial\psi}{\partial y} + x \right)^2 \right] dxdy \right\}. \quad (78)$$

It is worth noting that the warping function  $\psi$  will have an undetermined constant in the free torsion problem of the cylindrical rod. This undetermined constant is the displacement of the rigid body and determined by the given boundary condition. If it involves strain and the derivative of the displacement function, this constant will not have an impact.

In the other solution of stress, the strong form of the stress function solution is (considering simply connected regions):

$$\begin{cases} \frac{\partial^2 \phi}{\partial^2 x} + \frac{\partial^2 \phi}{\partial^2 y} = -2G\alpha & \mathbf{x} \in \Omega \\ \phi = 0 & \mathbf{x} \in \partial\Omega \\ M_t = 2 \int_{\Omega} \phi d\Omega. \end{cases} \quad (79)$$

In the stress function solution, the  $\alpha$  is unknown in advance, so it cannot be solved directly. Here, the pre-assumption method is used, assuming  $C_1 = -2G\alpha$ , to solve:

$$\begin{cases} \frac{\partial^2 \phi}{\partial^2 x} + \frac{\partial^2 \phi}{\partial^2 y} = C_1 & \mathbf{x} \in \Omega \\ \phi = 0 & \mathbf{x} \in \partial\Omega. \end{cases} \quad (80)$$

The solution result is recorded as  $\phi_1$ , and  $\phi_1$  is brought into the torque formula  $M_1 = 2 \int_{\Omega} \phi_1 d\Omega$  to correct

$$\phi = \frac{M_t}{M_1} \phi_1 \quad (81)$$

According to the uniqueness of the elastic mechanics' solution, the above revised  $\phi$  in Eq. (81) is the true solution to the problem. Bring the corrected  $\phi$  into the domain equation, and correct  $C_1$

$$\frac{\partial^2 \phi}{\partial^2 x} + \frac{\partial^2 \phi}{\partial^2 y} = \frac{M_t}{M_1} \left( \frac{\partial^2 \phi_1}{\partial^2 x} + \frac{\partial^2 \phi_1}{\partial^2 y} \right) = \frac{M_t}{M_1} C_1. \quad (82)$$

Thus  $\alpha$  can be written as:

$$\alpha = -\frac{M_t C_1}{2M_1 G}. \quad (83)$$

Next, We consider DCEM, i.e., the minimum complementary energy form of the stress function solution, which can be written as (considering simply connected regions):

$$\phi = \arg \min_{\phi} \{ \Pi_c = \frac{L}{G} \int_{\Omega} \frac{1}{2} [(\frac{\partial \phi}{\partial x})^2 + (\frac{\partial \phi}{\partial y})^2] dx dy - \alpha L \int_{\Omega} 2\phi dx dy \}. \quad (84)$$

The minimum complementary energy solution also encounters the same problem as the strong form of the stress function ( $\alpha$  is not known in advance). Since the first-order variation of the complementary energy is equivalent to the strong form, the same approach can be adopted, setting  $\alpha = \alpha_1$ , to solve the minimum complementary energy form, and bring the obtained  $\phi_1$  into the torque formula  $M_1 = 2 \int_{\Omega} \phi_1 d\Omega$ , and we correct

$$\begin{aligned} \phi &= \frac{M_t}{M_1} \phi_1 \\ \alpha &= \frac{M_t}{M_1} \alpha_1. \end{aligned} \quad (85)$$

We take a rectangular cylinder as an example in Fig. 23b to show the comparison between the prediction and analytical solution of the torsion angle  $\alpha$  of the above four methods: PINNs strong form of displacement, DEM, PINNs strong form of stress function, and DCEM. The four methods' neural network structure, optimization scheme and point allocation strategy are the same. The neural network structure is the x and y coordinates of 2 neurons in the input layer, 2 hidden layers, 20 neurons in each layer, the output is one neuron, the activation function is tanh, the output layer without activated function; the optimization scheme is Adam; the initialization method is Xavier; all the internal point allocation methods of the four methods are randomly distributed, 10,000 points and the strong displacement form needs to allocate additional boundary points on the boundary, 1000 points per side, also randomly distributed. Fig. 24 show that, for different  $a/b$  aspect ratios, the four methods converge to the exact solution when increasing with the number of iterations, which shows that the four methods can predict the rotation angle  $\alpha$  of unit length. It is worth noting that the DEM does not require to assume an admissible displacement field because all boundaries are force boundary conditions; However, the DCEM based on the minimum complementary energy principle needs to assume an admissible stress function. The stress function of the boundary is assumed to be a constant zero. Due to the regular geometry of the problem, the admissible stress function of the boundary condition is satisfied by the coordinate construction method in advance:

$$\phi = (x^2 - \frac{a^2}{4})(y^2 - \frac{b^2}{4})NN(x, y; \theta). \quad (86)$$

The loss function of the strong form of displacement in PINNs is

$$\begin{aligned} \mathcal{L}_{strongdis} &= \lambda_1 \frac{1}{N_{dom}} \sum_{i=1}^{N_{dom}} \left| \frac{\partial^2 \psi(\mathbf{x}_i)}{\partial^2 x} + \frac{\partial^2 \psi(\mathbf{x}_i)}{\partial^2 y} \right|^2 \\ &+ \lambda_2 \frac{1}{N_b} \sum_{i=1}^{N_b} \left| \frac{\partial \psi(\mathbf{x}_i)}{\partial x} n_x + \frac{\partial \psi(\mathbf{x}_i)}{\partial y} n_y - y_i n_x + x_i n_y \right|^2, \end{aligned} \quad (87)$$

where we set  $\lambda_1 = \lambda_2 = 1$ . The strong form of the PINNs stress function does not use a penalty function to satisfy the boundary conditions but uses an admissible stress function consistent with the DCEM to satisfy the force boundary

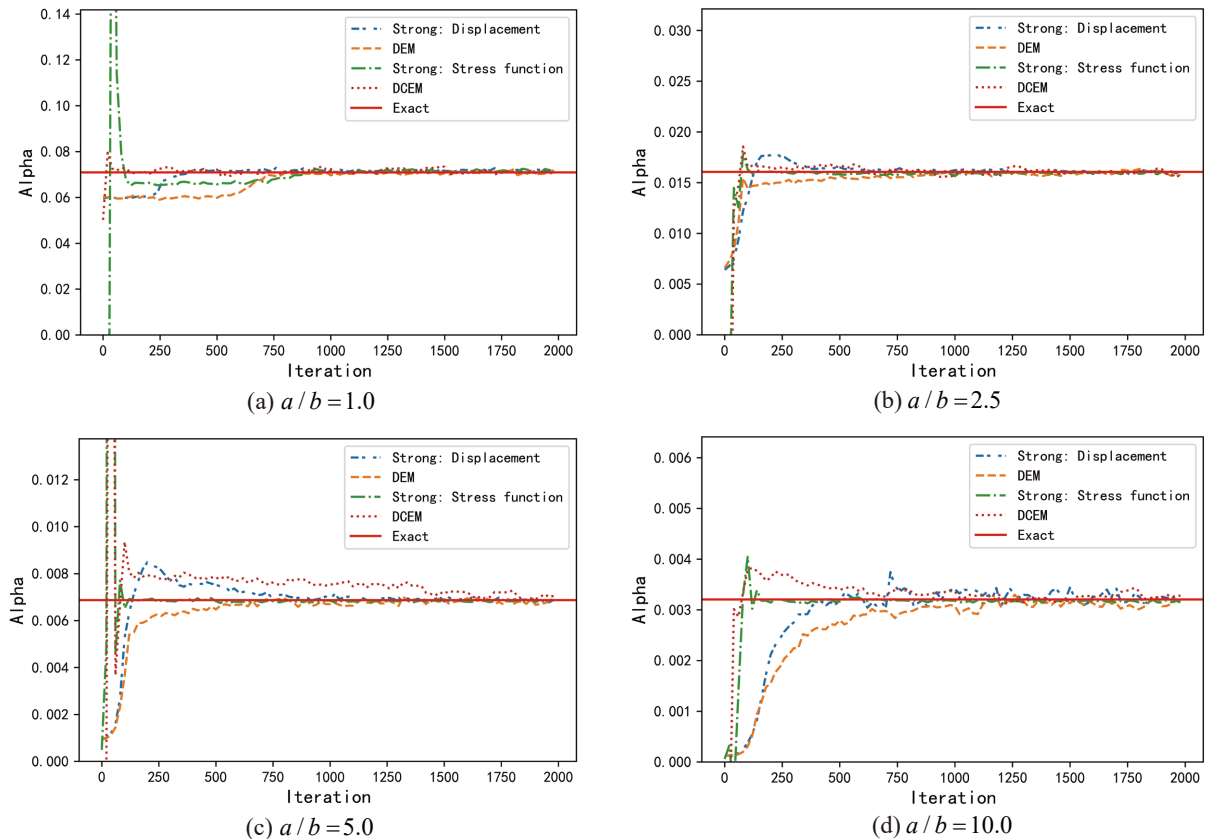


**FIGURE 24** Comparison of the numerical solution and analytical solution of the rotation angle  $\alpha$  in the different rectangular cylinder (aspect ratio  $a/b$ ) under the four models of PINNs displacement strong form, DEM based on the minimum potential energy, PINNs stress function strong form and DCEM based on the minimum complementary energy.

conditions, so there are no additional hyperparameters in the strong form of PINNs stress function and DCEM. The strong form of PINNs stress function and DCEM both assume  $\alpha = 0.0005$ .

In order to accurately compare the accuracy of the four methods, we analyze more examples, different aspect ratios  $a/b$  correspond to different exact solutions  $\alpha$  and maximum shear stress  $\tau_{max}$ , as shown in Table 5. The analytical expressions of  $\alpha$  and  $\tau_{max}$  are:

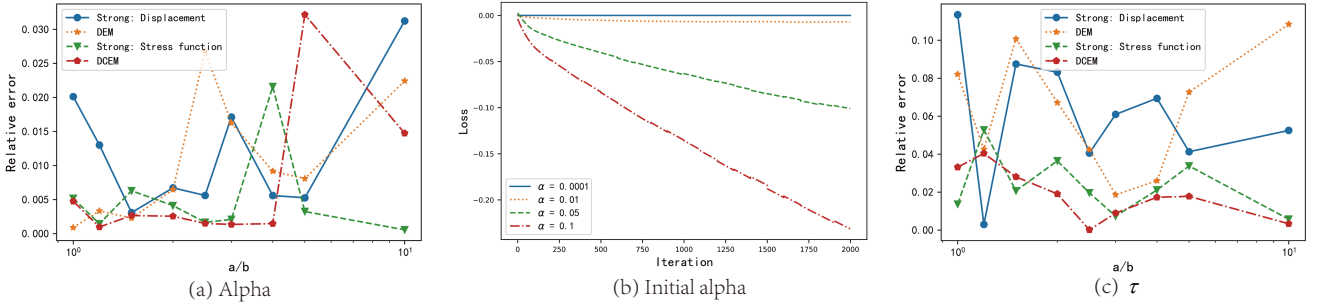
$$\alpha = \frac{M_t}{\beta G a b^3} \quad (88)$$

$$\tau_{max} = \frac{M_t}{\beta_1 a b^2}$$

Fig. 25a gives the relative error  $|pred - exact|/exact$  of  $\alpha$  under different aspect ratio  $a/b$ . The number of iterations of all methods is 2000, and all configurations related to training are the same, the results show that under the same number of iterations, the accuracy of the four methods is similar. From the perspective of computational efficiency, DEM and DCEM can be computationally more efficient due to the lower order of the derivative than the corresponding strong form of displacement and stress function theoretically. Therefore, all four methods can obtain satisfactory results under different rectangular sizes. Since all boundaries are force boundary conditions, DEM does not require additional construction of admissible displacement fields in advance, which is a great advantage compared to the DCEM. From the other extreme, if all the boundaries are displacement boundary conditions which we show in Section 4.1.1, the DCEM does not need to construct the admissible stress function field in advance. Therefore, different energy principles have different advantages under different types of boundary conditions.

**TABLE 5** Analytical solutions of  $\alpha$  and the maximum shear stress  $\tau_{max}$  of a rectangular cylinder under different  $a/b$  aspect ratios

Aspect ratio $a/b$	$\beta$	Torsion angle $\alpha$	$\beta_1$	$\tau_{max}$
1.0	0.141	70.922	0.208	48076.923
1.2	0.166	50.201	0.219	38051.750
1.5	0.196	34.014	0.20231	28860.029
2.0	0.229	21.834	0.246	20312.203
2.5	0.249	16.064	0.258	15503.876
3.0	0.263	12.672	0.267	12484.395
4.0	0.281	8.897	0.282	8865.248
5.0	0.291	6.873	0.291	6872.852
10.0	0.312	3.205	0.312	3205.128

**FIGURE 25** (a) Relative error of rotation angle  $\alpha$  of a rectangular cylinder under four models under PINNs displacement strong form, DEM, PINNs stress function strong form and DCEM. (b) The effect of different initial  $\alpha$  on the convergence rate under DCEM. (c) Relative error of the maximum shear stress  $\tau$  of the rectangular cylinder under the strong form of PINNs displacement, DEM, the strong form of PINNs stress function and DCEM.**TABLE 6** Comparison of accuracy and convergence time of torsion angle  $\alpha$  under different aspect ratios  $a/b$  under the four models of PINNs displacement strong form, DEM, PINNs stress function strong form and DCEM

Aspect ratio $a/b$	Torsion angle $\alpha$ : relative error and convergence time			
	PINNs strong form: Dis	DEM	PINNs strong form: Stress	DCEM
1.0	1.51%, 25.9s	0.73%, 19.4s	1.02%, 12.4s	0.65%, 3.4s
1.2	1.32%, 12.1s	0.65%, 9.1s	0.97%, 7.4s	0.12%, 9.2s
1.5	1.26%, 8.1s	0.74%, 9.1s	1.04%, 18.4s	0.64%, 9.4s
2.0	1.01%, 15.2s	0.93%, 9.5s	0.95%, 5.7s	0.27%, 4.7s
2.5	1.03%, 15.1s	1.07%, 15.7s	0.52%, 8.7s	0.13%, 3.7s
3.0	0.95%, 21.1s	1.04%, 17.4s	0.67%, 23.2s	0.42%, 6.7s
4.0	1.02%, 25.6s	1.12%, 12.2s	0.82%, 21.4s	0.13%, 2.6s
5.0	1.14%, 31.2s	1.14%, 20.7s	0.89%, 19.2s	0.43%, 8.2s
10.0	1.57%, 16.1s	1.04%, 24.2s	0.79%, 21.4s	0.27%, 8.3s
Mean error	1.21%	0.94%	0.85%	<b>0.34%</b>
Mean time	18.9s	15.3s	15.3s	<b>6.2s</b>

In order to further analyze the potential of the four methods, we cancel the limitation of the fixed number of iterations and calculate the relative error and convergence time of  $\alpha$  when convergence, as shown in the table Table 6. The computer hardware for all the numerical experiments is RTX2060, 6G GPU, and 16G RAM. Generally the DCEM and the DEM have higher calculation efficiency because of the low order of derivatives, especially DCEM.

Fig. 26 gives four methods to predict the maximum shear stress  $\tau$ , and the maximum shear stress effect of the four methods is good. The PINNs strong form of displacement and the DEM fluctuate greatly, but the PINNs strong form of

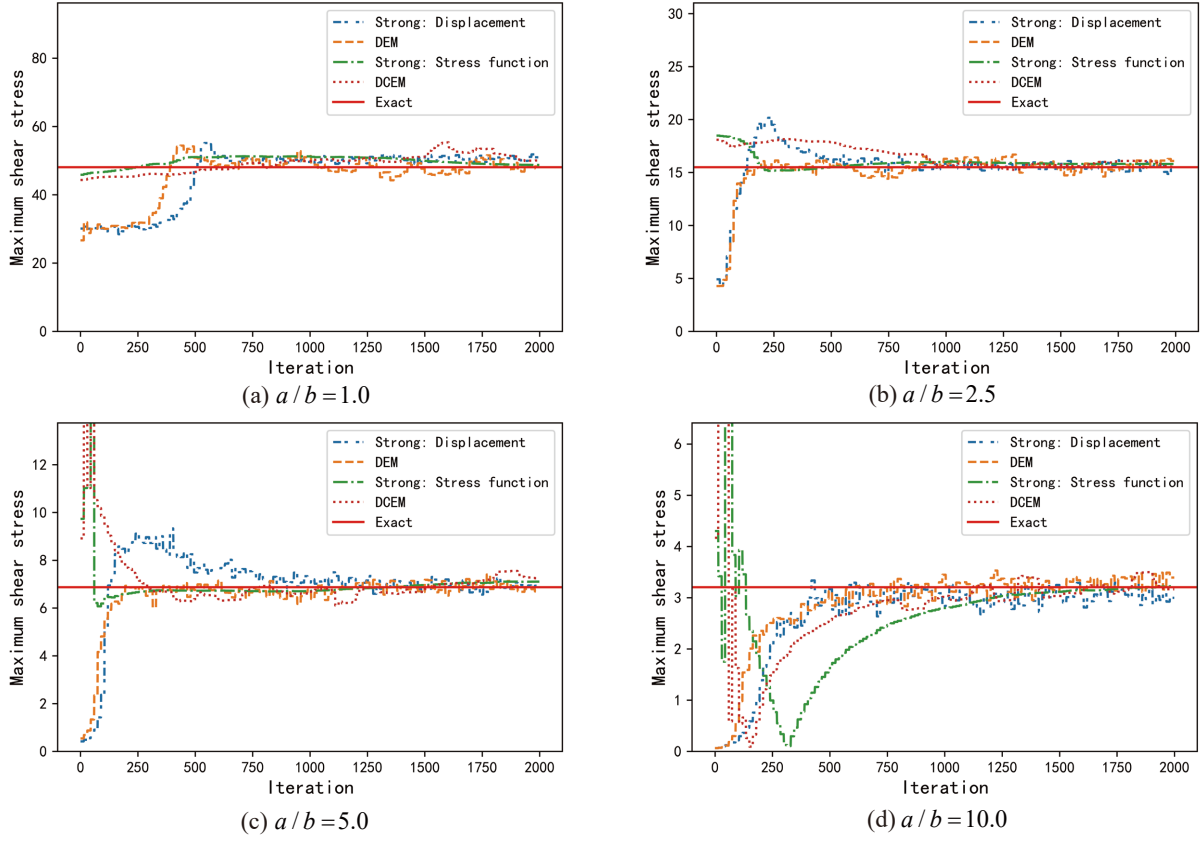


**FIGURE 26** Comparison of the numerical and analytical solutions of the maximum shear stress  $\tau$  of the rectangular cylinder under the strong form of PINNs displacement, DEM, the strong form of PINNs stress function and DCEM

stress function and the DCEM fluctuate less because the pre-setting  $\alpha$  affects the result of the stress solution, i.e., the initial prediction value will affect the accuracy and convergence speed. All four methods can predict maximum shear stress well, as is shown in Fig. 25c under different  $a/b$ .

DEM has been discussed in detail in<sup>1</sup>, so here we mainly discuss the DCEM based on the minimum complementary energy form, and we analyze the DCEM separately in this paper. Fig. 28c,f show that the maximum absolute error is mainly concentrated on the boundary, because the maximum shear stress is concentrated on the boundary, so it cannot show that the learning of the boundary is worse than that of the interior simply. On the whole, the predictive shear stress effect of DCEM is close to the exact solution. The  $\mathcal{L}_2^{rel}$  relative error norm and  $\mathcal{H}_1^{rel}$  relative error seminorm in DCEM are calculated as follows

$$\begin{aligned}
 \|e\|_{\mathcal{L}_2^{rel}} &= \frac{\|\phi^{pred} - \phi^{exact}\|_{\mathcal{L}_2}}{\|\phi^{exact}\|_{\mathcal{L}_2}} = \frac{\int_{\Omega} (\phi^{pred} - \phi^{exact})^2 dx dy}{\int_{\Omega} (\phi^{exact})^2 dx dy} \\
 \|e\|_{\mathcal{H}_1^{rel}} &= \frac{\|\phi^{pred} - \phi^{exact}\|_{\mathcal{H}_1}}{\|\phi^{exact}\|_{\mathcal{H}_1}} = \frac{\int_{\Omega} (E^{pred} - E^{exact})^2 dx dy}{\int_{\Omega} (E^{exact})^2 dx dy} \\
 E &= \int_{\Omega} \left( \frac{\partial \phi}{\partial x} \right)^2 + \left( \frac{\partial \phi}{\partial y} \right)^2 dx dy.
 \end{aligned} \tag{89}$$

Four different neural networks were constructed, each having a different number of hidden layers (HL): 1HL, 2HL, 3HL, and 4HL. Each hidden layer consists of 30 neurons. Additionally, the NNs were trained for various steps ranging from 100 to 1000. As shown in Fig. 27, all neural network architectures demonstrated promising results when compared with the exact solution. Moreover, the DCEM exhibited convergence concerning the training steps in both  $\mathcal{L}_2^{rel}$  and  $\mathcal{H}_1^{rel}$  norms.

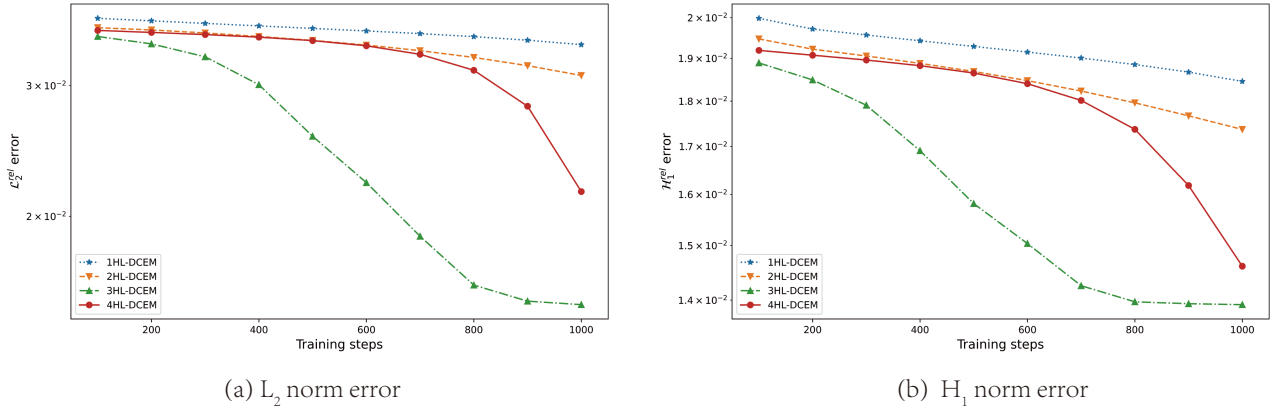


**FIGURE 27** The error in terms of  $\mathcal{L}_2^{rel}$  norm and  $\mathcal{H}_1^{rel}$  seminorm of DCEM with respect to the training steps in Prandtl stress function.

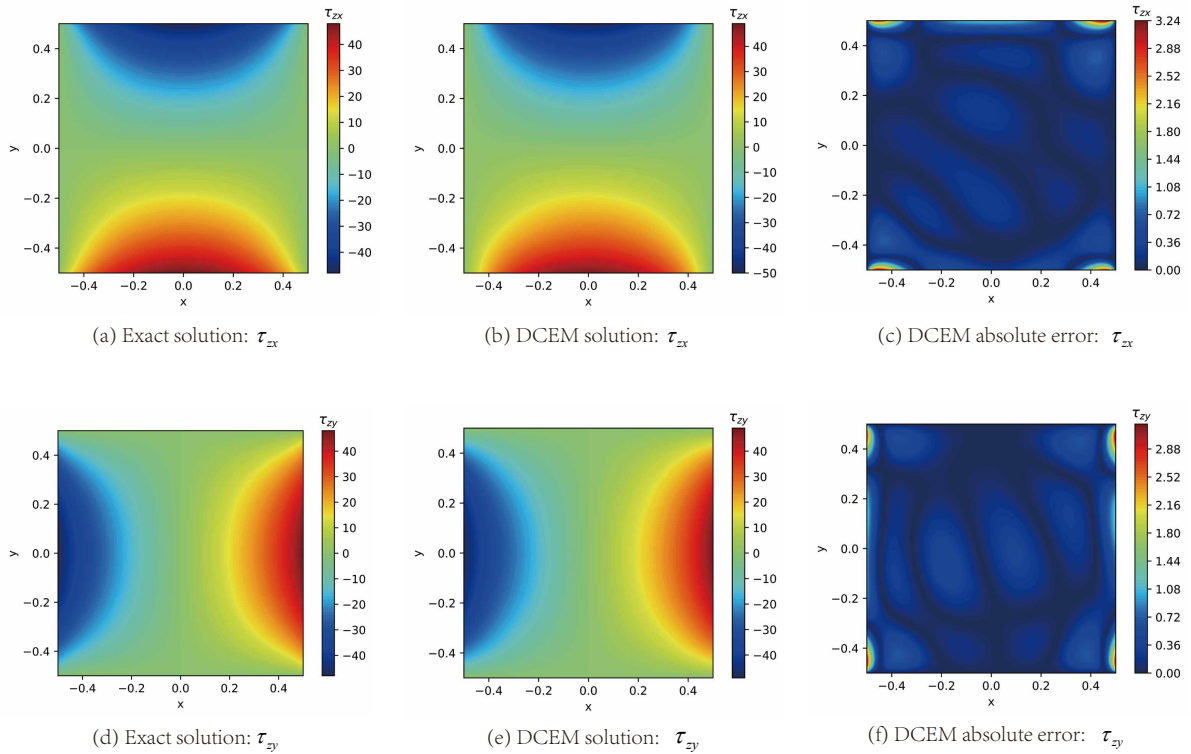


**FIGURE 28** Comparison of numerical and analytical solution of the shear stress in cylinder  $\tau$  in DCEM

However, it should be noted that the DCEM did not converge with respect to the number of hidden layers, as having more hidden layers did not necessarily result in improved accuracy.

Considering that the initial  $\alpha$  of the DCEM may affect the convergence rate and precision, the influence of different initial values of  $\alpha$  on the convergence rate and precision is analyzed, as shown in Fig. 25b. The convergence rate is slower with increasing  $\alpha$ . We explain it from the perspective of the strong form, this is because of the larger constant of the Poisson equation. The neural network is relatively more difficult to fit since the Poisson equation is more apparent in ups and downs. The initial value of  $\alpha$  will not only affect the convergence speed but also significantly influence the accuracy of  $\alpha$ .



The DCEM needs to assume an admissible stress function since it is a full-force boundary condition problem, while the DEM does not need to assume an admissible displacement field. As a result, DEM is more convenient to deal with the full-force boundary condition problem, and this advantage can use the enormous approximate function space of the neural network to optimize and achieve remarkable results.

We compare the DCEM-O (operator learning based on DCEM) with DCEM in this full-force boundary example. The input of the branch net is geometry information,  $a$  and  $b$ . We deal with the  $a$  and  $b$  as the constant field function. The basis function is  $(x^2 - \frac{a^2}{4})(y^2 - \frac{b^2}{4})$ , and the particular function is zero. The output of the DCEM-O can be written as:

$$\phi = (x^2 - \frac{a^2}{4})(y^2 - \frac{b^2}{4})NN_B(a, b; \theta) * NN_T(x, y; \theta). \quad (90)$$

The architecture of the trunk net consists of 6 hidden layers and 30 neurons in every hidden layer. The architecture of the branch net is 3 hidden layers and 30 neurons in every hidden layer. We use the 11 different  $a/b$  ratios as the input of the branch net. The input of the trunk net is  $100 \times 100$  equal spacing points. The output of DCEM-O is the Prandtl stress function  $\phi$ , and the output training dataset is from the analytical solution of the problem<sup>85</sup> or the high fidelity numerical experiment (FEM based on the stress function element<sup>84</sup>). In this example, the data comes from the analytical solution of the rectangle, which can be written as:

$$\begin{aligned} \phi(x, y) &= G\alpha \left( \frac{b^2}{4} - y^2 \right) - \frac{8G\alpha b^2}{\pi^3} \sum_{i=0}^{\infty} \frac{(-1)^i}{(2i+1)^3} \frac{\cosh(\lambda_i x)}{\cosh(\lambda_i a/2)} \cos(\lambda_i y) \\ \lambda_i &= (2i+1) \frac{\pi}{b} \end{aligned} \quad (91)$$

Note that the test dataset (we only test  $a = b = 1$ ) differs from the training set. Fig. 29 shows the comparison of DCEM with DCEM-O, and the absolute error of DCEM-O is lower than DCEM in the same iteration. The absolute error of DCEM is almost the same in the initial 250, 500, and 750 iterations, but DCEM-O converges to the exact solution dramatically in those iterations. Fig. 29m,n shows that the DCEM-O converges faster than DCEM in term of the  $\mathcal{L}_2^{rel}$  and  $\mathcal{H}_1^{rel}$ .

## 5 | DISCUSSION

### 5.1 | The construction of the basis function

In this section, we discuss the construction of the basis function. The distance function is a special form of the basis function, as explained in Section 3.2. If the deep energy method is based on the principle of the minimum potential energy, the basis function is zero only if the position is on the Dirichlet boundary condition. Thus, we can construct different basis functions, as shown in Fig. 30. The idea of the contour line is adopted in the construction of the basis function.

For the sake of simplicity, we use three different basis function  $NN_b^1$ ,  $NN_b^2$ , and  $NN_b^3$  to illustrate the idea. We assume that the direction of the derivative of the  $NN_b^1$ ,  $NN_b^2$ , and  $NN_b^3$  are zero, i.e.

$$\begin{aligned} \frac{\partial NN_b^{(1)}}{\partial l_1} &= 0 \\ \frac{\partial NN_b^{(2)}}{\partial l_2} &= 0 \\ \frac{\partial NN_b^{(3)}}{\partial l_3} &= 0, \end{aligned} \quad (92)$$

where  $l_1$ ,  $l_2$ , and  $l_3$  are the corresponding direction of the derivative, i.e. tangent to contours. It is hard for the general net to learn because the  $NN_b = 0$  and  $\partial NN_b / \partial l = 0$  when the direction is parallel to the contours near the boundary. The direction of

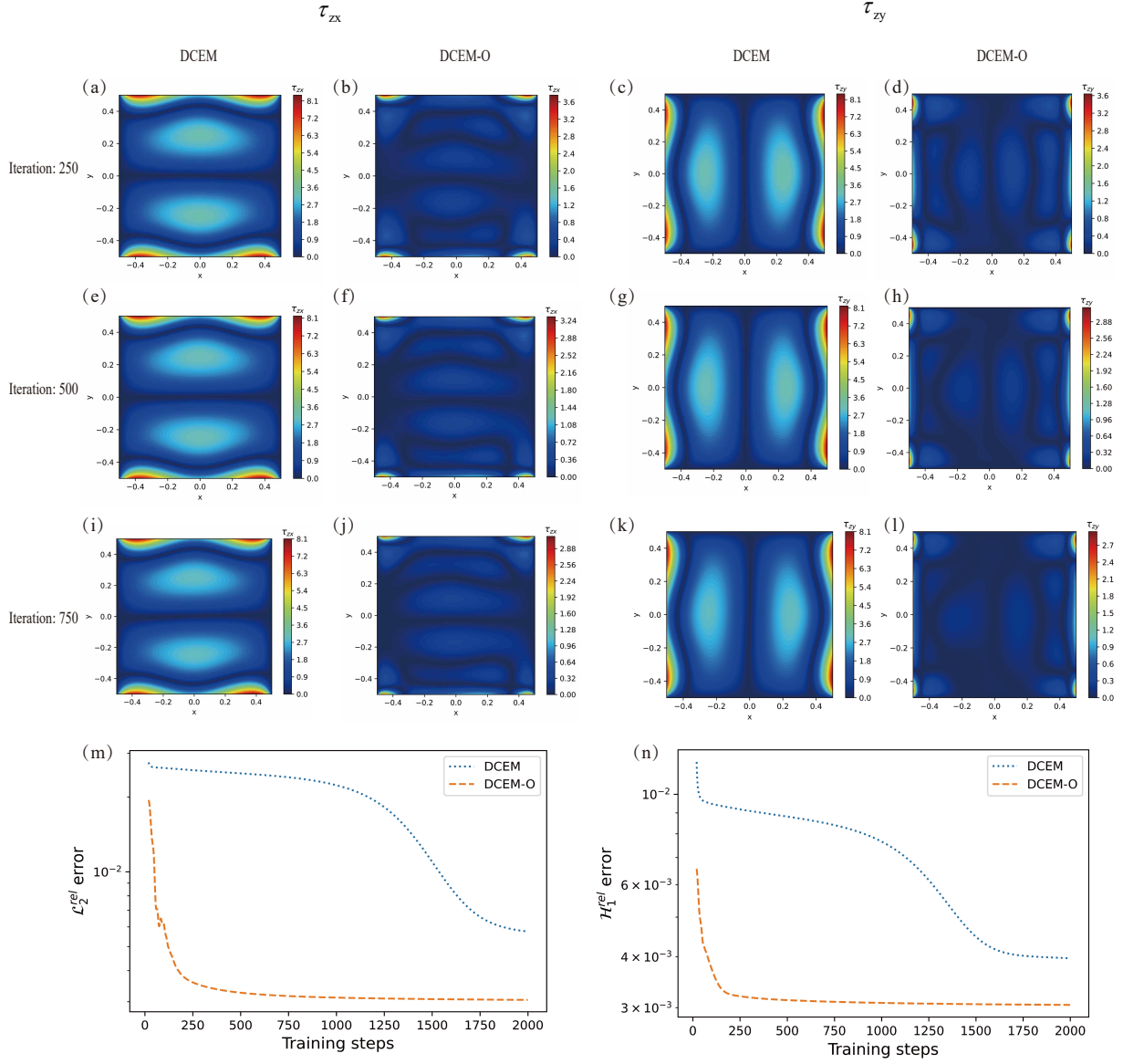


**FIGURE 29** The absolute error of DCEM and DCEM-O in Prandtl stress function of cylinder: (a, b, c, d), (e, f, g, h), and (i, j, k, l) the absolute error in the number of iterations 250, 500, and 750 respectively; (a, e, i, c, g, k) the result of DCEM ; (b, f, j, d, h, l) the result of DCEM-O. (a, b, e, f, i, j) the result of  $\tau_{zx}$ ; (c, d, g, h, k, l) the result of  $\tau_{zy}$ . (m) the evolution of  $L_2^{rel}$  by DCEM and DCEM-O; (n) the evolution of  $H_1^{rel}$  by DCEM and DCEM-O

the derivative can be written as follows:

$$\begin{aligned}
 \frac{\partial \phi}{\partial \mathbf{l}_1} &= \frac{\partial NN_p}{\partial \mathbf{l}_1} + \sum_{i=1}^3 \frac{\partial NN_g^{(i)}}{\partial \mathbf{l}_1} * NN_b^{(i)} + \sum_{i=1}^3 NN_g^{(i)} * \frac{\partial NN_b^{(i)}}{\partial \mathbf{l}_1} \\
 \frac{\partial \phi}{\partial \mathbf{l}_2} &= \frac{\partial NN_p}{\partial \mathbf{l}_2} + \sum_{i=1}^3 \frac{\partial NN_g^{(i)}}{\partial \mathbf{l}_2} * NN_b^{(i)} + \sum_{i=1}^3 NN_g^{(i)} * \frac{\partial NN_b^{(i)}}{\partial \mathbf{l}_2} \\
 \frac{\partial \phi}{\partial \mathbf{l}_3} &= \frac{\partial NN_p}{\partial \mathbf{l}_3} + \sum_{i=1}^3 \frac{\partial NN_g^{(i)}}{\partial \mathbf{l}_3} * NN_b^{(i)} + \sum_{i=1}^3 NN_g^{(i)} * \frac{\partial NN_b^{(i)}}{\partial \mathbf{l}_3}.
 \end{aligned} \tag{93}$$

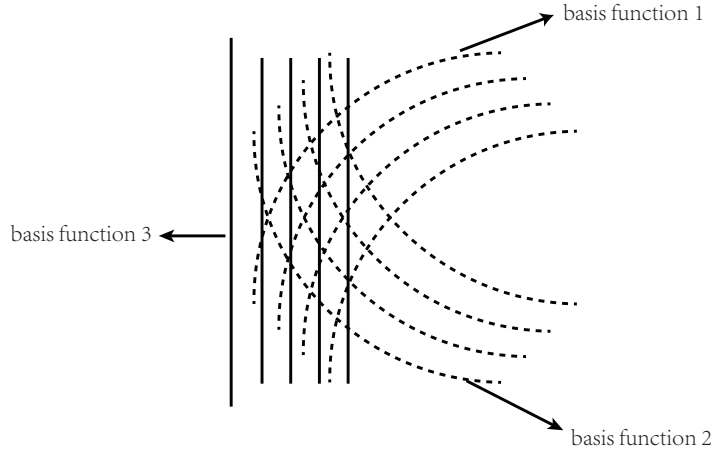


**FIGURE 30** The schematic of the different basis function.

Because  $\partial NN_b^1/l_1 = 0$ ,  $\partial NN_b^2/l_2 = 0$ , and  $\partial NN_b^3/l_3 = 0$ , Eq. (93) can be further written as

$$\begin{aligned}
 \frac{\partial \phi}{\partial l_1} &= \frac{\partial NNp}{\partial l_1} + NNg^{(2)} * \frac{\partial NNb^{(2)}}{\partial l_1} + NNg^{(3)} * \frac{\partial NNb^{(3)}}{\partial l_1} \\
 \frac{\partial \phi}{\partial l_2} &= \frac{\partial NNp}{\partial l_2} + NNg^{(1)} * \frac{\partial NNb^{(1)}}{\partial l_2} + NNg^{(3)} * \frac{\partial NNb^{(3)}}{\partial l_2} \\
 \frac{\partial \phi}{\partial l_3} &= \frac{\partial NNp}{\partial l_3} + NNg^{(1)} * \frac{\partial NNb^{(1)}}{\partial l_3} + NNg^{(2)} * \frac{\partial NNb^{(2)}}{\partial l_3}
 \end{aligned} \tag{94}$$

In the energy principle training, the basis function network and the particular net are frozen and not trained, and only the general network can be trained. The Eq. (94) shows that although one of the basis function networks makes the corresponding general network impossible training, the other two generalized networks are still trainable. As a result, constructing different basis function is beneficial to training general network based on energy principle and improve the accuracy of DEM near the boundary.

## 5.2 | The comparison of DEM, PINNs strong form, and DCEM

PINNs strong form of stress function is suitable for dealing with full-force boundary conditions. However, it is not convenient to solve the problem with the displacement boundary because displacement boundary conditions are formulated in the form of boundary integral equations. On the other hand, DCEM based on the minimum complementary energy principle only needs to convert the displacement boundary conditions into the complementary potential for optimization when dealing with the displacement boundary conditions, which is difficult for the PINN strong form of the stress function. From the construction of the admissible field, DEM is more suitable for dealing with the problems dominated by the force boundary conditions because it reduce the requirement of the construction of the admissible displacement field on the force boundary condition. In contrast, DCEM is suitable for dealing with displacement boundary conditions.

Therefore, from the perspective of admissible field construction, different problems are suitable for different deep energy methods (DEM or DCEM). One needs to understand the problem's nature so we can choose the suitable deep energy method based on potential or complementary energy.

If we use the penalty method to satisfy the boundary condition, results show PINNs energy form depends more on the hyperparameters for the boundary condition than PINNs strong form empirically, because the energy methods would solve the wrong target if the admissible field is not satisfied. As a result, it is more important to construct the admissible field in DCEM and DEM than PINNs strong forms.

Mathematically, the choice of the form of PDEs can indeed affect the accuracy of the solution for a given physical problem. In the context of solid mechanics, stress as an unknown and basic variable in the DCEM is generally considered to be more accurate than the displacement as an unknown and basic variable in the DEM in term of stress, and vice versa.

### 5.3 | The input of the branch net in DCEM-O

If the input of DeepONet's branch net is a constant field, the constant value can be input to the branch net instead of the variable field function considering the computational efficiency.

The input of the branch net is a variable field. We can choose the suitable architecture of the branch net to be consistent with the nature of the input of the trunk net. For example, if the input of the trunk net is the image structure, we can use the CNN in the trunk net; if the input of the trunk net is the data associated with the time, we can use the RNN to be the architect of the branch net. The key to choosing the architecture of the branch net is to consider the nature of the input of the branch net.

### 5.4 | Applicability of DCEM and DEM

The energy form of PINNs not only can be applied to the reversible processes, but also some irreversible processes, such as viscoelasticity<sup>23</sup> and elastoplasticity<sup>40</sup>. The key of energy form of PINNs is to find the energy form and construct the admissible field.

In many cases, linear problems can be efficiently solved using standard approaches such as the Finite Element Method (FEM). Moreover, for linear problems, reduced order models can be employed to significantly reduce simulation time. On the other hand, when applying machine learning (ML) techniques to solve linear models, the originally well-posed linear problem, which involves finding a solution to a linear system of equations, is transformed into a nonlinear nonconvex optimization problem. This transformation introduces challenges as a unique solution cannot be guaranteed. Therefore, ML-based solutions for partial differential equations (PDEs) should primarily focus on nonlinear problems or optimization/inverse analysis problems. However, it is crucial to demonstrate that these methods can also effectively handle linear problems.

### 5.5 | Energy Bounds in Variational Principles of Elasticity in terms of DEM and DCEM

In elasticity, the variational principles have upper and lower bounds on energy. The approximate displacement solution obtained using the principle of minimum potential energy is theoretically associated with lower strain energy compared to the exact displacement solution. Consequently, the structure exhibits slightly smaller displacements and strains, resulting in lower stresses derived from the constitutive model. On the other hand, the principle of complementary energy yields stresses that are theoretically associated with greater strain energy compared to the exact stress distribution, leading to a softer structural response and higher stress levels. However, it's worth noting that these upper and lower bounds do not directly apply to methods like DEM and DCEM, as shown in Fig. 21. This is because these bounds are achieved in the context of optimization at the extremum, which is challenging to reach in the case of neural network-based methods due to the non-convex nature of the optimization landscape. Therefore, the energy bounds from the variational principles of elasticity may not be fully applied in DEM and DCEM.

### 5.6 | Shear and volumetric locking problem in term of DEM and DCEM

In the low-order elements of displacement finite elements, the deformation mode (interpolation function) cannot well represent volumetric strain (in incompressible problems) or shear strain (in structural elements such as beams, plates, shells, etc.). The stress element uses independent interpolation for stress, and the deformation mode can better reflect the above strain characteristics.

However, in DEM, the displacement field is approximated by the neural networks, so it is extremely "high-order" to avoid the shear and locking problem. As a result, DCEM does not have the absolute advantage of handling volumetric and shear problem theoretically.

## 6 | CONCLUSION

We propose the deep complementary energy method (DCEM) based on the minimum complementary energy principle, a novel deep energy framework for solving elasticity problems in solid mechanics. Our comprehensive comparison between DEM, DCEM, and PINNs strong forms has demonstrated the superior accuracy and efficiency of DCEM, particularly in stress predictions. The construction of admissible function fields plays a crucial role in DEM and DCEM. From the perspective of constructing admissible function fields, DEM is better suited for the problem dominated by force boundaries, whereas DCEM excels in handling the problem dominated by displacement boundaries. We have extended the DCEM framework to DCEM-Plus (DCEM-P), introducing terms that naturally satisfy PDEs, and proposed the Deep Complementary Energy Operator Method (DCEM-O), leveraging operator learning in conjunction with physical equations. The result shows that DCEM-P and DCEM-O can further improve the accuracy and efficiency of DCEM, opening up exciting avenues for future research.

While DCEM has been applied successfully to the two most common stress functions, we recognize the need for testing on three-dimensional problems, involving Morera and Maxwell stress functions, which we intend to explore in our future work. We have proved that DCEM can solve the same nonlinear energy problem theoretically, such as hyperelasticity, if DEM can solve the problem in solid mechanics, but we have yet to test it in the numerical experiment, which we will further study in the future. This work proposes an important supplementary energy form of the deep energy method. In linear elasticity, the relationship between stress and strain is linear, and the relationship between displacement and strain is also linear. Thus, there is no problem for computation based on both energy principles in linear elasticity, i.e. potential and complementary energy. However, there are lots of challenges in nonlinear problems. Complementary energy exists in solid mechanics and other physical fields, such as Helmholtz free energy, enthalpy, Gibbs free energy and internal energy in thermodynamics. The relationship between energy conforms to the Legendre transformation in mathematics. Therefore, DCEM can also apply to the energy principles of Legendre transformation in other physics. The energy method based on deep learning can be applied to irreversible problems, such as viscoelasticity<sup>23</sup> and elastoplasticity<sup>40</sup>, which suggests that DEM and DCEM have great potential if the potential of the irreversible problems as a loss function can be obtained. Standard approaches like FEM can easily and efficiently solve linear problems, and ROD (Reduced Order Models) can be used to drastically reduce the simulation time of such problems. However, deep learning-based solutions for linear models convert the well-posed linear problem into a nonlinear non-convex optimization problem, which cannot guarantee a unique solution. Thus, methods based on deep learning for solving PDEs should focus on nonlinear or optimization and inverse analysis problems.

The work in this paper reflects the broad prospect of combining deep learning with computational mechanics. It is not easy for a purely physics-based energy method to surpass traditional finite elements, and a purely data-driven model will bring about the problem of excessive data requirement. With the in-depth research on neural networks and the advancement of computing power, combined with more and more calculation data results, there are strong reasons to believe that operator learning based on the energy method can bring a balance between data and physical equations. If more high-precision calculation results are stored in the future, the operator learning based on the energy method has the potential to exceed the traditional algorithms, which will give computational mechanics the new and broad research prospects.

### AUTHOR CONTRIBUTIONS

**Yizheng Wang:** Conceptualisation, Methodology, Coding, Formal analysis, Writing-Original draft. **Jia Sun:** Advising, Scientific Discussions, Writing-Reviewing and Editing. **Timon Rabczuk:** Discussions, Writing-Reviewing and Editing. **Yinghua Liu:** Conceptualisation, Discussions, Writing-Reviewing and Editing, Supervision.

### ACKNOWLEDGEMENT

The study was supported by the Key Project of the National Natural Science Foundation of China (12332005). The authors would like to thank Jingyun Bai, Zaiyuan Lu, Yuqing Du, Hugo Santos and Lu Lu for helpful discussions.

## FINANCIAL DISCLOSURE

None reported.

## CONFLICT OF INTEREST

The authors declare no potential conflict of interests.

## References

1. Samaniego E, Anitescu C, Goswami S, et al. An energy approach to the solution of partial differential equations in computational mechanics via machine learning: Concepts, implementation and applications. *Computer Methods in Applied Mechanics and Engineering*. 2020;362:112790.
2. Brunton SL, Proctor JL, Kutz JN. Discovering governing equations from data by sparse identification of nonlinear dynamical systems. *Proceedings of the national academy of sciences*. 2016;113(15):3932–3937.
3. Zienkiewicz OC, Taylor RL, Zhu JZ. *The finite element method: its basis and fundamentals*. Elsevier, 2005.
4. Hughes TJ. *The finite element method: linear static and dynamic finite element analysis*. Courier Corporation, 2012.
5. Bathe KJ. *Finite element procedures*. Klaus-Jurgen Bathe, 2006.
6. Reddy JN. *Introduction to the finite element method*. McGraw-Hill Education, 2019.
7. Darwish M, Moukalled F. *The finite volume method in computational fluid dynamics: an advanced introduction with OpenFOAM® and Matlab®*. Springer, 2016.
8. LeVeque RJ. *Finite difference methods for ordinary and partial differential equations: steady-state and time-dependent problems*. SIAM, 2007.
9. Zhang X, Chen Z, Liu Y. *The material point method: a continuum-based particle method for extreme loading cases*. Academic Press, 2016.
10. Liu GR, Karamanlidis D. Mesh free methods: moving beyond the finite element method. *Appl. Mech. Rev.*. 2003;56(2):B17–B18.
11. Rabczuk T, Belytschko T. Cracking particles: a simplified meshfree method for arbitrary evolving cracks. *International journal for numerical methods in engineering*. 2004;61(13):2316–2343.
12. Nguyen VP, Rabczuk T, Bordas S, Duflo M. Meshless methods: a review and computer implementation aspects. *Mathematics and computers in simulation*. 2008;79(3):763–813.
13. Rabczuk T, Belytschko T. A three-dimensional large deformation meshfree method for arbitrary evolving cracks. *Computer methods in applied mechanics and engineering*. 2007;196(29-30):2777–2799.
14. Rabczuk T, Song JH, Zhuang X, Anitescu C. *Extended finite element and meshfree methods*. Academic Press, 2019.
15. Wang Y, Sun J, Li W, Lu Z, Liu Y. CENN: Conservative energy method based on neural networks with subdomains for solving variational problems involving heterogeneous and complex geometries. *Computer Methods in Applied Mechanics and Engineering*. 2022;400:115491.
16. Koric S, Hibbeler LC, Thomas BG. Explicit coupled thermo-mechanical finite element model of steel solidification. *International Journal for Numerical Methods in Engineering*. 2009;78(1):1–31.
17. Silver D, Huang A, Maddison CJ, et al. Mastering the game of Go with deep neural networks and tree search. *Nature*. 2016;529(7587):484–489. OA status: bronzedoi: [10.1038/nature16961](https://doi.org/10.1038/nature16961)
18. Vinyals O, Babuschkin I, Czarnecki WM, et al. Grandmaster level in StarCraft II using multi-agent reinforcement learning. *Nature*. 2019;575(7782):350–354. doi: [10.1038/s41586-019-1724-z](https://doi.org/10.1038/s41586-019-1724-z)
19. Krizhevsky A, Sutskever I, Hinton GE. Imagenet classification with deep convolutional neural networks. *Advances in neural information processing systems*. 2012;25:1097–1105.
20. Graves A, Fernández S, Gomez F, Schmidhuber J. Connectionist temporal classification: labelling unsegmented sequence data with recurrent neural networks. 2006:369–376.
21. Popel M, Tomkova M, Tomek J, et al. Transforming machine translation: a deep learning system reaches news translation quality comparable to human professionals. *Nature communications*. 2020;11(1):1–15.
22. Senior AW, Evans R, Jumper J, et al. Improved protein structure prediction using potentials from deep learning. *Nature*. 2020;577(7792):706–710. doi: [10.1038/s41586-019-1923-7](https://doi.org/10.1038/s41586-019-1923-7)

23. Abueidda DW, Koric S, Al-Rub RA, Parrott CM, James KA, Sobh NA. A deep learning energy method for hyperelasticity and viscoelasticity. *European Journal of Mechanics-A/Solids*. 2022;95:104639.
24. Kirchdoerfer T, Ortiz M. Data-driven computational mechanics. *Computer Methods in Applied Mechanics and Engineering*. 2016;304:81–101.
25. Kirchdoerfer T, Ortiz M. Data-driven computing in dynamics. *International Journal for Numerical Methods in Engineering*. 2018;113(11):1697–1710.
26. Li L, Chen C. Equilibrium-based convolution neural networks for constitutive modeling of hyperelastic materials. *Journal of the Mechanics and Physics of Solids*. 2022;164:104931.
27. Flaschel M, Kumar S, De Lorenzis L. Unsupervised discovery of interpretable hyperelastic constitutive laws. *Computer Methods in Applied Mechanics and Engineering*. 2021;381:113852.
28. Li X, Liu Z, Cui S, Luo C, Li C, Zhuang Z. Predicting the effective mechanical property of heterogeneous materials by image based modeling and deep learning. *Computer Methods in Applied Mechanics and Engineering*. 2019;347:735–753.
29. Li X, Ning S, Liu Z, Yan Z, Luo C, Zhuang Z. Designing phononic crystal with anticipated band gap through a deep learning based data-driven method. *Computer Methods in Applied Mechanics and Engineering*. 2020;361:112737.
30. Kollmann HT, Abueidda DW, Koric S, Guleryuz E, Sobh NA. Deep learning for topology optimization of 2D metamaterials. *Materials & Design*. 2020;196:109098.
31. Liu B, Wang Y, Rabczuk T, Olofsson T, Lu W. Multi-scale modeling in thermal conductivity of Polyurethane incorporated with Phase Change Materials using Physics-Informed Neural Networks. *arXiv preprint arXiv:2307.16785*. 2023.
32. Wang S, Teng Y, Perdikaris PJSJoSC. Understanding and mitigating gradient flow pathologies in physics-informed neural networks. *SIAM Journal on Scientific Computing*. 2021;43(5):A3055-A3081.
33. Li L, Li Y, Du Q, Liu T, Xie Y. ReF-nets: Physics-informed neural network for Reynolds equation of gas bearing. *Computer Methods in Applied Mechanics and Engineering*. 2022;391:114524.
34. Matthey R, Ghosh S. A novel sequential method to train physics informed neural networks for Allen Cahn and Cahn Hilliard equations. *Computer Methods in Applied Mechanics and Engineering*. 2022;390:114474.
35. Cybenko G. Approximation by superpositions of a sigmoidal function. *Mathematics of control, signals and systems*. 1989;2(4):303–314.
36. Hornik K. Approximation capabilities of multilayer feedforward networks. *Neural networks*. 1991;4(2):251–257.
37. Raissi M, Perdikaris P, Karniadakis GE. Physics-informed neural networks: A deep learning framework for solving forward and inverse problems involving nonlinear partial differential equations. *Journal of Computational Physics*. 2019;378:686–707.
38. Lagaris IE, Likas A, Fotiadis DI. Artificial neural networks for solving ordinary and partial differential equations. *IEEE transactions on neural networks*. 1998;9(5):987–1000.
39. Lee H, Kang IS. Neural algorithm for solving differential equations. *Journal of Computational Physics*. 1990;91(1):110–131.
40. He J, Abueidda D, Al-Rub RA, Koric S, Jasiuk I. A deep learning energy-based method for classical elastoplasticity. *International Journal of Plasticity*. 2023:103531.
41. Haghghat E, Raissi M, Moure A, Gomez H, Juanes R. A physics-informed deep learning framework for inversion and surrogate modeling in solid mechanics. *Computer Methods in Applied Mechanics and Engineering*. 2021;379:113741. doi: [10.1016/j.cma.2021.113741](https://doi.org/10.1016/j.cma.2021.113741)
42. Goswami S, Yin M, Yu Y, Karniadakis GE. A physics-informed variational DeepONet for predicting crack path in quasi-brittle materials. *Computer Methods in Applied Mechanics and Engineering*. 2022;391:114587.
43. Cai S, Mao Z, Wang Z, Yin M, Karniadakis GE. Physics-informed neural networks (PINNs) for fluid mechanics: A review. *Acta Mechanica Sinica*. 2021;37(12):1727–1738.
44. Raissi M, Yazdani A, Karniadakis GE. Hidden fluid mechanics: Learning velocity and pressure fields from flow visualizations. *Science*. 2020;367(6481):1026–1030.
45. Yin M, Zheng X, Humphrey JD, Karniadakis GE. Non-invasive inference of thrombus material properties with physics-informed neural networks. *Computer Methods in Applied Mechanics and Engineering*. 2021;375:113603.
46. Yin M, Ban E, Rego BV, et al. Simulating progressive intramural damage leading to aortic dissection using DeepONet: an operator–regression neural network. *Journal of the Royal Society Interface*. 2022;19(187):20210670.
47. Goswami S, Anitescu C, Rabczuk T. Adaptive fourth-order phase field analysis using deep energy minimization. *Theoretical and Applied Fracture Mechanics*. 2020;107:102527.

48. Goswami S, Anitescu C, Chakraborty S, Rabczuk T. Transfer learning enhanced physics informed neural network for phase-field modeling of fracture. *Theoretical and Applied Fracture Mechanics*. 2020;106:102447.
49. Nguyen-Thanh VM, Zhuang X, Rabczuk T. A deep energy method for finite deformation hyperelasticity. *European Journal of Mechanics-A/Solids*. 2020;80:103874.
50. Nguyen-Thanh VM, Anitescu C, Alajlan N, Rabczuk T, Zhuang X. Parametric deep energy approach for elasticity accounting for strain gradient effects. *Computer Methods in Applied Mechanics and Engineering*. 2021;386:114096. doi: [10.1016/j.cma.2021.114096](https://doi.org/10.1016/j.cma.2021.114096)
51. Wang S, Wang H, Perdikaris P. On the eigenvector bias of Fourier feature networks: From regression to solving multi-scale PDEs with physics-informed neural networks. *Computer Methods in Applied Mechanics and Engineering*. 2021;384:113938. doi: [10.1016/j.cma.2021.113938](https://doi.org/10.1016/j.cma.2021.113938)
52. Wang S, Yu X, Perdikaris P. When and why PINNs fail to train: A neural tangent kernel perspective. *Journal of Computational Physics*. 2022;449:110768.
53. Li W, Bazant MZ, Zhu J. A physics-guided neural network framework for elastic plates: Comparison of governing equations-based and energy-based approaches. *Computer Methods in Applied Mechanics and Engineering*. 2021;383:113933. doi: [10.1016/j.cma.2021.113933](https://doi.org/10.1016/j.cma.2021.113933)
54. Fuhg JN, Bouklas N. The mixed deep energy method for resolving concentration features in finite strain hyperelasticity. *Journal of Computational Physics*. 2022;451:110839.
55. Abueidda DW, Koric S, Guleryuz E, Sobh NA. Enhanced physics-informed neural networks for hyperelasticity. *International Journal for Numerical Methods in Engineering*. 2023;124(7):1585–1601.
56. Rao C, Ren P, Wang Q, Buyukozturk O, Sun H, Liu Y. Encoding physics to learn reaction–diffusion processes. *Nature Machine Intelligence*. 2023:1-15.
57. Paszke A, Gross S, Massa F, et al. Pytorch: An imperative style, high-performance deep learning library. *Advances in neural information processing systems*. 2019;32.
58. Abadi M, Barham P, Chen J, et al. Tensorflow: a system for large-scale machine learning.. In: . 16. Savannah, GA, USA. 2016:265–283.
59. Cai S, Wang Z, Fuest F, Jeon YJ, Gray C, Karniadakis GE. Flow over an espresso cup: inferring 3-D velocity and pressure fields from tomographic background oriented Schlieren via physics-informed neural networks. *Journal of Fluid Mechanics*. 2021;915:A102.
60. Stumpf H. The principle of complementary energy in nonlinear plate theory. *Journal of Elasticity*. 1976;6(1):95–104.
61. Lu L, Meng X, Cai S, et al. A comprehensive and fair comparison of two neural operators (with practical extensions) based on fair data. *Computer Methods in Applied Mechanics and Engineering*. 2022;393:114778.
62. Wang S, Wang H, Perdikaris P. Learning the solution operator of parametric partial differential equations with physics-informed DeepONets. *Science advances*. 2021;7(40):eabi8605.
63. Wen G, Li Z, Azizzadenesheli K, Anandkumar A, Benson SM. U-FNO—An enhanced Fourier neural operator-based deep-learning model for multiphase flow. *Advances in Water Resources*. 2022;163:104180.
64. Lu L, Jin P, Pang G, Zhang Z, Karniadakis GE. Learning nonlinear operators via DeepONet based on the universal approximation theorem of operators. *Nature Machine Intelligence*. 2021;3(3):218-229. doi: [10.1038/s42256-021-00302-5](https://doi.org/10.1038/s42256-021-00302-5)
65. Li Z, Kovachki N, Azizzadenesheli K, et al. Fourier neural operator for parametric partial differential equations. *arXiv preprint arXiv:2010.08895*. 2020.
66. Chen T, Chen H. Universal approximation to nonlinear operators by neural networks with arbitrary activation functions and its application to dynamical systems. *IEEE Transactions on Neural Networks*. 1995;6(4):911–917.
67. LeCun Y, Boser B, Denker JS, et al. Backpropagation applied to handwritten zip code recognition. *Neural computation*. 1989;1(4):541–551.
68. Vaswani A, Shazeer N, Parmar N, et al. Attention is all you need. *Advances in neural information processing systems*. 2017;30.
69. Hornik K, Stinchcombe M, White H. Multilayer feedforward networks are universal approximators. *Neural networks*. 1989;2(5):359–366.
70. Paszke A, Gross S, Chintala S, et al. Automatic differentiation in pytorch. 2017.
71. Gasser TC, Ogden RW, Holzapfel GA. Hyperelastic modelling of arterial layers with distributed collagen fibre orientations. *Journal of the royal society interface*. 2006;3(6):15–35.
72. Chagnon G, Rebouah M, Favier D. Hyperelastic energy densities for soft biological tissues: a review. *Journal of Elasticity*. 2015;120(2):129–160.
73. Belytschko T, Liu WK, Moran B, Elkhodary K. *Nonlinear finite elements for continua and structures*. John wiley & sons, 2013.
74. Sukumar N, Srivastava A. Exact imposition of boundary conditions with distance functions in physics-informed deep neural networks. *Computer Methods in Applied Mechanics and Engineering*. 2022;389:114333.



75. Lu L, Pestourie R, Yao W, Wang Z, Verdugo F, Johnson SG. Physics-informed neural networks with hard constraints for inverse design. *SIAM Journal on Scientific Computing*. 2021;43(6):B1105–B1132.
76. Sheng H, Yang C. PFNN: A penalty-free neural network method for solving a class of second-order boundary-value problems on complex geometries. *Journal of Computational Physics*. 2021;428:110085.
77. Berg J, Nyström K. A unified deep artificial neural network approach to partial differential equations in complex geometries. *Neurocomputing*. 2018;317:28–41.
78. Yu B, others . The deep Ritz method: a deep learning-based numerical algorithm for solving variational problems. *Communications in Mathematics and Statistics*. 2018;6(1):1–12.
79. Fung Y. Foundations of solid mechanics. 1965. *Englewood Cliffs, NJ*. 2010;436.
80. Kellogg OD. *Foundations of potential theory*. 31. Courier Corporation, 1953.
81. Rao C, Sun H, Liu Y. Physics-informed deep learning for computational elastodynamics without labeled data. *Journal of Engineering Mechanics*. 2021;147(8):04021043.
82. Li Z, Zheng H, Kovachki N, et al. Physics-informed neural operator for learning partial differential equations. *arXiv preprint arXiv:2111.03794*. 2021.
83. Vullo V, others . Circular cylinders and pressure vessels. *Stress Analysis and Design; Springer: Berlin/Heidelberg, Germany*. 2014.
84. Cen S, Fu XR, Zhou MJ. 8-and 12-node plane hybrid stress-function elements immune to severely distorted mesh containing elements with concave shapes. *Computer Methods in Applied Mechanics and Engineering*. 2011;200(29-32):2321–2336.
85. Fung Y. On the Behavior of a Sharp Leading Edge. *Journal of the Aeronautical Sciences*. 1953;20(9):644–645.
86. Boyd S, Boyd SP, Vandenberghe L. *Convex optimization*. Cambridge university press, 2004.

□

## APPENDIX

### A PROOF OF APPLICABILITY OF COMPLEMENTARY ENERGY PRINCIPLE IN NONLINEAR ELASTICITY

All the following proofs are based on the stress-free in the initial configuration and nonlinear elasticity is monotonically increasing, i.e., the stress increases with the increase of strain.

In linear elasticity, both the potential energy principle and the complementary energy principle can be used to solve the same problem as we know. In nonlinear elasticity, the potential energy principle can be used to optimize the hyperelastic problem<sup>49</sup>, but there are few studies on the optimization of nonlinear elasticity problems based on the minimum complementary energy principle. Thus we prove the rationality of using the complementary energy principle for nonlinear elasticity problems, that is, to prove whether the problems that can be solved by using the minimum potential energy principle can be solved by using the minimum complementary energy principle.

First, we prove that the strain complementary energy  $W_c(\boldsymbol{\sigma})$  are the Legendre transformation of the strain energy  $W_p(\boldsymbol{\varepsilon})$  in mathematics. According to the definition of both, we can obtain the relation between them,

$$\begin{aligned}
 W_p(\boldsymbol{\varepsilon}) + W_c(\boldsymbol{\sigma}) &= \boldsymbol{\varepsilon} : \boldsymbol{\sigma} \\
 W_p &= \int_{\boldsymbol{\varepsilon}} \boldsymbol{\sigma}(\boldsymbol{\varepsilon}) : d\boldsymbol{\varepsilon} \\
 W_c &= \int_{\boldsymbol{\sigma}} \boldsymbol{\varepsilon}(\boldsymbol{\sigma}) : d\boldsymbol{\sigma}
 \end{aligned} \tag{A1}$$

Considering the Legendre transformation of the  $W_p$ , we can obtain

$$\begin{aligned}
 W_p^*(\mathbf{d}) &= \boldsymbol{\varepsilon} : \frac{\partial W_p(\boldsymbol{\varepsilon})}{\partial \boldsymbol{\varepsilon}} - W_p(\boldsymbol{\varepsilon}) \\
 \mathbf{d} &= \frac{\partial W_p(\boldsymbol{\varepsilon})}{\partial \boldsymbol{\varepsilon}},
 \end{aligned} \tag{A2}$$

where  $W_p^*(\mathbf{d})$  is the Legendre transformation of the strain energy  $W_p(\boldsymbol{\varepsilon})$ .

According to the expression of  $W_p$  in Eq. (A1), we get

$$\boldsymbol{\sigma} = \frac{\partial W_p(\boldsymbol{\varepsilon})}{\partial \boldsymbol{\varepsilon}}. \quad (\text{A3})$$

We substitute Eq. (A3) into Eq. (A2) and obtain

$$W_p^*(\mathbf{d}) = \boldsymbol{\varepsilon} : \boldsymbol{\sigma} - W_p(\boldsymbol{\varepsilon}) \quad (\text{A4})$$

Comparing Eq. (A4) with Eq. (A1), we can easily found  $W_p^*(\mathbf{d}) = W_c(\boldsymbol{\sigma})$ . As a result, strain complementary energy  $W_c(\boldsymbol{\sigma})$  are Legendre transformation of strain energy  $W_p(\boldsymbol{\varepsilon})$ .

If we use the minimum potential energy principle, the second variation of the total potential energy

$$J = \int_{\Omega} W_p(\boldsymbol{\varepsilon}) d\Omega - \int_{\Gamma'} \bar{\mathbf{t}} \cdot \mathbf{u} d\Gamma - \int_{\Omega} \mathbf{f} \cdot \mathbf{u} d\Omega$$

must be greater than zero, i.e.

$$\begin{aligned} \delta^2 J &> 0 \\ \delta^2 J &= \frac{1}{2} \int_{\Omega} \delta \boldsymbol{\varepsilon} : \frac{\partial^2 W_p(\boldsymbol{\varepsilon})}{\partial \boldsymbol{\varepsilon} \partial \boldsymbol{\varepsilon}} : \delta \boldsymbol{\varepsilon} d\Omega. \end{aligned} \quad (\text{A5})$$

Since any  $\delta \boldsymbol{\varepsilon}$  holds, if we can use the principle of minimum potential energy to solve the problem,  $\partial^2 W_p(\boldsymbol{\varepsilon})/(\partial \boldsymbol{\varepsilon} \partial \boldsymbol{\varepsilon})$  must be positive, i.e.,  $W_p(\boldsymbol{\varepsilon})$  is the strictly convex function. According to the following lemma,  $W_c(\boldsymbol{\sigma})$  must be the strictly convex function in terms of  $\boldsymbol{\sigma}$ , i.e.,  $\partial^2 W_c(\boldsymbol{\sigma})/(\partial \boldsymbol{\sigma} \partial \boldsymbol{\sigma})$  must be positive.

The Legendre transform of a convex function is convex<sup>86</sup>.

According to the Eq. (A1), we obtain

$$\frac{\partial \boldsymbol{\varepsilon}}{\partial \boldsymbol{\sigma}} = \frac{\partial^2 W_c(\boldsymbol{\sigma})}{\partial \boldsymbol{\sigma} \partial \boldsymbol{\sigma}} > 0. \quad (\text{A6})$$

We assume there is a tensor function  $\varphi$  between  $\boldsymbol{\sigma}$  and  $\boldsymbol{\varepsilon}$ ,

$$\boldsymbol{\varepsilon} = \varphi(\boldsymbol{\sigma}).$$

We get the differential of  $\boldsymbol{\varepsilon}$

$$d\boldsymbol{\varepsilon} = \frac{\partial \varphi(\boldsymbol{\sigma})}{\partial \boldsymbol{\sigma}} : d\boldsymbol{\sigma} = \frac{\partial \boldsymbol{\varepsilon}}{\partial \boldsymbol{\sigma}} : d\boldsymbol{\sigma} = \frac{\partial^2 W_c(\boldsymbol{\sigma})}{\partial \boldsymbol{\sigma} \partial \boldsymbol{\sigma}} : d\boldsymbol{\sigma}.$$

Because  $\partial^2 W_c(\boldsymbol{\sigma})/(\partial \boldsymbol{\sigma} \partial \boldsymbol{\sigma})$  is positive, there is a unique mapping between  $\boldsymbol{\varepsilon}$  and  $\boldsymbol{\sigma}$ , which we prove next.

We assume the different  $\boldsymbol{\sigma}_1$  and  $\boldsymbol{\sigma}_2$ , we obtain the difference in the strain

$$\|\varphi(\boldsymbol{\sigma}_1) - \varphi(\boldsymbol{\sigma}_2)\|_2^2 = \left\| \frac{\partial \varphi(\boldsymbol{\sigma})}{\partial \boldsymbol{\sigma}} \Big|_{\boldsymbol{\sigma}=\boldsymbol{\sigma}^*} : (\boldsymbol{\sigma}_1 - \boldsymbol{\sigma}_2) \right\|_2^2, \quad (\text{A7})$$

where  $\boldsymbol{\sigma}^* \in [\boldsymbol{\sigma}_1, \boldsymbol{\sigma}_2]$  according to Lagrange's Mean Value Theorem, if  $\varphi$  is smooth enough. We analysis Eq. (A7)

$$\left\| \frac{\partial \varphi(\boldsymbol{\sigma})}{\partial \boldsymbol{\sigma}} \Big|_{\boldsymbol{\sigma}=\boldsymbol{\sigma}^*} : (\boldsymbol{\sigma}_1 - \boldsymbol{\sigma}_2) \right\|_2^2 = (\boldsymbol{\sigma}_1 - \boldsymbol{\sigma}_2)^T \left[ \frac{\partial \varphi(\boldsymbol{\sigma})}{\partial \boldsymbol{\sigma}} \right]^T \left[ \frac{\partial \varphi(\boldsymbol{\sigma})}{\partial \boldsymbol{\sigma}} \right] (\boldsymbol{\sigma}_1 - \boldsymbol{\sigma}_2) > 0.$$

Because  $\partial \varphi(\boldsymbol{\sigma})/\partial \boldsymbol{\sigma} = \partial^2 W_c(\boldsymbol{\sigma})/(\partial \boldsymbol{\sigma} \partial \boldsymbol{\sigma})$  is positive,  $[\partial \varphi(\boldsymbol{\sigma})/\partial \boldsymbol{\sigma}]^T [\partial \varphi(\boldsymbol{\sigma})/\partial \boldsymbol{\sigma}]$  must be positive too, which results in

$$\|\varphi(\boldsymbol{\sigma}_1) - \varphi(\boldsymbol{\sigma}_2)\|_2^2 > 0.$$

It means the different  $\boldsymbol{\sigma}_1$  and  $\boldsymbol{\sigma}_2$  can not map to the same  $\boldsymbol{\varepsilon}$ . It is easy to prove that different strains must be expressed as different stresses, and the proof results are the same as above. Thus, there is a unique mapping between  $\boldsymbol{\varepsilon}$  and  $\boldsymbol{\sigma}$  each other.

As a result, there must be a formula for expressing strain in terms of stress so that we can solve the problem by the minimum complementary energy theorem if the nonlinear elasticity problem can be solved by the minimum potential energy theorem. The key to the problem is to find the expression of the strain in terms of stress. It is worth noting that this relationship may be implicit, so it may be represented by a neural network.

## B THE APPLICATION OF THE PROPERTY OF THE AIRY STRESS FUNCTION

The proof is based on free body force.

In this appendix, we show

$$\begin{aligned} n_x \frac{\partial^2 \phi}{\partial y^2} - n_y \frac{\partial^2 \phi}{\partial x \partial y} &= \bar{t}_x \\ -n_x \frac{\partial^2 \phi}{\partial x \partial y} + n_y \frac{\partial^2 \phi}{\partial x^2} &= \bar{t}_y \end{aligned} \quad (\text{B8})$$

is equal to

$$\begin{aligned} \phi &= M \\ \frac{\partial \phi}{\partial \mathbf{n}} &= -R_s = -s_x R_x - s_y R_y, \end{aligned} \quad (\text{B9})$$

where  $M$  and  $R_s$  are explained in Fig. 3a. We consider the moment  $M$  of an external force about a point  $B$  from the initial point  $A$

$$M|_B = \int_A^B [\bar{t}_x (y_B - y) + \bar{t}_y (x - x_B)] ds. \quad (\text{B10})$$

We substitute Eq. (B8) into Eq. (B10), and we can obtain

$$\begin{aligned} M|_B &= \int_A^B [(n_x \frac{\partial^2 \phi}{\partial y^2} - n_y \frac{\partial^2 \phi}{\partial x \partial y})(y_B - y) + (-n_x \frac{\partial^2 \phi}{\partial x \partial y} + n_y \frac{\partial^2 \phi}{\partial x^2})(x - x_B)] ds \\ &= \int_A^B [(\frac{dy}{ds} \frac{\partial^2 \phi}{\partial y^2} + \frac{dx}{ds} \frac{\partial^2 \phi}{\partial x \partial y})(y_B - y) + (-\frac{dy}{ds} \frac{\partial^2 \phi}{\partial x \partial y} - \frac{dx}{ds} \frac{\partial^2 \phi}{\partial x^2})(x - x_B)] ds \\ &= \int_A^B [\frac{d(\frac{\partial \phi}{\partial y})}{ds} (y_B - y) + \frac{d(\frac{\partial \phi}{\partial x})}{ds} (x_B - x)] ds \\ &= \int_A^B d(\frac{\partial \phi}{\partial y})(y_B - y) + d(\frac{\partial \phi}{\partial x})(x_B - x) \\ &= [\frac{\partial \phi}{\partial y} (y_B - y) + \frac{\partial \phi}{\partial x} (x_B - x)]|_A^B - \int_A^B [\frac{\partial \phi}{\partial y} (-\frac{dy}{ds}) - \frac{\partial \phi}{\partial x} (\frac{dx}{ds})] ds \\ &= -[\frac{\partial \phi}{\partial y}|_A (y_B - y_A) + \frac{\partial \phi}{\partial x}|_A (x_B - x_A)] + \int_A^B d\phi, \end{aligned}$$

where  $n_x$  and  $n_y$  are the normal direction of boundary, and  $s_x$  and  $s_y$  are the tangent direction of the boundary,

$$\begin{aligned} n_x &= \frac{dy}{ds} = s_y \\ n_y &= -\frac{dx}{ds} = -s_x. \end{aligned}$$

We set

$$\phi|_A = \frac{\partial \phi}{\partial x}|_A = \frac{\partial \phi}{\partial y}|_A = 0,$$

because point  $A$  is the initial point.

Thus

$$M = \phi|_B.$$

Now we show the second part of the Eq. (B9), and we also substitute Eq. (B8) into the second part of Eq. (B9), and we can obtain

$$\begin{aligned}
-R_s|_B &= -s_x R_x - s_y R_y \\
&= -s_x \int_A^B \bar{t}_x ds - s_y \int_A^B \bar{t}_y ds \\
&= -\frac{dx}{ds} \int_A^B \left( \frac{dy}{ds} \frac{\partial^2 \phi}{\partial y^2} + \frac{dx}{ds} \frac{\partial^2 \phi}{\partial x \partial y} \right) ds - \frac{dy}{ds} \int_A^B \left( -\frac{dy}{ds} \frac{\partial^2 \phi}{\partial x \partial y} - \frac{dx}{ds} \frac{\partial^2 \phi}{\partial^2 x} \right) ds \\
&= -\frac{dx}{ds} \int_A^B \left( \frac{d(\frac{\partial \phi}{\partial y})}{ds} \right) ds + \frac{dy}{ds} \int_A^B \left( \frac{d(\frac{\partial \phi}{\partial x})}{ds} \right) ds \\
&= -\frac{dx}{ds} \left( \frac{\partial \phi}{\partial y} \Big|_A^B \right) + \frac{dy}{ds} \left( \frac{\partial \phi}{\partial x} \Big|_A^B \right) \\
&= n_y \left( \frac{\partial \phi}{\partial y} \Big|_B \right) + n_x \left( \frac{\partial \phi}{\partial x} \Big|_B \right).
\end{aligned}$$

As a result,

$$\frac{\partial \phi}{\partial \mathbf{n}} = -R_s.$$

The proof from Eq. (B9) to Eq. (B8) is the same, so we won't explain the details here.

### C THE BASIS FUNCTION IN AIRY STRESS FUNCTION

If we use the idea of the distance function (basis function), we show that the basis function must satisfy  $\{\mathbf{x}_i \in \Gamma^t, \phi|_{\mathbf{x}_i} = 0\}_{i=1}^n$ ;  $\{\mathbf{x}_i \in \Gamma^t, \partial \phi / \partial \mathbf{n}|_{\mathbf{x}_i} = 0\}_{i=1}^n$ . The construction of the admissible stress function can be written as:

$$\phi = \phi_p + \phi_g * \phi_b,$$

where the particular solution  $\phi_p$  satisfy the natural boundary condition. We analyze

$$\frac{\partial \phi}{\partial \mathbf{n}} = \frac{\partial \phi_p}{\partial \mathbf{n}} + \frac{\partial \phi_g}{\partial \mathbf{n}} * \phi_b + \phi_g * \frac{\partial \phi_b}{\partial \mathbf{n}}.$$

If we set  $\{\mathbf{x}_i \in \Gamma^t, \phi_b|_{\mathbf{x}_i} = 0\}_{i=1}^n$ ;  $\{\mathbf{x}_i \in \Gamma^t, \partial \phi_b / \partial \mathbf{n}|_{\mathbf{x}_i} = 0\}_{i=1}^n$ , the stress function can satisfy the admissible stress function.

### D SUPPLEMENTARY CODE

The code of this work will be available at <https://github.com/yizheng-wang/Research-on-Solving-Partial-Differential-Equations-of-Solid-Mechanics-Based-on-PINN>. Note to editor and reviewers: the link above will be made public upon the publication of this manuscript. During the review period, the data and source code can be made available upon request to the corresponding author.